Doctoral Dissertation

Lyotropic Liquid Crystalline Property, Organized Structure and Pressure Response in Highly Proton-Conductive Sulfonated Polyimide Thin Films

Yuze Yao

Supervisor : Yuki NAGAO

School of Materials Science

Japan Advanced Institute of Science and Technology

March 2023

Abstract

The catalyst layer (LC) is an important part of the polymer electrolyte membrane fuel cells (PEMFCs), where the hydrogen oxidation and oxygen reduction reactions (ORR) take place. Therefore, the efficiency of the LC has a profound effect on the performance of PEMFCs. The CL is a multi-scale composite structure composed of platinum group metal catalysts, carbon supports, ionomer materials and pores. The ionomers are used as binder and proton conduction network, carbon supports are applied to electron conduction, and pores provide mass transport channels for reactants and products. Studies have shown that the ionomer coverage on the catalyst particles decreases the ORR activity and increases the difficulty of oxygen diffusion to Pt surface, which seriously affects cell performance. Although reducing the thickness of the ionomer coating layer can effectively solve this problem, it will cause inhomogeneous distribution of ionomers and low proton transport efficiency. Hence, it is necessary to develop ionomer thin film materials with high proton conductivity.

After decades of research, designing polymers with efficient proton transport channels based on well-defined phase segregation is a basic principle for development of high-performance proton-conducting materials. The alkyl-sulfonated polyimides (ASPIs) are a kind of high proton-conducting materials that can form ordered structure under humidified conditions driven by lyotropic liquid crystalline (LC) properties. Previous studies have systematically explored the lyotropic LC properties of fully aromatic ASPIs. However, the reports on sulfonated semi-alicyclic polyimides are still rare. Therefore, this study mainly focused on exploring the influence of semi-alicyclic structure on the ordered structure driven by lyotropic LC properties and proton conductivity of ASPI thin films. In addition, the potential of ASPIs as pressure-sensitive materials was explored.

Firstly, a sulfonated semi-alicyclic polyimide (BSPA-BOEDA) with a dienophile structure in backbone was newly synthesized. A facile cross-linking reaction was carried out via $Fe3^{+}$-catalyzed Diels–Alder (D-A) reaction between BSPA-BOEDA and silica nanoparticles modified by (3-cyclopentadienylpropyl) triethoxyslane (CPTS). Compared with BSPA-BOEDA, the cross-linked BSPA-BPEDA-NPs membrane and thin film showed better stability in water. Because of the nonlinear molecular conformation of neither BSPA-BOEDA nor BSPA-BPEDA-NPs can form well-defined ordered structures but only form phase separation. The proton conductivity of BSPA-BPEDA-NPs thin film is lower than that of BSPA-BOEDA thin film due to the cross-linking, reaching maxima value of 0.01 and 0.04 S cm^{-1} at 25 °C and 95% RH,

respectively.

Secondly, a sulfonated semi-alicyclic oligoimide (BSPA-CPDA) with a linear molecular conformation was newly synthesized. Benefiting from this conformation, the BSPA-CPDA thin film forms a lamellar structure similar to that of fully aromatic alkyl sulfonated polyimides driven by lyotropic liquid crystal properties, even the molecular weight is significantly lower. The BSPA-CPDA thin film exhibits a high proton conductivity of 0.2 S cm^{-1} at 25 °C and 95% RH, which is the highest value among reported alkyl sulfonated polyimides with comparable molecular weight.

Finally, the basic pressure sensitivity of three ASPIs (ASPI-1, ASPI-2 and APOS-PMDA) was investigated. The results show that ASPI-1 has no pressure sensitivity, while ASPI-2 and APOS-PMDA show reproducible pressure sensitivity under humidified conditions. Particularly, the resistance of ASPI-2 thin film increases linearly with increasing the pressure between 0.1 and 0.2 MPa and the calculated sensitivity is 24 MPa^{-1}.

Keyword: Sulfonated imide ionomer, Proton-conductive thin film, Lyotropic liquid crystal, Pressure sensor

Table of Contents

List of Figures

Chapter 1

Chapter 2

Chapter 3

List of Scheme

List of Table

Chapter 1
General Introduction

1.1 Liquid Crystal (LC)

Liquid crystals (LCs) are well known as they represent the dominant technology for fabricating electronic display screens in recent decades. The beginning of the recognized liquid crystal science is the discovery of the double melting point phenomenon in the phase transition process of cholesterol benzoate by Austrian scientist Friedrich Reinitzer in 1888.[1] Friedrich Reinitzer found that when cholesterol benzoate was heated to 145.5°C it would become a misty liquid and become completely clear when heated to 178.5°C. During cooling down the liquid, it first turned blue and then became turbid, and it turned purple again when continuously cool down, finally turned into a white solid. In addition, a reticulated strip structure similar to uniaxial needle-like crystals was also observed under the electric field. Then German physicist Otto Lehmann studied this phenomenon and proposed the concept of “liquid crystal” for the first time, as well as the classification methods of nematic phase and smectic phase, creating a precedent for liquid crystal research, hence Otto Lehmann is also known as the father of liquid crystal science. Since then, the development of liquid crystal science has fallen into a trough. Until 1968, the RCA company in the United States used the phenomenon that liquid crystal molecules were affected by the voltage to change the arrangement state of their molecules and can deflect incident light invented the first liquid crystal display. Starting from this, liquid crystal materials have gradually become the most important materials for display manufacturing.

The liquid crystal phase is a special mesophase between solids (crystals) and liquids. In solids, especially crystals, molecules are confined to occupy specific positions in the crystal lattice and their molecular axes are oriented in the same direction. Compared with solids, the interaction between molecules in liquids is much weaker, resulting in the free movement and tumbling of molecules inside the liquid, leading to the loss of positional and orientational order.[2] The molecules in the liquid crystal phase not only maintain some fluidity, but also have orientational order, and sometimes also have a positional order.[3] The physical properties of crystal, liquid crystal and liquid are compared in Table 1. Because the liquid crystal phase has some orientational order, the light and electricity behaviors in the liquid crystal phase show anisotropy. Moreover, the orientational order in liquid crystal phase can be controlled artificially under some certain conditions. Therefore, in addition to being used in the production of liquid crystal displays, liquid crystal materials have also shown great potential in many other fields, such as molecular sensors and detectors, solar cells, and new composite materials, etc. [4,5,6,7]

Table 1-1. Comparison of physical properties for crystal, liquid crystal and liquid

	Positional order	Orientational order	Fluidity
Crystal	yes	yes	no
Liquid Crestal	no	yes	yes
Liquid	no	no	yes

1.2 Classification of liquid crystals

There are various ways to classify liquid crystals. According to the conditions required for liquid crystal formation, it can be divided into thermotropic liquid crystal and lyotropic liquid crystal; according to the molecular weight of the molecules forming liquid crystal, it can be divided into low-molecular-weight liquid crystal and polymer liquid crystal; according to the shape of the molecules forming liquid crystal, it can be divided into calamitic (rod shape), discotic (disk shape) and bend core shape.[2,8]

1.2.1. Thermotropic liquid crystal

If one material can obtain liquid crystal mesophase through temperature change, it is called thermotropic liquid crystal. When the thermotropic liquid crystal is heated to the melting point T_m, it will transform into a liquid crystal phase with both fluidity and birefringence, and the liquid is viscous and turbid. The anisotropy of molecular shapes (such as rod-like molecules or disc-like molecules) and the microphase separation between different chemical structural units within the molecule (incompatibility between rigid cores and flexible chains) are the main driving forces for the formation of liquid crystals. Molecules that are anisotropic in shape tend to line up in parallel to occupy space most efficiently, thus achieving long-range orientational order without long-range positional order. Further, when the microphase separation between the parts with different intramolecular chemical structures causes the structural units with different properties in the molecule to aggregate separately from each other, a complex liquid crystal state structure with one-dimensional, two-dimensional or even three-dimensional positional order is formed. When the temperature continuously rises to the clearing point T_c of the material, the thermotropic liquid crystal will turn into an isotropic liquid again. If this liquid is cooled, the liquid crystal phase can be reversibly obtained again.

The first discovered thermotropic liquid crystal material is cholesteryl benzoate, whose chemical

structure is shown in Figure 1-1(a). After more than 100 years of development, some typical molecular structures of thermotropic liquid crystals are shown in Figure 1-1(b) and (c). Typically, these molecules have a rod- or disk-like rigid core composed of aromatic rings and flexible terminal chains composed of aliphatic hydrocarbons.

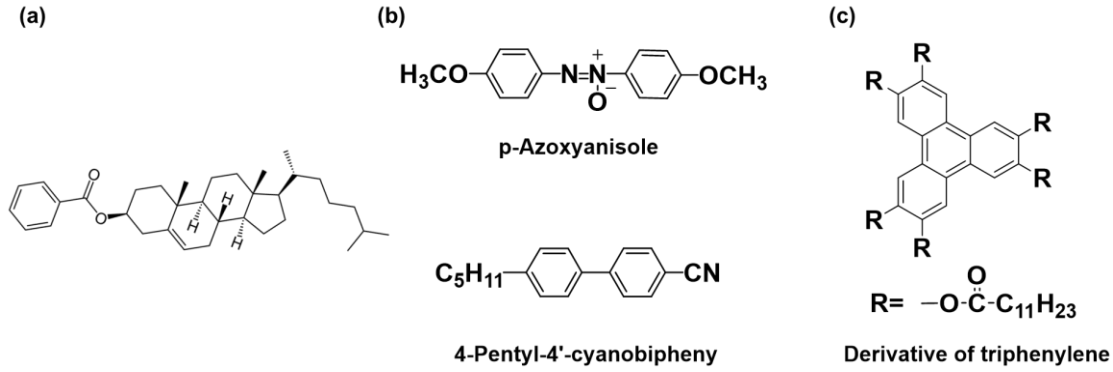

Figure 1-1. (a) Chemical structure of cholesteryl benzoate.[9] typical rod-like (b) and disk-like (c) thermotropic liquid crystals.[10]

Thermotropic liquid crystals can be further subdivided into three types, nematic (N), smectic (Sm), and cholesteric (Chol), according to the different molecular arrangements in their liquid crystal phases.[7,11,12,13]

1.2.2. Lyotropic liquid crystal

Lyotropic liquid crystal is a kind of mesophase formed by the dissolution of amphiphilic molecules (having both hydrophilic and hydrophobic groups) in a polar solvent (usually water). Lyotropic liquid crystals widely exist in nature and living organisms, usually some lipid esters, such as sodium dodecyl sulfonate. When these substances dissolve in water, they self-assemble into many different liquid crystal phases due to the exclusion volume effect. These mesophases have not only nanoscale phase separation but also periodically arranged hydrophilic and hydrophobic features. Lyotropic liquid crystals have attracted great attention in applications such as drug delivery, ion transport, and heterogeneous catalysis due to their self-assembly properties.[14,15] The chemical structures of some typical lyotropic liquid crystal molecules are shown in Figure 1-2.

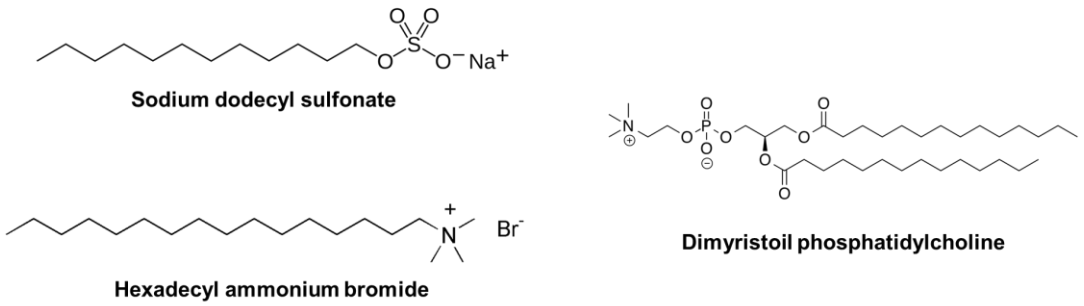

Figure 1-2. Typical lyotropic liquid crystals.[10]

The morphology of lyotropic liquid crystals mainly depends on the concentration of amphiphilic molecules in the solvent and the temperature and pressure at which the liquid crystal phase is formed also affect it.[16,17] Depending on the molecular shape/packing preferences and interfacial curvature energy, lyotropic liquid crystal phases can form in solvent ranging from micelles (I) to cylindrical channels (hexagonal, H)[18,19,20] to planar bilayer lamellas (lamellar, L)[21,22] to three-dimensional interconnected channels (bicontinuous cubic, Q).[23,24,25]

The micelle is the most basic structure for the lyotropic liquid crystal phase. When the amphiphilic molecule reaches a certain concentration in the solvent (called critical micelle concentration, CMC), it will form an oil-in-water structure called normal micelle phase (I_1), as shown in Figure 1-3(a). The subscript 1 indicates that at lower concentrations the hydrophobic portion of the amphiphilic molecule is located at the center of the micelle phase. In contrast, an inverse micelle phase may be formed when the concentration is high, where the water molecule is located at the center. Such an oil-in-water structure is assigned as I_2.[15] When rod-like disk-like micelles have an orientation order, a lyotropic nematic phase similar to the nematic phase will be formed (Figure 1-3(b)).

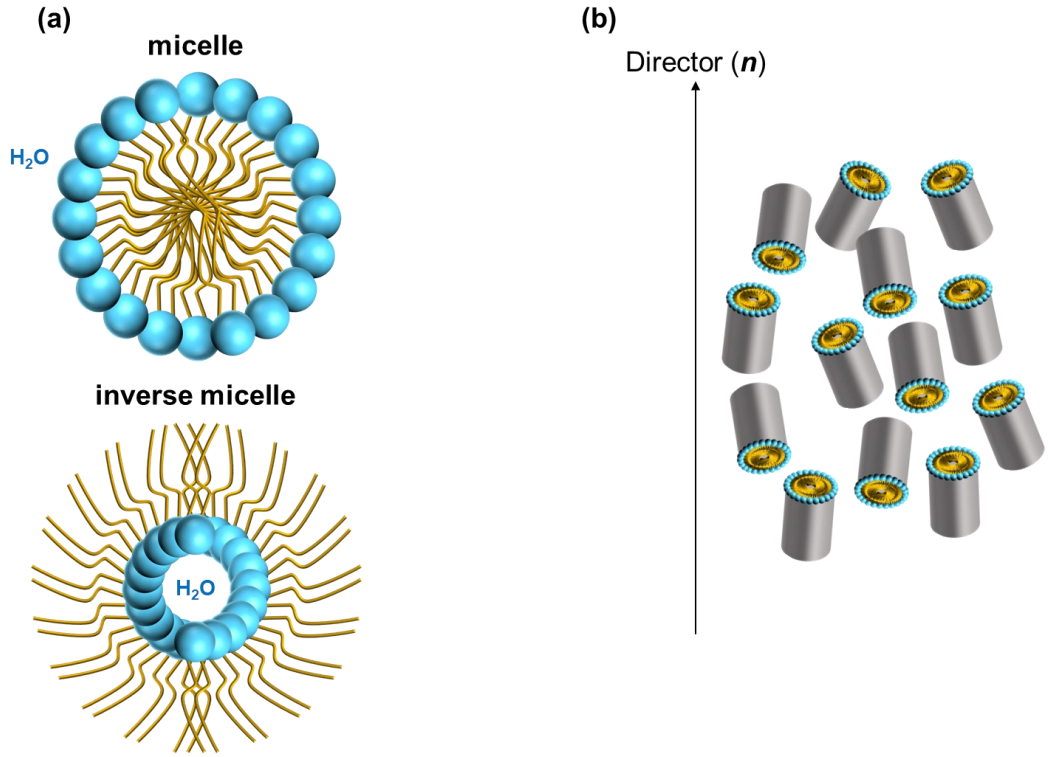

Figure 1-3. Schematic diagram of (a) micelle and inverse micelle phase; (b) lyotropic nematic phase.

As the concentration increases, the concentration of micelle in the solvent also increases gradually. To reduce and minimize the contact of the hydrophobic moiety with water, these micelles spontaneously form various secondary structures. The hexagonal is the first phase formed. If the concentration continues to increase a more ideal-ordered liquid crystal phase, the lamellar phase will appear. There are also intermediate phases between the hexagonal and lamellar phases, which have continuous three-dimensional channels called bicontinuous phases. The relationship between the formed liquid crystal phase and the concentration of amphiphilic molecules is shown in Figure 1-4.[26]

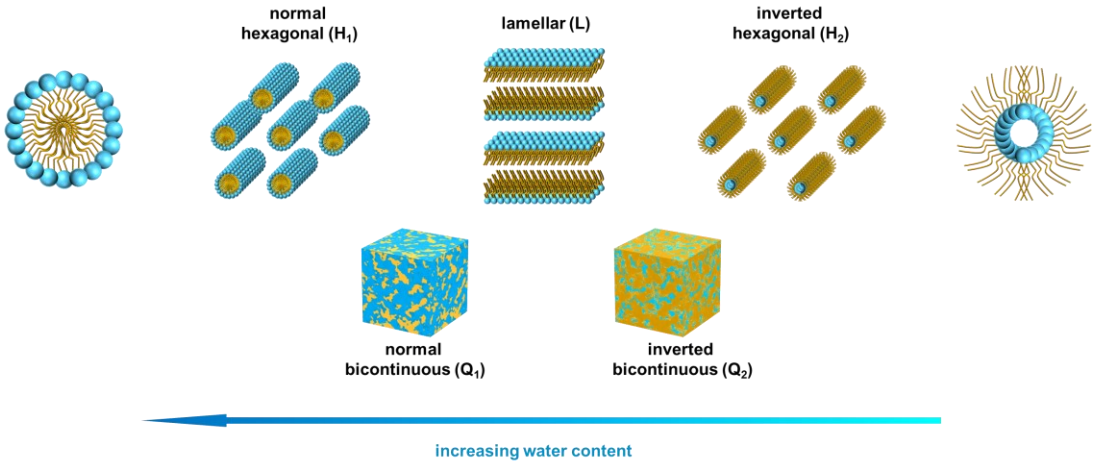

Figure 1-4. Common lyotropic liquid crystal phases formed by amphiphiles in water.

1.2.3. Polymer liquid crystal

Usually liquid crystal materials are low-molecular-weight compounds, hence they are also called monomer liquid crystals (MLCs). In contrast, when the polymer compounds exhibit liquid crystal properties, they are called polymer liquid crystals (PLCs) or liquid crystal polymer (LCP).[27,28] PLCs have received continuous attention as an emerging material platform in recent decades due to their easy processing and flexible molecular design properties from polymers and the structural order and anisotropy properties from liquid crystals. PLCs can be divided into main-chain-type PLCs and side-chain-type PLCs according to the position of the mesogens (rigid component) located in the polymer. As shown in Figure 1-5(a), the backbone of main-chain-type PLCs can be composed of only mesogens and flexible spacers. Generally, it has ultrahigh modulus and good thermal stability, making them ideal structural materials.[29] The backbone of side-chain-type PLCs is composed of flexible aliphatic polymers with mesogens located at the side chain positions (Figure 1-5(b)). Usually, it easily forms into phase-separated structures and abundant liquid crystal phases, making it excellent development platform for functional materials.

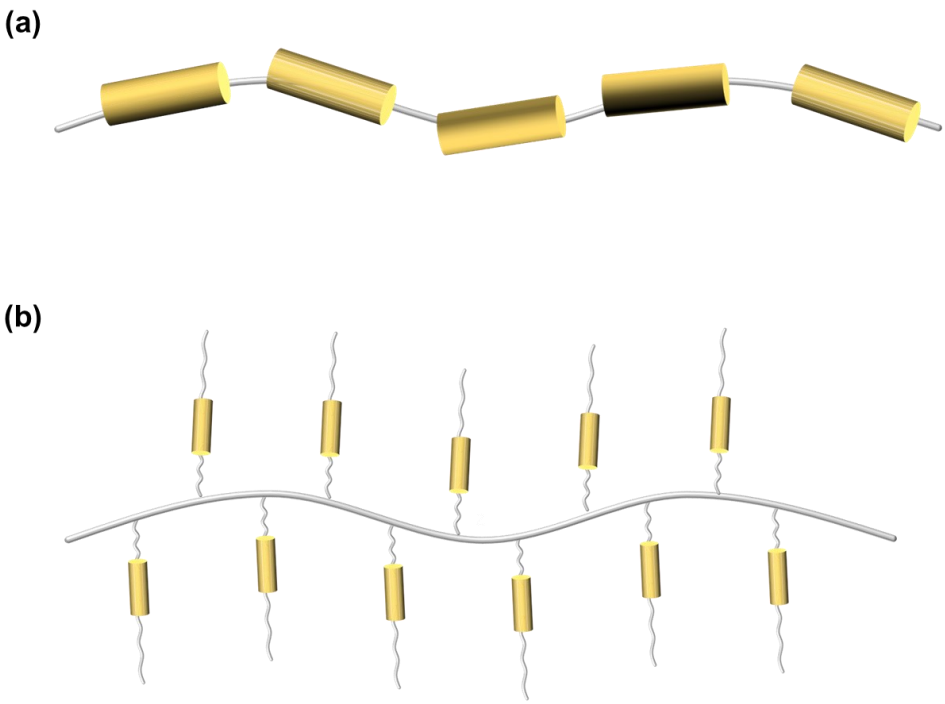

Figure 1-5. Schematic diagram of (a) main-chain-type PLC and (b) side-chain-type PLC.

1.3 Application of liquid crystals

Having fluidity and anisotropy simultaneously is the basis for their successful commercial applications of liquid crystal materials. After continuous development, liquid crystals have been successfully applied in display materials, catalysts, drug delivery, etc. As the research on liquid crystal materials, especially lyotropic liquid crystals and polymer liquid crystals, has gradually intensified, new application fields of liquid crystal materials continue to emerge. Among them, liquid crystal materials have huge advantages in the field of energy conversion.

1.3.1. Lyotropic liquid crystal-based conducting material

The development of efficient and environmentally friendly new energy conversion systems to replace traditional fossil fuel-based systems is still a challenge today. Lyotropic liquid crystal is gradually gaining attention in this field due to its ability to form long-range ordered structures at the nanoscale and is easy to make such ordered structures point in a specific direction as required. Compared with conventional non-ordered isotropic ion-conducting materials, lyotropic liquid crystal with the same ion transport unit has more uniform nanoscale domains and may form continuous transport channels in 1-, 2- or 3-dimensional space. This property can greatly improve the ion transport efficiency and the ionic conductivity in lyotropic liquid crystals.

More challenging work in the field of polymer membrane fuel cells (PEMFCs) is to develop ultrathin ionomer films with high ionic conductivity. Due to the important role played by the ionomer in PEMFCs, the requirements for its properties are different from those of the electrolyte bulk membrane. Due to its good self-assembly properties, the lyotropic liquid crystal has great potential in the fabrication of ultrathin ionomer films. Ichikawa et al. successfully obtained a lyotropic liquid crystal film with a bicontinuous phase, and its proton conductivity was as high as 10^{-1} S cm^{-1}.[30,31] Kato et al. fabricated ion-conducting thin films with columnar structures and demonstrated that the ionic conductivity parallel to the column axis was higher than that perpendicular to the column axis.[32,33]

1.3.2. Liquid crystal-based sensor

The fluid properties and the anisotropy caused by the orientational order of the molecules in the liquid crystal, enable it to respond to various external stimuli. These stimuli including light, temperature, pH, electromagnetic fields, and mechanical deformation may cause distortion of the director (***n***) for liquid

crystal phases. Taking the nematic phase as an example, the interaction between external stimuli and liquid crystal molecules produces elastic restoring force and can be described by the Frank–Oseen equation:

$$F_e = \frac{1}{2}[K_{11}(\nabla \cdot n)^2 + K_{22}(n \cdot \nabla \times n)^2 + K_{33}(n \times \nabla \times n)^2] \quad (1\text{-}1)$$

where F_e is the elastic energy, K_{11}, K_{22} and K_{33} are the Frank's elastic constants associated with splay, twist and bend, respectively.[34] The degree of damage to the orientational order of liquid crystal molecules by external stimuli determines the magnitude of the elastic restoring force (F_e) generated. This forms the basis for liquid crystals as sensor materials.

There have been reports of sensors made of liquid crystal materials. Chen et al. fabricated a pH sensor by filling liquid crystal molecules into a copper grid on a glass substrate.[35] Gleeson et al. fabricated strain sensors with high strain-optic coefficients s based on liquid crystal elastomers.[36] Schenning et al. developed a temperature/humidity sensor based on H-bonded supramolecular cholesteric liquid crystal that can fast-respond through color changes.[37] Most of these sensors developed based on liquid crystal materials have the characteristics of easy fabrication, fast response, and low cost, which make them great advantages compared with traditional sensors that require high-precision instruments for fabrication.

1.4 Catalyst layer (CL) and ionomer

The most serious challenge in the development of commercially viable fuel cell vehicles (FCVs) is the high cost of platinum (Pt)-based catalysis. Therefore, great efforts have been devoted to reducing the Pt loading in the cathode CL and improving the utilization efficiency of Pt in past decades.[38,39,40,41,42,43] However, membrane electrode assembly (MEA) with low Pt loadings generally suffers significant performance losses due to the huge oxygen transport resistance in the cathode CL.[44,45,46] Therefore, in-depth exploration of the oxygen transport behavior in the cathode CL is of great significance for optimizing the electrode nanostructure and improving the performance of polymer electrolyte membrane fuel cells (PEMFCs).

The total oxygen transport resistance (R_{total}) in the cathode of PEMFCs can be divided into several components, i.e., the transport resistance in channel ($R_{Channel}$), in GDLs (R_{GDLs}), and in CLs (R_{CLs}).[44,45,46] Among them, R_{CLs} is proven to be the main contributor to R_{total}.[47,48,49] Figure 1-6 is a schematic diagram of an MEA, which consists of PEM, ORR catalyst and ionomers. There are two kinds of pores in the CLs,

one is the primary pores possessed by the catalyst particle itself, and the other is the secondary pores formed between the catalyst particles covered by the ionomer thin film. Therefore, the oxygen transport resistance through CL can be divided into two types, i.e., the diffusion resistance of oxygen in the primary and secondary pores, denoted as the bulk transport resistance R_{Bulk}, and the permeation resistance of oxygen through the ionomer membrane, denoted as the local resistance, R_{Local}.

Although both of these two different mechanisms of oxygen transport resistance are important for PEMFC, studies have shown that R_{Local} is the dominant contributor at low Pt loading MEA. [50,51,52] With decreasing Pt loading, concentration polarization will severely deteriorate the performance of PEMFC, so it is necessary to reduce the oxygen transport resistance in CL, especially R_{Local}. An effective approach is to adjust the ratio of ionomer to carbon (I/C).[53,54] Once a is too large, the massive aggregation of the ionomer will cause additional local transport resistance, meaning that oxygen must pass through a thicker ionomer film to reach the active sites of the Pt catalyst.[55] When I/C is in an appropriate range, not only the ionomer will cover the catalyst particle surface more uniformly but also R_{Local} will be significantly reduced.[56] However, simply reducing I/C to reduce R_{Local} results in a sacrifice of proton transport efficiency in the CL. Therefore, it is of great significance to develop ionomer materials with high proton conductivity that can uniformly cover the surface of catalyst particles.

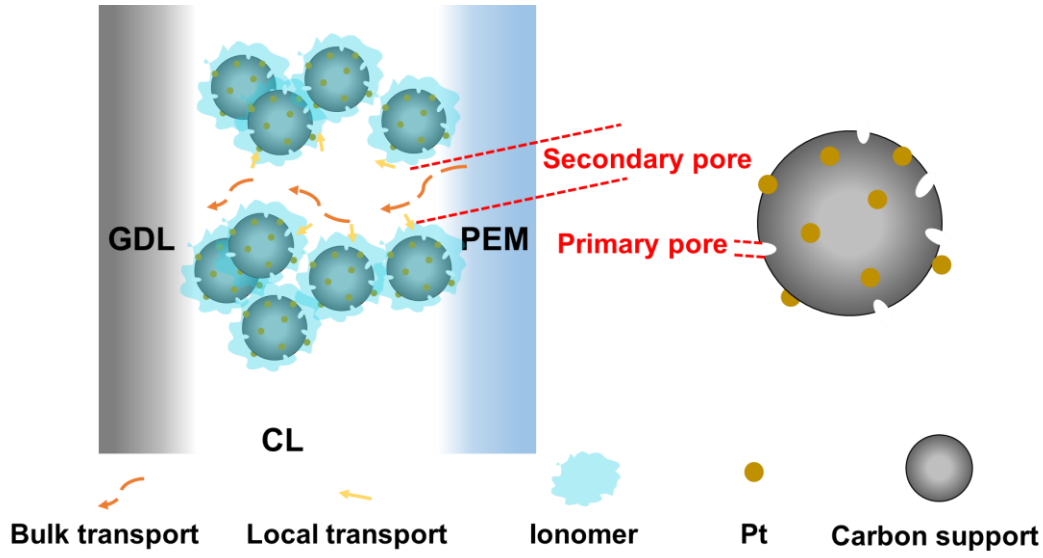

Figure 1-6. Schematic diagram of the membrane electrode assembly (MEA).

The electrode reaction of PEFCs can only occur at the three-phase boundary where the fuel or oxidant, catalyst and polymer electrolyte are in contact with each other (Figure 1-7). In order to let the reaction proceed smoothly, a highly proton-conductive material must be present at the three-phase

boundary. The ionomer film is very thin compared to polymer electrolyte membranes, generally. This requires the ionomer to have a high proton conductivity even in a very thin state.

At present, the most used proton-conductive polymer material is perfluorosulfonic acid (PFSA), which is designed and developed by DuPont, and is commonly called Nafion.[57,58,59] The structure of Nafion is shown in Figure 1-8. Nafion is a copolymer obtained by radical polymerization. One of the comonomers is tetrafluoroethylene (TFE), and another comonomer has a perfluorovinyl ether side chain terminated with a sulfonic acid group. The basic strategy for designing PFSA as represented by Nafion is to make the hydrophobic main chain and the hydrophilic side chain form microphase separation under some conditions.[60] As shown in Figure 1-9, the sulfonic groups will gradually come together to form clusters under humidified conditions. Protons and water molecules can move in PFSA through these clusters. The formation of these clusters allows water molecules to pass freely in PFSA and promotes the transport of protons, thus giving PFSA excellent proton conductivity. In addition, by adjusting the ratio of x can get PFSA with better mechanical strength and higher proton conductivity.[61]

Although Nafion has excellent proton conductivity and good chemical and mechanical stability, there are still some defects such as high cost, difficult to recycle and methanol permeability that limit the wide application of Nafion[57,58]. In addition, a significant decrease in the proton conductivity when Nafion is made into a thin film was reported.[62,63,64] Therefore, it is necessary to develop a new material that can be used as an ionomer for replacing Nafion.

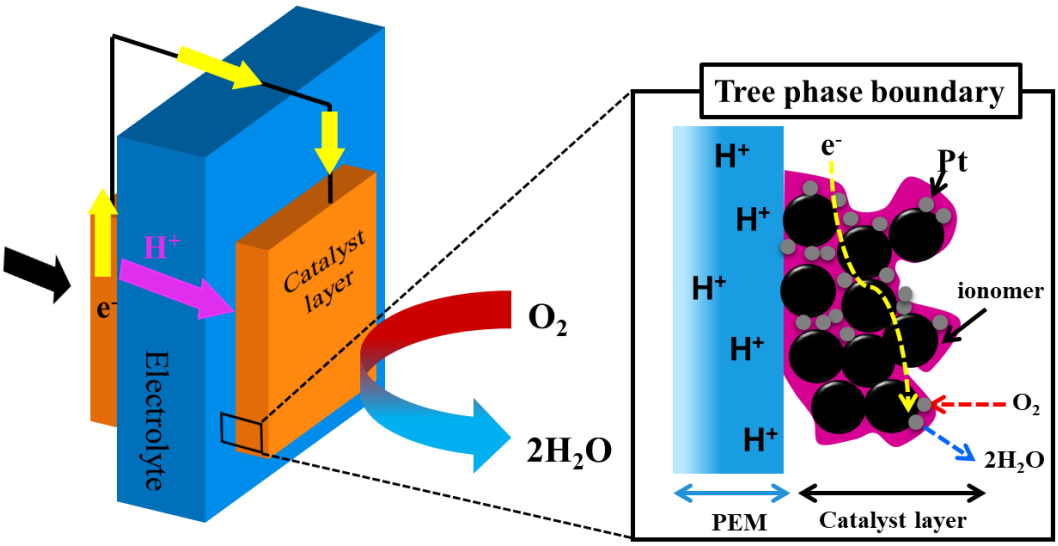

Figure 1-7. Schematic diagram of PEFC and three phase boundary.

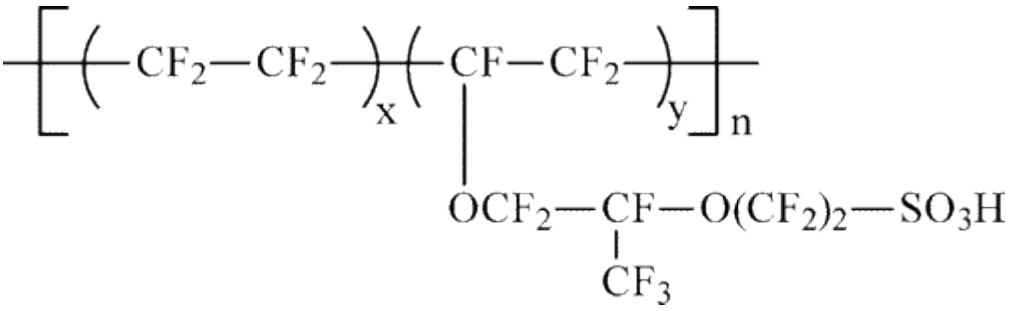

Figure 1-8. Chemical structure of Nafion.

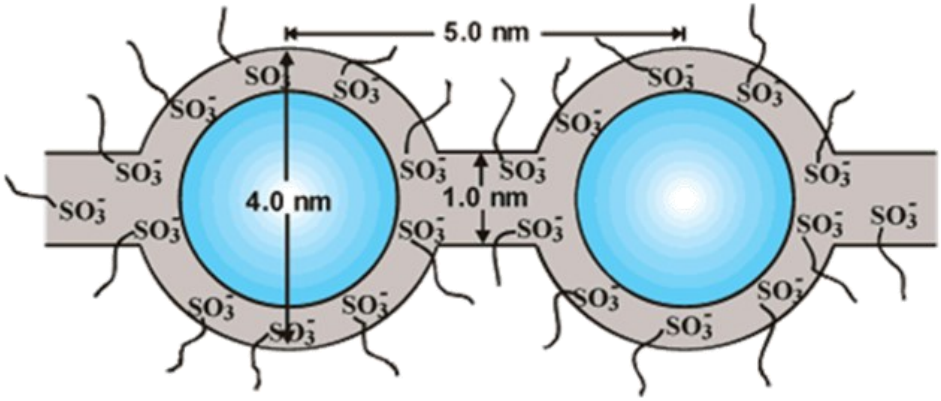

Figure 1-9. Schematic diagram of cluster structure in perfluorosulfonic acid polymers.[57]

1.5 Enhancement of proton conductivity in ionomer thin films

Based on the success of Nafion, most ionomer designs are also based on microphase separation between hydrophobic and hydrophilic components. However, these ionomers usually do not possess well-defined long-range ordered structures, which makes it difficult to deeply discuss the relationship between structure and proton conductivity.[57,65,58,61,66,67,68]

Ikkala et al. observed a temperature-dependent change in proton conductivity in PS-block-P4VP(MSA)$_{1.0}$(PDP)$_{1.0}$ (PS, polystyrene; P4VP, poly(4-vinly pyridine); MSA, methane sulfonic acid; PDP, pentadecylphenol), which they attributed to the order-disorder or order-to-order structural changes in PS-block-P4VP(MSA)$_{1.0}$(PDP)$_{1.0}$ during the phase transition (Figure 1-10(a)).[69] This study was published in 1998, and since then researchers began to realize the effect of ordered structure on proton conductivity. In 2004, Picken et al. observed a lyotropic nematic phase in an aqueous solution of poly-(p-

sulfophenylene-terephthalamide), unfortunately, they did not investigate the proton conductivity.[70] This is the earliest report of sulfonated polymers as lyotropic liquid crystals. In 2009, Nagao et al. reported that the molecular orientation of oligo[(1,2-propanediamine)-alt-(oxalic acid)] thin film can be altered based on the interaction between the substrate and the material interface, and that proton conductivity can be improved (Figure 1-10(b)).[71,72,73] In 2010, Park and Balsara observed in-plane and out-of-plane anisotropic proton conductivity in poly(styrenesulfonate-b-methylbutylene) copolymer films through pressing, electric-field, and shear-aligned methods (Figure 1-10(c)).[74] In 2011, Rikukawa et al. observed anisotropic proton conductivity and swelling behavior in sulfonated poly(4-phenoxybenzoyl-1,4-phenylene)s (s-PPBPs) and attributed them to lyotropic liquid crystallinity (Figure 1-10(d)).[75] In 2015, Matsui et al. used poly(N-dodecylacrylamide-co-acrylic acid) to obtain thin films with well-defined lamellar structures and demonstrated a huge difference in proton conductivity between in-plane and out-of-plane directions (Figure 1-12(e)).[76] The in-plane proton conductivity is as high as 5.1×10^{-2} S cm^{-1}, which is excellent for materials using carboxylic acid as a proton source. Recently, porous materials such as porous coordination polymers (PCP), metal-organic frameworks (MOF) and covalent organic frameworks (COFs) have become a new platform for the development of proton-conducting materials due to their excellent crystallinity, good stability, and pre-designed structures.[77] Li et al. achieved an intrinsic proton conductivity of 2.9×10^{-2} S cm^{-1} with an activation energy of only 0.17 eV by anchoring sulfonic acid groups on the inner wall of the COF.[78] A growing number of similar studies have demonstrated that the organized structure will directly affect the way that protons transported within materials, which will contribute to the understanding of proton conduction mechanisms and the development of high-performance proton-conducting materials.

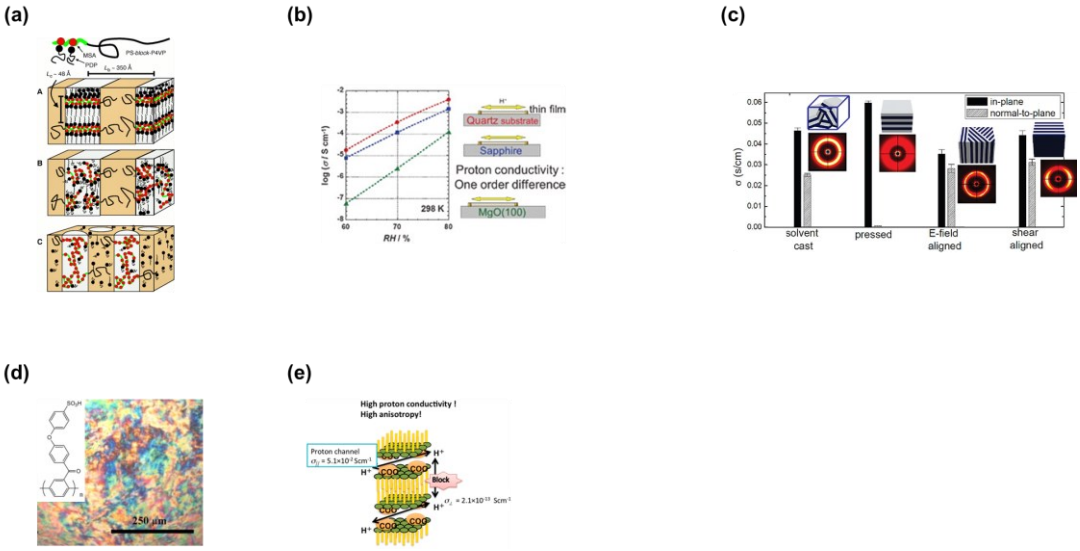

Figure 1-10. (a) schematic diagram of the self-organized structures of PS-block-P4VP(MSA)$_{1.0}$(PDP)$_{1.0}$.[69] (b) substrate-dependence proton conductivity in oligo[(1,2-propanediamine)-alt-(oxalic acid)] thin film.[73] (c) 2D small angle X-ray scattering profiles and in-plane and normal-to-plane conductivity of as-cast and aligned samples.[74] (d) chemical structure and optical polarization micrograph of S-PPBP in DMSO.[75] (e) Schematic of multilayer film of poly(N-dodecylacrylamide-co-acrylic acid) by Langmuir–Blodgett method with highly anisotropic proton conduction.[76]

1.6 Alkyl sulfonated polyimides (ASPIs)

Many studies show that many main-chain-type sulfonated polyimides (SPIs) (Figure 1-11(a)) have the ability to exhibit high proton conductivity comparable to that of Nafion. In 2003,Watanabe et al. synthesized a fluorenyl group contained sulfonated polyimide with a proton conductivity as high as 1.67 S cm^{-1} at 120 °C and 100% RH.[79] One year later, the same research group again synthesized a sulfonated polyimide with trifluoromethyl groups, which achieved better oxidative stability and mechanical strength than the previous one, although the proton conductivity was reduced (0.2 S cm^{-1} at 30−140 °C).[80] After that, Ando et al. first demonstrated the existence of ordered liquid crystal phases in fully aromatic and semi-aliphatic polyimides (PIs) molecules by grazing incidence wide-angle X-ray scattering.[81] However, these main-chain-type SPIs are easily degraded under fuel cell operating conditions, resulting in a decrease in fuel cell performance.[82] To solve this problem, attempts to introduce sulfonic acid groups into the side chains of SPIs instead of the main chains have achieved success. In 2004, Okamoto et al. synthesized two isomers of side-chain type SPIs with proton conductivity as high as 0.1 S cm^{-1} (at 50 °C

and 90% RH) and better water stability than main-chain type SPIs.[83,84] Such side-chain-type SPIs (Figure 1-11(b)), also known as Alkyl sulfonated polyimides (ASPIs), not only have good proton conductivity and stability but also easily obtain ultrathin films with self-assembled ordered structures due to their lyotropic liquid crystal property (as shown in Figure 1-4), making them an ideal candidate for ionomer material.

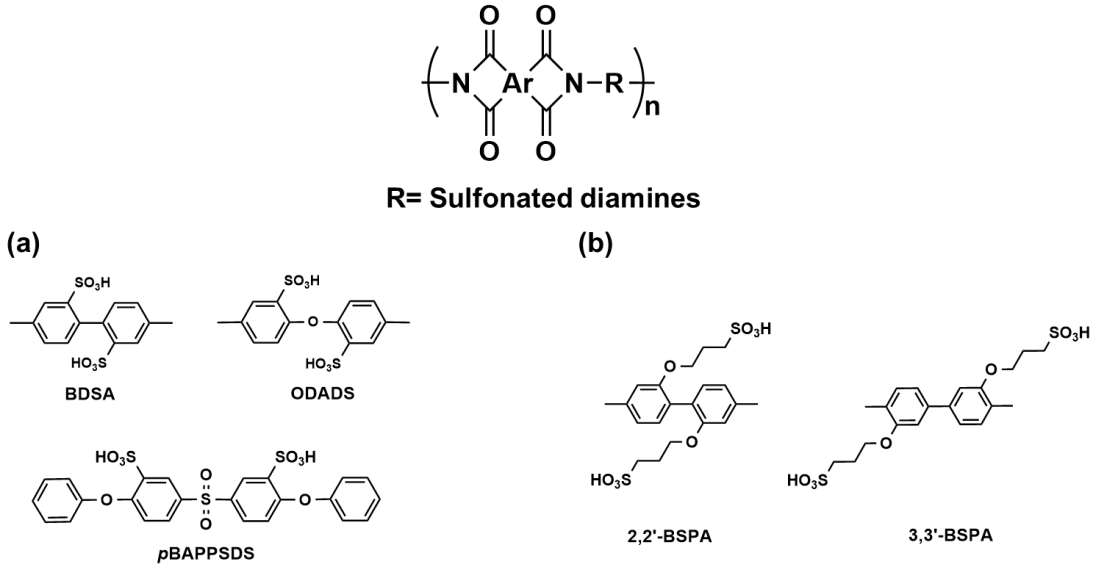

Figure 1-11. Chemical structure of (a) main-chain-type ASPIs and (b) side-chain-type ASPIs

In 2014, Krishnan et al. obtained proton conductivity as high as 0.26 S cm^{-1} (at 25 °C and 95% RH) in the direction parallel to the substrate surface in ASPI thin film, which is an order of magnitude higher than its bulk membrane. They attribute this to the formation of a lamellar ordered structure parallel to the substrate under humidified conditions and propose that the formation of this ordered structure is driven by lyotropic liquid crystal property (Figure 1-12(a)).[85] They proposed such a mechanism based on the study by Wegner on the lyotropic liquid crystal property of polymers with rigid backbone structures.[86] The highly hydrophilic and polar sulfonic acid groups in the side chain of ASPI provide it with sufficient solubility, and simultaneously, the main chain composed of aromatic rings makes the overall ASPI molecule appear rod-like and rigid. Further studies showed that molecular weight and molecular configuration have obvious effects on the structure of ASPI thin films. Both the studies by Krishnan et al. and Takakura et al. show that higher molecular weight in either fully aromatic or semi-aliphatic ASPIs will favor the formation of lamellar structures under humidified conditions, thereby improving proton transport in thin films (Figure 1-12(b)).[87,88] The work of Ando et al. demonstrated that fully aromatic PIs are more likely to form liquid crystal ordered domains while semi-aliphatic PIs can only form amorphous halos. This is due to that fully aromatic PIs have highly planar rod-like molecular structures whereas semi-aliphatic PIs have molecules

that are more curved and non-planar.[81] The work of Ono et al. demonstrated that fully aromatic ASPIs with planar backbones are more capable of forming well-defined lamellar ordered structures than fully aromatic ASPIs with bent backbones (Figure 1-12(c)).[89]

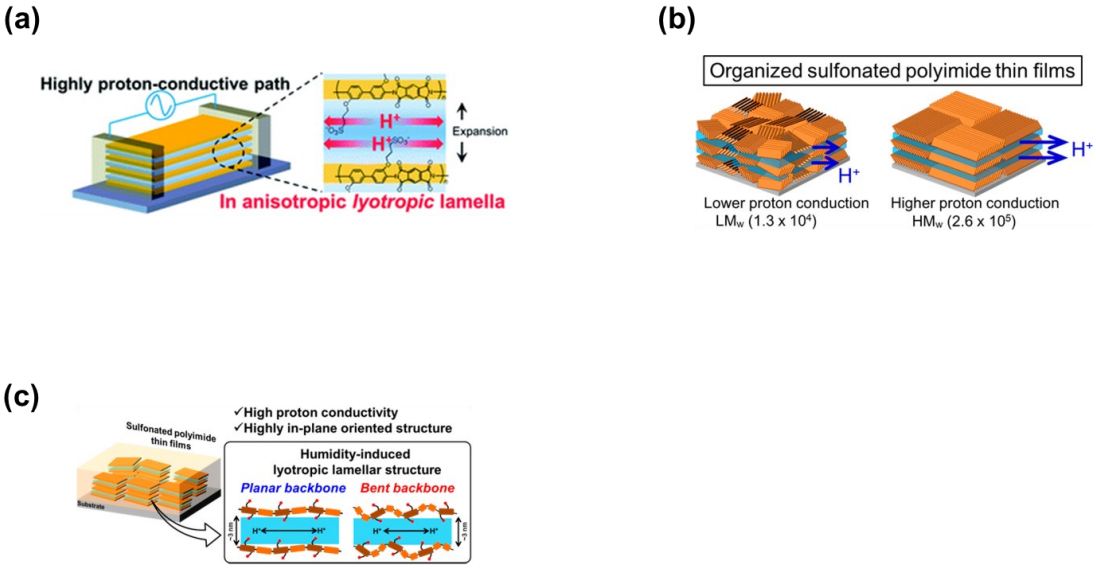

Figure 1-12. (a) schematic diagram of lamellar order structure in ASPI with high in-plane proton conductivity of 0.26 S cm^{-1} at 25 °C and 95% RH.[85] (b) schematic diagram of molecular weight dependence of proton conductivity and molecular order.[87] (c) schematic diagram of effect of main chain bending degree on the organized structure in ASPI thin films.[89]

1.7 New application field for ASPIs

As the interface between the surrounding environment and the human sensorium system, the human skin has an unparalleled ability to perceive changes in environmental stimuli and accurately distinguish between different stimuli.[90] To mimic this ability of human skin, a large number of different types of electronic sensors with the ability to detect external stimuli have been developed. Among them, the development of pressure sensors is of great importance for a wide range of applications such as wearable healthcare systems, human-machine interface devices, etc.[91,92]

There are generally several methods of converting pressure signals into electrical signals, the most well-known of which are piezoresistivity, capacitance, and piezoelectricity (Figure 1-13).[93,94] Piezoresistive sensors (Figure 1-13(a)), which work by converting the resistance change of a material into an electrical signal, have been widely studied due to their simple design and easy-to-read-out properties. When pressure is exerted on a piezoresistive sensor, its resistance change follows a power-

law relationship with the pressure, $R \propto F^{1/2}$, ensuring high sensitivity and wide operating range of the piezoresistive sensors at low pressure.[95] Capacitance (C), the charge storage capacity is usually described by C=εA/d, where ε is the dielectric constant, and A and d are the area and the distance between the two electrodes, respectively (Figure 1-13(b)). Changes in pressure will easily lead to changes in the d or contact A between the two electrodes, making the capacitance sensor highly sensitive.[96] Piezoelectricity refers to the phenomenon that certain materials generate electric charges due to the occurrence of electrical dipole moments under pressure. Sensors fabricated based on this mechanism usually have high sensitivity and rapid response (Figure 1-13(c)).[97,98,99]

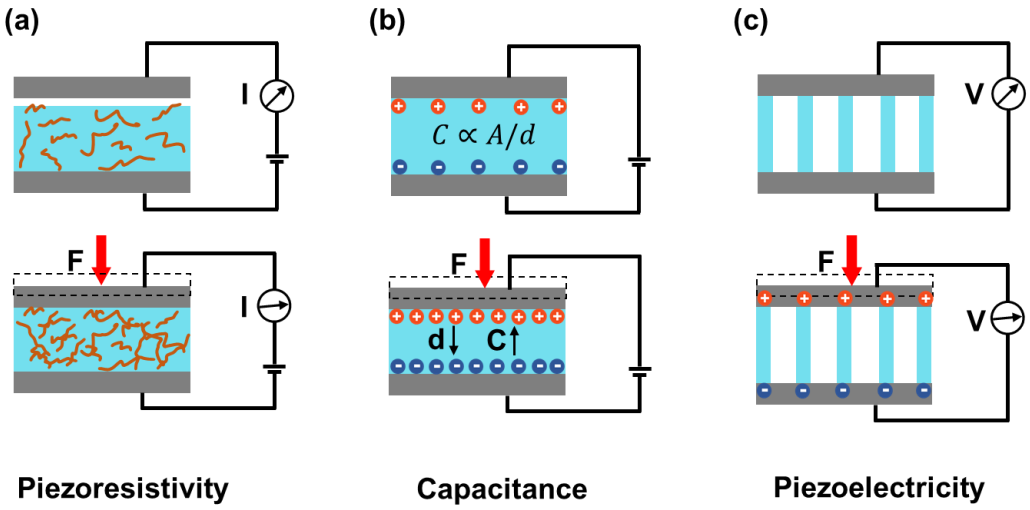

Figure 1-13. Schematic diagram of (a) piezoresistivity, (b) capacitance, and (c)piezoelectricity transduction methods.

Advanced flexible sensing materials should be able to respond to multiple stimuli, like human skin can sense not only pressure but also humidity, temperature and even pH.[100,101] Although such functions can be achieved by integrating multiple single-function sensors on the same substrate, the development of new materials capable of sensing multiple stimuli simultaneously remains a major research direction.

ASPIs are naturally sensitive to ambient temperature and humidity as an ionic (proton) conductor material. Moreover, ASPIs can form lamellar ordered structure driven lyotropic liquid crystalline property, when applied pressure perpendicular to the ASPI thin film plane, the lamellar distance will decrease accordingly, resulting in a change in proton conductivity. This makes them a kind of potential stimulus-responsive material.

1.8 Research objectives

Although our previous work demonstrated the promotion of protons in ionomer thin films by the lyotropic liquid crystal ordered structure, most of these works have focused on fully aromatic ASPIs. The effects of introducing aliphatic rings into the backbone of ASPIs on lyotropic liquid crystal properties and proton conductivity are still inadequate. At the same time, previous studies have also shown that the increased molecular weight is beneficial to the formation of lamella structure, furthermore lamella structure has not been observed in oligomers so far. Inspired by this, the author focused on ordered structure and proton conductive properties of sulfonated semi-alicyclic poly-/oligo-imide thin films in this thesis. The research objectives were summarized as follows:

(1) To enhance the mechanical stability of semi-alicyclic polyimide thin film in water solvent, cross-linking is done through a Diels–Alder (D-A) reaction. The high proton conductivity is preserved because the sulfonic acid groups which act as proton transport carriers are retained and no non-ionically conductive moieties are introduced.

(2) The relationship between ordered structure and proton conductivity was investigated by introducing a cyclopentane structure into the imide backbone. The cyclopentane structure, compared to the previous cyclohexane structure which enhances linear conformation of backbone confirmed by density functional theory (DFT) calculation, can be anticipated for the changes in the molecular structure and organization by the lyotropic LC property.

(3) Explore the possibilities of ASPIs as potential pressure-sensitive materials. Qualitative and quantitative measurements were made of its basic properties.

1.9 Outline of thesis

In chapter 1, the general introduction of this thesis summarized the recent advancement of PEMFCs and emphasized the state-of-the-art ionomer thin films.

In chapter 2, a cross-linked semi-alicyclic polyimide that can be stable in water was synthesized via D-A reaction. The effect of the cross-linked structure on the water uptake, proton conductivity and lyotropic LC properties of the thin films was investigated.

In chapter 3, the relationship between ordered structure and proton conductivity was investigated in

sulfonated semi-alicyclic oligoimide thin film. And the structural differences between fully aromatic ASPIs and semi-alicyclic poly-/oligo-imide are summarized and compared.

In chapter 4, a system was established to measure the sensitivity of ASPIs to pressure. And investigated the change of the conductivities of ASPIs under pressure conditions.

In chapter 5, the overall finding of this study was presented. The findings provide new insights for understanding the proton conductivity and lyotropic LC properties of semi-alicyclic poly-/oligo-imide thin films. Besides, a simple and easy-to-implement cross-linked structure resulting from the D-A reaction was demonstrated to improve mechanical stability of semi-alicyclic polyimide thin film in water while maintaining high proton conductivity. In addition, it is proved that ASPIs can be used as pressure-sensitive materials under certain humidity conditions.

References

1. Timothy J. Sluckin, David A. Dunmur & Horst Stegemeyer. Crystals That Flow. Crystals That Flow (2004). doi:10.1201/9780203022658.
2. Yadav, S. P. & Singh, S. Carbon nanotube dispersion in nematic liquid crystals: An overview. Prog. Mater. Sci. 80, 38–76 (2016).
3. Oswald, P. & Pieranski, P. NEMATIC AND LIQUID CRYSTALS LIQUID CRYSTALS.
4. Ohm, C., Brehmer, M. & Zentel, R. Liquid crystalline elastomers as actuators and sensors. Adv. Mater. 22, 3366–3387 (2010).
5. Hussain, A., Pina, A. S. & Roque, A. C. A. Bio-recognition and detection using liquid crystals. Biosens. Bioelectron. 25, 1–8 (2009).
6. Andrienko, D. Introduction to liquid crystals. J. Mol. Liq. 267, 520–541 (2018).
7. Collings, P. J. Point and line disclinations in models of the blue phases. Mol. Cryst. Liq. Cryst. Sci. Technol. Sect. A Mol. Cryst. Liq. Cryst. 292, 155–162 (1997).
8. Hu, G. et al. Photopolymerisable liquid crystals for additive manufacturing. Addit. Manuf. 55, 102861 (2022).
9. Zhou, M., Gong, Y., Yuan, Y. & Zhang, H. Research on Circularly Polarized Luminescent and Clustering-Triggered Emission Properties of Cholesteryl Benzoate. J. Phys. Chem. C 2022, 15485–15490 (2022).
10. Lagerwall, J. P. F. & Scalia, G. A new era for liquid crystal research: Applications of liquid crystals in soft matter nano-, bio- and microtechnology. Curr. Appl. Phys. 12, 1387–1412 (2012).
11. Collings, P. J. & Hird, M. Introduction to liquid crystals: Chemistry and physics. Introduction to Liquid Crystals: Chemistry and Physics vol. 3 (2017).
12. Sackmann, H. Plenary lecture: Smectic liquid crystals: A historical review. Liq. Cryst. 5, 43–55 (1989).
13. Bushby, R. J. & Kawata, K. Liquid crystals that affected the world: Discotic liquid crystals. Liq. Cryst. 38, 1415–1426 (2011).
14. Gin, D. L. et al. Recent advances in the design of polymerizable lyotropic liquid-crystal assemblies for heterogeneous catalysis and selective separations. Adv. Funct. Mater. 16, 865–878 (2006).
15. Gin, D. L., Pecinovsky, C. S., Bara, J. E. & Kerr, R. L. Functional lyotropic liquid crystal materials. Struct. Bond. 128, 181–222 (2007).
16. Tiddy, G. J. T. Surfactant-water liquid crystal phases. Phys. Rep. 57, 1–46 (1980).
17. Seddon, J. M. Structure of the inverted hexagonal (HII) phase, and non-lamellar phase transitions of lipids. BBA - Rev. Biomembr. 1031, 1–69 (1990).
18. Soberats, B. et al. Ionic Switch Induced by a Rectangular-Hexagonal Phase Transition in Benzenammonium Columnar Liquid Crystals. J. Am. Chem. Soc. 137, 13212–13215 (2015).
19. Yoshio, M., Mukai, T., Ohno, H. & Kato, T. One-Dimensional Ion Transport in Self-Organized Columnar Ionic Liquids. J. Am. Chem. Soc. 126, 994–995 (2004).
20. Kato, T. et al. Transport of ions and electrons in nanostructured liquid crystals. Nat. Rev. Mater. 2, (2017).
21. Lee, T. J. et al. Stability of Lyotropic Phases with Curved Interfaces. J. Chem. Phys. Lett 93, 447 (1989).
22. Prieve, D. C., Prieve & C., D. Intermolecular and surface forces with applications to colloidal and

biological systems. JCIS 116, 300 (1987).
23. Ichikawa, T. et al. Design of Ionic Liquid Crystals Forming Normal-Type Bicontinuous Cubic Phases with a 3D Continuous Ion Conductive Pathway. Crystals 9, 309 (2019).
24. Maekawa, A., Kobayashi, T. & Ichikawa, T. Gyroid nanostructured soft membranes formed by controlling the degree of crosslinking polymerization of bicontinuous cubic liquid-crystalline monomers. Polym. J. 53, 463–470 (2021).
25. Uemura, N. et al. Double-Gyroid Nanostructure Formation by Aggregation-Induced Atropisomerization and Co-Assembly of Ionic Liquid-Crystalline Amphiphiles. Angew. Chemie - Int. Ed. 59, 8445–8450 (2020).
26. Benedicto, A. D. & O'Brien, D. F. Bicontinuous cubic morphologies in block copolymers and amphiphile/water systems: Mathematical description through the minimal surfaces. Macromolecules 30, 3395–3402 (1997).
27. Brostow, W. Properties of polymer liquid crystals: choosing molecular structures and blending. Polymer (Guildf). 31, 979–995 (1990).
28. White, T. J. & Broer, D. J. Programmable and adaptive mechanics with liquid crystal polymer networks and elastomers. Nat. Mater. 2015 1411 14, 1087–1098 (2015).
29. Chiellini, E. & Laus, M. Main Chain Liquid Crystalline Semiflexible Polymers. Handb. Liq. Cryst. Set 26–51 (2008) doi:10.1002/9783527619276.CH1BD.
30. Kobayashi, T., Li, Y. X., Ono, A., Zeng, X. B. & Ichikawa, T. Gyroid structured aqua-sheets with sub-nanometer thickness enabling 3D fast proton relay conduction. Chem. Sci. 10, 6245–6253 (2019).
31. Kobayashi, T. et al. Gyroid-Nanostructured All-Solid Polymer Films Combining High H+ Conductivity with Low H2 Permeability. Macromol. Rapid Commun. 42, 2100115 (2021).
32. Yoshio, M. et al. One-dimensional ion-conductive polymer films: Alignment and fixation of ionic channels formed by self-organization of polymerizable columnar liquid crystals. J. Am. Chem. Soc. 128, 5570–5577 (2006).
33. Kuo, D. et al. Switching of ionic conductivities in columnar liquid-crystalline anilinium salts: effects of alkyl chains, ammonium cations and counter anions on thermal properties and switching temperatures. Mol. Syst. Des. Eng. 4, 342–347 (2019).
34. Adler, J. H., Atherton, T. J., Emerson, D. B. & MacLachlan, S. P. An energy-minimization finite-element approach for the Frank-Oseen model of nematic liquid crystals. SIAM J. Numer. Anal. 53, 2226–2254 (2015).
35. Chen, W. L., Ho, T. Y., Huang, J. W. & Chen, C. H. Continuous monitoring of pH level in flow aqueous system by using liquid crystal-based sensor device. Microchem. J. 139, 339–346 (2018).
36. Mistry, D. et al. Isotropic Liquid Crystal Elastomers as Exceptional Photoelastic Strain Sensors. Macromolecules 53, 3709–3718 (2020).
37. Herzer, N. et al. Printable optical sensors based on H-bonded supramolecular cholesteric liquid crystal networks. J. Am. Chem. Soc. 134, 7608–7611 (2012).
38. Luo, L. et al. Composition-Graded PdxNi1-x Nanospheres with Pt Monolayer Shells as High-Performance Electrocatalysts for Oxygen Reduction Reaction. ACS Catal. 7, 5420–5430 (2017).
39. Tian, R. et al. Icosahedral Pt–Ni Nanocrystalline Electrocatalyst: Growth Mechanism and Oxygen Reduction Activity. ChemSusChem 11, 1015–1019 (2018).
40. Luo, X. et al. Thermal annealing synthesis of double-shell truncated octahedral Pt-Ni alloys for oxygen reduction reaction of polymer electrolyte membrane fuel cells. Front. Energy 14, 767–777 (2020).
41. Zhu, F. et al. Improving the High-Current-Density Performance of PEMFC through Much Enhanced

Utilization of Platinum Electrocatalysts on Carbon. ACS Appl. Mater. Interfaces 12, 26076–26083 (2020).
42. Chowdhury, A. et al. Linking Perfluorosulfonic Acid Ionomer Chemistry and High-Current Density Performance in Fuel-Cell Electrodes. ACS Appl. Mater. Interfaces 13, 42579–42589 (2021).
43. Woo, S. et al. Current understanding of catalyst/ionomer interfacial structure and phenomena affecting the oxygen reduction reaction in cathode catalyst layers of proton exchange membrane fuel cells. Curr. Opin. Electrochem. 21, 289–296 (2020).
44. Baker, D. R., Caulk, D. A., Neyerlin, K. C. & Murphy, M. W. Measurement of Oxygen Transport Resistance in PEM Fuel Cells by Limiting Current Methods. J. Electrochem. Soc. 156, B991 (2009).
45. Yan, X. et al. Flow field design with 3D geometry for proton exchange membrane fuel cells. Appl. Therm. Eng. 147, 1107–1114 (2019).
46. Kongkanand, A. & Mathias, M. F. The Priority and Challenge of High-Power Performance of Low-Platinum Proton-Exchange Membrane Fuel Cells. J. Phys. Chem. Lett. 7, 1127–1137 (2016).
47. Yarlagadda, V. et al. Boosting Fuel Cell Performance with Accessible Carbon Mesopores. ACS Energy Lett. 3, 618–621 (2018).
48. Kodama, K., Nagai, T., Kuwaki, A., Jinnouchi, R. & Morimoto, Y. Challenges in applying highly active Pt-based nanostructured catalysts for oxygen reduction reactions to fuel cell vehicles. Nat. Nanotechnol. 16, 140–147 (2021).
49. Sun, X. et al. Influence of platinum dispersity on oxygen transport resistance and performance in PEMFC. Electrochim. Acta 332, 135474 (2020).
50. Weber, A. Z. et al. A Critical Review of Modeling Transport Phenomena in Polymer-Electrolyte Fuel Cells. J. Electrochem. Soc. 161, F1254–F1299 (2014).
51. Weber, A. Z. & Kusoglu, A. Unexplained transport resistances for low-loaded fuel-cell catalyst layers. J. Mater. Chem. A 2, 17207–17211 (2014).
52. Sabharwal, M. et al. Analysis of Catalyst Layer Microstructures: From Imaging to Performance. Fuel Cells 16, 734–753 (2016).
53. Yu, H., Bonville, L. & Maric, R. Analysis of H 2 /Air Polarization Losses of Low-Platinum-Loading Cathodes with Various I/C Ratios and Carbon Supports . J. Electrochem. Soc. 165, J3318–J3334 (2018).
54. Sun, C.-N., More, K. L., Veith, G. M. & Zawodzinski, T. A. Composition Dependence of the Pore Structure and Water Transport of Composite Catalyst Layers for Polymer Electrolyte Fuel Cells. J. Electrochem. Soc. 160, F1000–F1005 (2013).
55. Wang, C. et al. Respective Influence of Ionomer Content on Local and Bulk Oxygen Transport Resistance in the Catalyst Layer of PEMFCs with Low Pt Loading. J. Electrochem. Soc. 166, F239–F245 (2019).
56. Hitchcock, A. P. et al. Characterizing automotive fuel cell materials by soft X-ray scanning transmission X-ray microscopy. AIP Conf. Proc. 1696, (2016).
57. Hsu, W. Y. & Gierke, T. D. Ion transport and clustering in nafion perfluorinated membranes. J. Memb. Sci. 13, 307–326 (1983).
58. Kreuer, K. D. On the development of proton conducting polymer membranes for hydrogen and methanol fuel cells. J. Memb. Sci. 185, 29–39 (2001).
59. Mauritz, K. A. & Moore, R. B. State of understanding of Nafion. Chem. Rev. 104, 4535–4585 (2004).
60. Gierke, T. D., Munn, G. E. & Wilson, F. C. Morphology in Nafion Perfluorinated Membrane Products, As Determined By Wide- and Small-Angle X-Ray Studies. J. Polym. Sci. Part A-2, Polym. Phys. 19, 1687–1704 (1981).

61. Hickner, M. A., Ghassemi, H., Kim, Y. S., Einsla, B. R. & McGrath, J. E. Alternative polymer systems for proton exchange membranes (PEMs). Chem. Rev. 104, 4587–4611 (2004).
62. Siroma, Z. et al. Depression of proton conductivity in recast Nafion® film measured on flat substrate. J. Power Sources 189, 994–998 (2009).
63. Shen, S. et al. Influence of Equivalent Weight of Ionomer on Proton Conduction Behavior in Fuel Cell Catalyst Layers. J. Electrochem. Soc. 166, F724–F728 (2019).
64. Paul, D. K., Fraser, A. & Karan, K. Towards the understanding of proton conduction mechanism in PEMFC catalyst layer: Conductivity of adsorbed Nafion films. Electrochem. commun. 13, 774–777 (2011).
65. Rikukawa, M. & Sanui, K. Proton-conducting polymer electrolyte membranes based on hydrocarbon polymers. Prog. Polym. Sci. 25, 1463–1502 (2000).
66. Yang, Y. & Holdcroft, S. Synthetic strategies for controlling the morphology of proton conducting polymer membranes. Fuel Cells 5, 171–186 (2005).
67. Chang, Y. et al. Aromatic Ionomers with Highly Acidic Sulfonate Groups: Acidity, Hydration, and Proton Conductivity. Macromolecules 44, 8458–8469 (2011).
68. Allen, F. I. et al. Morphology of hydrated as-cast Nafion revealed through cryo electron tomography. ACS Macro Lett. 4, 1–5 (2015).
69. Ruokolainen, J. et al. Switching supramolecular polymeric materials with multiple length scales. Science (80-.). 280, 557–560 (1998).
70. Viale, S., Best, A. S., Mendes, E., Jager, W. F. & Picken, S. J. A supramolecular nematic phase in sulfonated polyaramides. Chem. Commun. 4, 1596–1597 (2004).
71. Nagao, Y., Naito, N., Iguchi, F., Sata, N. & Yugami, H. Synthesis of oligomeric poly[(1, 2-propanediamine)-alt-(oxalic acid)] and anomalous proton conductivities of the thin films. Solid State Ionics 180, 589–591 (2009).
72. Nagao, Y., Naito, N., Iguchi, F., Sata, N. & Yugami, H. Proton Conductivity of Oligomeric Poly[(1,2-Propanediamine)-alt-(Oxalic Acid) Thin Films on Al2O3 Substrates. e-Journal Surf. Sci. Nanotechnol. 7, 530–532 (2009).
73. Nagao, Y. Substrate Dependence of the Proton Transport and Oriented Structure in Oligo[(1,2-propanediamine)-alt-(oxalic acid)] Thin Films. https://doi.org/10.1246/cl.130019 42, 468–470 (2013).
74. Park, M. J. & Balsara, N. P. Anisotropie proton conduction in aligned block copolymer electrolyte membranes at equilibrium with humid air. Macromolecules 43, 292–298 (2010).
75. Tonozuka, I., Yoshida, M., Kaneko, K., Takeoka, Y. & Rikukawa, M. Considerations of polymerization method and molecular weight for proton-conducting poly(p-phenylene) derivatives. Polymer (Guildf). 52, 6020–6028 (2011).
76. Sato, T. et al. High proton conductivity in the molecular interlayer of a polymer nanosheet multilayer film. Langmuir 31, 5174–5180 (2015).
77. Horike, S., Umeyama, D. & Kitagawa, S. Ion conductivity and transport by porous coordination polymers and metal-organic frameworks. Acc. Chem. Res. 46, 2376–2384 (2013).
78. Zhai, L. et al. Accumulation of Sulfonic Acid Groups Anchored in Covalent Organic Frameworks as an Intrinsic Proton-Conducting Electrolyte. Macromol. Rapid Commun. 43, 1–7 (2022).
79. Miyatake, K., Zhou, H., Uchida, H. & Watanabe, M. Highly proton conductive polyimide electrolytes containing fluorenyl groups. Chem. Commun. 3, 368–369 (2003).
80. Miyatake, K., Zhou, H., Matsuo, T., Uchida, H. & Watanabe, M. Proton conductive polyimide electrolytes containing trifluoromethyl groups: Synthesis, properties, and DMFC performance. Macromolecules 37, 4961–4966 (2004).

81. Wakita, J., Jin, S., Shin, T. J., Ree, M. & Ando, S. Analysis of molecular aggregation structures of fully aromatic and semialiphatic polyimide films with synchrotron grazing incidence wide-angle x-ray scattering. Macromolecules 43, 1930–1941 (2010).
82. Yin, Y. et al. Water stability of sulfonated polyimide membranes. Macromolecules 39, 1189–1198 (2006).
83. Yin, Y. et al. Synthesis and properties of highly sulfonated proton conducting polyimides from bis(3-sulfopropoxy)benzidine diamines. J. Mater. Chem. 1062–1070 (2004) doi:10.1039/B313276E.
84. Yin, Y., Tanaka, K., Kita, H. & Okamoto, K.-I. Sulfonated Polyimide Membranes for Polymer Electrolyte Fuel Cell.
85. Krishnan, K., Iwatsuki, H., Hara, M., Nagano, S. & Nagao, Y. Proton conductivity enhancement in oriented, sulfonated polyimide thin films. J. Mater. Chem. A 2, 6895–6903 (2014).
86. Wegner, G. Ultrathin films of polymers: architecture, characterization and properties. Thin Solid Films 216, 105–116 (1992).
87. Krishnan, K., Iwatsuki, H., Hara, M., Nagano, S. & Nagao, Y. Influence of Molecular Weight on Molecular Ordering and Proton Transport in Organized Sulfonated Polyimide Thin Films. J. Phys. Chem. C 119, 21767–21774 (2015).
88. Takakura, K. et al. Lyotropic ordering for high proton conductivity in sulfonated semialiphatic polyimide thin films. Polym. J. 51, 31–39 (2019).
89. Ono, Y. et al. High Proton Conduction of Organized Sulfonated Polyimide Thin Films with Planar and Bent Backbones. Macromolecules 51, 3351–3359 (2018).
90. Liu, Y., Pharr, M. & Salvatore, G. A. Lab-on-Skin: A Review of Flexible and Stretchable Electronics for Wearable Health Monitoring. ACS Nano 11, 9614–9635 (2017).
91. Gong, S. et al. A wearable and highly sensitive pressure sensor with ultrathin gold nanowires. Nat. Commun. 5, 1–8 (2014).
92. Pan, L. et al. An ultra-sensitive resistive pressure sensor based on hollow-sphere microstructure induced elasticity in conducting polymer film. Nat. Commun. 5, 1–8 (2014).
93. Zang, Y., Zhang, F., Di, C. A. & Zhu, D. Advances of flexible pressure sensors toward artificial intelligence and health care applications. Mater. Horizons 2, 140–156 (2015).
94. Wang, X. et al. Recent Progress in Electronic Skin. Adv. Sci. 2, 1–21 (2015).
95. Timsit, R. S. Electrical contact resistance: Properties of stationary interfaces. IEEE Trans. Components Packag. Technol. 22, 85–98 (1999).
96. Frutiger, A. et al. Capacitive soft strain sensors via multicore-shell fiber printing. Adv. Mater. 27, 2440–2446 (2015).
97. Park, K. Il et al. Highly-efficient, flexible piezoelectric PZT thin film nanogenerator on plastic substrates. Adv. Mater. 26, 2514–2520 (2014).
98. Xu, S. et al. Self-powered nanowire devices. Nat. Nanotechnol. 5, 366–373 (2010).
99. Lin, L. et al. Triboelectric active sensor array for self-powered static and dynamic pressure detection and tactile imaging. ACS Nano 7, 8266–8274 (2013).
100. Wang, C., Xia, K., Zhang, M., Jian, M. & Zhang, Y. An All-Silk-Derived Dual-Mode E-skin for Simultaneous Temperature-Pressure Detection. ACS Appl. Mater. Interfaces 9, 39484–39492 (2017).
101. Trung, T. Q., Ramasundaram, S., Hwang, B. U. & Lee, N. E. An All-Elastomeric Transparent and Stretchable Temperature Sensor for Body-Attachable Wearable Electronics. Adv. Mater. 28, 502–509 (2016).

Chapter 2

Effect of cross-linking on sulfonated polyimide thin film for high proton conductivity

Abstract

Sulfonated semi-alicyclic polyimides suffer the challenge of not maintaining mechanical and chemical stability in water. Herein, we synthesized a new sulfonated semi-alicyclic polyimide composed of Bicyclo[2.2.2]oct-7-ene-2,3,5,6-tetracarboxylic Dianhydride (BOEDA) and 3,3'-bis-(sulfopropoxy)-4,4'-diaminobiphenyl (BSPA) which containing dienophile structure can undergo Diels–Alder (D-A) reaction. A facile cross-linking reaction was carried out via Fe^{3+}-catalyzed D-A reaction between BSPA-BOEDA and silica nanoparticles modified by (3-cyclopentadienylpropyl) triethoxyslane (CPTS). Compared with BSPA-BOEDA, the cross-linked BSPA-BPEDA-NPs membrane and thin film showed better stability in water. Humidity-controlled grazing Incidence X-ray scattering (GIXRS) revealed that a phase separation was formed in both BSPA-BOEDA and BSPA-BPEDA-NPs thin films. The BSPA-BOEDA and BSPA-BPEDA-NPs thin films exhibited a high conductivity of 4×10^{-2} S cm^{-1} and 1×10^{-2} S cm^{-1}under 25 ℃ and 95% relative humidity (RH), respectively.

2.1 Introduction

Based on the descriptions in the previous chapters, it can be known that the reason why fully aromatic and semi-alicyclic ASPIs can exhibit high proton conductivity comparable to that of Nafion is that fully aromatic and semi-alicyclic ASPIs can form well-defined lamellar-organized structures under humidified conditions.[1,2,3,4,5,6] However, in the actual PEMFC operating environment, the ionomer thin film is always under high humidity conditions, even immersed in water, especially at the cathode where a large number of water molecules are generated, which requires the mechanical and chemical stability of the ionomer thin film in water.

Nafion with a perfluoropolyethylene structure as the backbone exhibits excellent mechanical and chemical stability due to its super-strong hydrophobic backbone. However, the complex production process and high cost also limit its large-scale application.[7,8] In contrast, ASPIs are simpler to produce, lower cost and more environmentally friendly due to no fluorine. However, since the hydrophobicity of the backbone is greatly reduced compared to that of Nafion, its stability in water is noteworthy, especially for semi-alicyclic ASPIs.

The sulfonic acid groups on the side chains of ASPIs can easily adsorb water molecules through hydrogen bond interaction under high humidity conditions. This will result in excessive swelling or even dissolution, which will lead to a decrease in mechanical properties. ASPIs also exhibit high ion exchange capacity (IEC) values. In PEMFCs system, higher IEC value also affords the fragile and unfavorable film. To solve these problems, two kinds of strategies can be chosen. One is introducing hydrophobic segments into the backbone; another one is making cross-linking structures. For the first strategy, since some parts which cannot be used as a proton transport carrier are introduced, the reduction of ion exchange capacity may lead to a decrease in proton conductivity.[9,10] Generally, cross-linking can inhibit the plasticization of polymers and enhance their chemical and mechanical stability.[11,12,13]

There are several methods for cross-linking SPIs, such as thermal cross-linking, ultraviolet (UV) cross-linking and chemical cross-linking. But both the thermal cross-linking method and UV crosslinking method suffer from some inevitable flaws. For example, the reaction speed of UV cross-linking is slow, and the reaction mostly occurs on the surface, therefore the reaction inside the thin film is difficult.[14] The thermal crosslinking is only suitable for SPIs containing alkynyl groups.[15,16] In contrast, chemical cross-linking methods are more widely used in studies related to SPI cross-linking. By introducing functional

groups that can be used for cross-linking in the main or side chains of SPI and selecting appropriate cross-linking agents, the effect of cross-linking on the properties of SPI can be systematically explored.

There have been some reports of cross-linked SPI through the chemical cross-linking method. Okamoto et al. obtained membranes with significantly improved oxidative stability by covalently crosslinking SPIs containing benzimidazole groups in polyphosphoric acid.[17] Guan et al. obtained SPI membranes with improved solvent resistance, oxidative stability and mechanical stability by introducing pendant tetrafluorostyrol groups in the side chains and thermally cross-linking at 260 °C.[18] Han et al. investigated the effect of cross-linking on SPI membrane based on the reaction between acridine groups and dibromoalkanes with different lengths in detail. It was found that the hydrolytic stability of the SPI membranes decreased as the length of the alkyl group of the cross-linking agent increased but the hydrolytic stability of all cross-linked SPI films was better than that of the uncross-linked SPI membranes.[19] Kim et al. reported cross-linked SPI membranes based on carboxylic acids and diols and investigated the effect of alkyl chain length of diols as cross-linking agents on membrane properties.[20] Yang et al. reported cross-linked SPI membranes based on maleic anhydride-terminated sulfonated polyimides with the hydrophilic cross-linking agent poly(ethylene glycol) diacrylate.[21] Wang et al. reported a kind of cross-linked membrane based on highly branched SPI.[22] Generally, these crosslinked membranes exhibit reduced water uptake and proton conductivity compared to uncross-linked membranes. This is also caused by the introduction of components in the SPI that cannot act as proton-conducting carriers.

The Diels–Alder (D-A) reaction, with its rich synthetic diversity, is recognized as one of the cornerstone reactions in modern organic chemistry. The D-A reaction is a [4 + 2] cycloaddition reaction that occurs between electron-rich dienes and electron-depleting dienophiles.[23] The D-A reaction is also commonly used in cross-linking methods due to its advantages such as mild reaction conditions, no by-products, reaction in water, etc.[24] The D-A reaction can occur at room temperature, but the reaction rate may be slow. Fortunately, many Lewis acids can effectively accelerate the D-A reaction.[25,26,27,28] If the designed SPI contains dienophiles that can undergo a D-A reaction, then cross-linking could be performed by D-A reaction. In this way, the introduction of non-ionically conductive components into the SPI. can be avoided.

The objective of this chapter is to develop a new design for cross-linked ASPI by D-A reaction to improve its stability in solvents and mechanical properties without reducing the proton conductivity.

Simultaneously, explore the effect of cross-linking on the water uptake by in situ quartz crystal microbalance (QCM) and ordered structure by RH-controlled grazing-incidence small-angle X-ray scattering (GI-SAXS) of ionomer thin films. The results reveal that the cross-linking structure increased the stability of ionomer thin film in water and does not decrease the water uptake and proton conductivity significantly. The cross-linked thin film still exhibits comparable proton conductivity to the reported materials.

2.2 Experimental section

2.2.1. Materials

3,3'-Bis(sulfopropoxy)-4,4'-diaminobiphenyl (BSPA) was synthesized according to previous reports.[3,29] Triethylamine (TEA) was used as received from Kanto Chemical Co. Inc., Japan. Hydrochloric acid, m-cresol, acetic acid, acetic anhydride, methanol, and acetone were obtained from Fujifilm Wako Pure Chemical Corp., Japan. 1,2,3,4-Cyclopentanetetracarboxylic dianhydride was purchased from Tokyo Chemical Industry Co. Ltd., Japan.

2.2.2 Synthetic route of 3,3'-bis(sulfopropoxy)-4,4'-diaminobiphenyl (BSPA)

The synthetic route of 3,3'-bis(sulfopropoxy)-4,4'-diaminobiphenyl (BSPA) is shown in Scheme 2-1. The detailed steps are described as follows

Step 1: Protection of amine groups

3,3'-dihydroxybenzidine (Tokyo Chemical Industry Co., Ltd.) 5 g, Acetic anhydride (Fujifilm Wako Pure Chemical Corporation) 79 ml, acetic acid (Wako) 1.5 ml, water (18 MΩ cm^{-1}) 200 ml were added into the Erlenmeyer flask and stirring at 70–80 °C for 2 h. After cooling to room temperature, the mixture was further cooled down by the ice bath. The solid product was separated from the mixture by centrifuge 5804 (Eppendorf) and washed several times with acetone. The calculated yield was 97% after the product had dried overnight in a vacuum.

Step 2: Introduction of sulfonated side chains

The acetylated 3,3'-dihydroxybenzidine, 1,3-Propanesulton (Tokyo Chemical Industry Co., Ltd.) and sodium hydroxide (Fujifilm Wako Pure Chemical Corporation) was added into a three-necked flask

equipped with a molar ratio of 1: 3: 3, respectively. 150 ml methanol was added into the flask to dissolve all the chemicals. Under the protection of argon atmosphere, the reaction was refluxed at 80 °C for 6 hours. The solution was black at the beginning of the reaction and turned yellowish-brown after about 1.5 h. After sufficient cooling in ice bath, the solid product was separated from the mixture by centrifuging, and the product was washed several times with methanol and acetone. The dried product was weighed after being vacuum dried overnight, and the yield was 50.3%. Based on NMR results, the sulfonation rate was calculated as 95%.

Step 3: Ion exchange

The solid product obtained in the previous step was dissolved in water (18 MΩ cm^{-1}). The aqueous solution flowed through a glass column filled with ion exchange resin Amberlyst 31WET (Organo) slowly. This process was repeated 5 times to exchange sodium ions into hydrogen ions as much as possible. Then the water was removed by rotary evaporator (Yamato Science).

Step 4: Removal of protective groups

The ion-exchanged product was dissolved in 100 ml of hydrochloric acid (Fujifilm Wako Pure Chemical Corporation). In a three-necked flask with a magnetic stirrer, the solution was refluxed at 120 °C for 2 hours under the protection of argon atmosphere. After that, the condenser tube was removed, and the temperature was raised to 150 °C for dry distillation. The evaporated hydrochloric acid was absorbed with a sodium hydroxide solution prepared in advance. The obtained product was washed with 2-propanol and acetone and then sufficiently dried to obtain a final product BSPA. The final yield was 47%

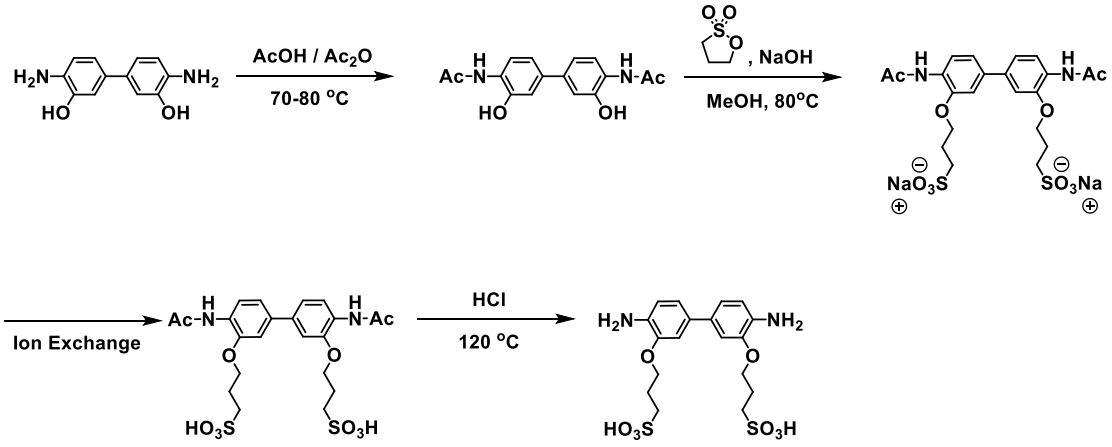

Scheme 2-1. Scheme for synthesizing BSPA

2.2.3 Synthetic route of BSPA-BOEDA

The synthetic route of BSPA-BOEDA is shown in Scheme 2-2. BSPA 0.46 g (1 mmol) and BOEDA 0.25 g (1 mmol) were added into a three-necked flask with magnetic stirring. 10 ml m-cresol (Fujifilm Wako Pure Chemical Corporation) was added to the three-necked flask as a solvent. Then filled with 600 µl triethylamine (Kanto Chemical Co. Inc) . Under the protection of argon atmosphere, the reaction was first performed at 80 ℃ for 2 h. Then, the temperature was raised to 180 ℃ and the reaction was continued for 20 h. After the reaction, the resulting solution was cooled to room temperature, and further cooled in ice bath for 30 minutes. The cooled solution was added to 100 ml of cold fresh acetone to obtain a white flocculent precipitate. The solid product was obtained by centrifugation and washed several times with acetone, then dried under vacuum overnight. The dried product was then dissolved in water, and ion exchange was carried out using a glass column packed with ion exchange resin Amberlyst 31WET (Organo). This process was repeated several times to ensure that sulfonate was exchanged to sulfonic acid as much as possible. The solvent was removed by rotary evaporation and the final product BSPA-BOEDA was obtained after completely drying.

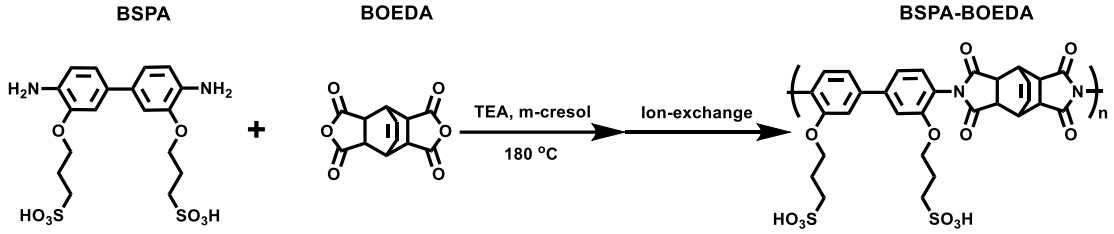

Scheme 2-2. Scheme for synthesizing BSPA-BOEDA.

2.2.4 Characterization

2.2.4.1 Nuclear magnetic resonance (NMR)

The ^{1}H nuclear magnetic resonance (NMR, Bruker Avance III (400 MHz) spectrometer; Bruker Analytik GmbH) spectra was used to determine whether the monomer and polymer were successfully synthesized. Approximately 3 mg of monomer or oligomer was dissolved in a 600 µl dimethyl sulfoxide (DMSO) solution containing 0.03% of trimethylsilane (TMS) for NMR determination. After the measurement, software 1D NMR was used to integrate the results.

2.2.4.2 Infrared (IR) spectroscopy

The Fourier Transform Infrared Spectroscopy of monomer and oligomer was measured by

Attenuated Total Reflection (FT-IR ATR). The used device was Nicolet 6700 (Thermo Fisher Scientific Inc.) and the analysis software used was OMNIC (Thermo Fisher Scientific Inc.). The sample powder is evenly coated on the prism and compacted with equipment to make the sample fully contact the prism, following the sample was measured. The background spectrum and the sample spectrum were scanned 64 times to obtain the correct spectral image. The obtained spectrum was corrected by using Advanced ATR Correction. The measurement range was 400-4000 cm^{-1}.

2.2.4.3 Gel permeation chromatography (GPC)

The molecular weight of BSPA-BOEDA was measured by gel permeation chromatography (GPC), and the equipment used was LC-2000plus (JASCO). The mobile phase solution was obtained by mixing 10.26 g of $NaNO_3$ (Kanto Chemical Co. Inc), 600 ml of water, 400 ml of N, N'-dimethylformamide (DMF) (Fujifilm Wako Pure Chemical Corporation) and 18 mL of acetic acid. The preparation method of the measurement solution containing BSPA-CPDA is described as follows:

0.03 wt% of BSPA-BOEDA was added to 3ml of the mobile phase solution and stir it thoroughly to dissolve it. The solution containing BSPA-BOEDA was filtered by a syringe with a filter, then transfer the filtered solution to a screw cap bottle with a silicone cap. 50 µl of the prepared solution was injected into the device by microsampler. The molecular weight of the sample was calculated by comparing it with a standard curve drawn with standard materials in advance. The method of making the standard curve is as follows. Several polystyrenes with exact molecular weight (Mw = 759,000, 580,000, 290,000, 101,000, 23,600) were dissolved in mobile solution to prepare a standard solution. GPC measurement was performed on the standard solution, and the obtained results were fitted into a standard curve.

2.2.4.4 Scanning electron microscope and energy dispersive X-ray spectroscopy (SEM-EDX)

Scanning electron microscopy and Energy dispersive X-ray spectroscopy (SEM-EDX) were carried out using a TM3030Plus miniscope (Hitachi). The accelerating voltage was 15 kV.

2.2.5 Membrane preparation

The silica nanoparticles modified by (3-cyclopentadienylpropyl) triethoxyslane (CPTS) was received from Nagoya university. Cyclopenta-1,3-diene and its substitutes are commonly used dienes in Diels–Alder (D-A) reaction. 90 mg of BSPA-BOEDA and 10 mg of nanoparticles (NPs) were dissolved in 2 ml

mixed solution of water and THF (1:1 w/w). When the polymer and NPs were completely dissolved, add ferric chloride ($FeCl_3 \cdot 6H_2O$) and continue stirring until completely dissolved. Then, the solution was transferred into a mold and heated at 50 °C to dry until the solvent was completely evaporated. The synthetic route is shown in Scheme 2-3.

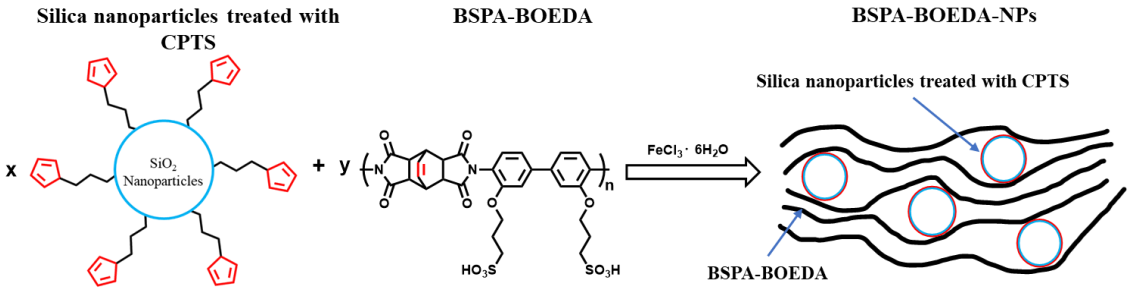

Scheme 2-3. Preparation scheme of cross-link BSPA-BOEDA-NPs.

2.2.6 Thin film preparation

2.2.6.1 Preparation of BSPA-BOEDA thin film

The spin coating (ACT-200 spin-coater; Active Co. Ltd.) method was used to prepare thin films. BSPA-BOEDA was dissolved in the 1: 1 (w / w) of water and Tetrahydrofuran (THF) (Fujifilm Wako Pure Chemical Corporation). The thickness of thin films was controlled at about 500 nm. The Si, SiO_2 substrates (E&M Co. Ltd.) and SiO_2-coated 9 MHz quartz crystals (Seiko EG&G Co. Ltd.) were washed with 2-propanol in advance. Before thin film deposition, plasma treatment (Cute-MP; Femto Science, Korea) was carried out to improve the hydrophilic properties of the substrate surface.

2.2.6.2 Preparation of BSPA-BOEDA-NPs thin film

To obtain thin films with good surface roughness, the NPs was first dissolved in 300 μl mixed solution of water and THF (3:4 w/w) and flowed through a filter film with a pore size of 1 μm to remove large aggregates. 9 mg of BSPA-BOEDA was added into the filtered solution and sonicated until completely dissolved. Then the solution was cooled in an ice-water bath for 30 min before the addition of $FeCl_3 \cdot 6H_2O$ (1 mg). The spin coating method was used to prepare thin film and the thickness was controlled at about 500 nm. The prepared thin films were immersed into 100 ml 1 M hydrochloric acid (HCl) to remove Fe^{3+} and then vacuum dried at 60 °C overnight.

2.2.7 Water uptake

The water uptake was measured with the humidity-controlled in situ quartz crystal microbalance (in-situ QCM) system. The diagram of the QCM substrate used in the measurement is shown in Figure 2-1. The schematic diagram of the measuring device is shown in Figure 2-2. Various relative humidity (RH) was generated by humidity generator Bel Flow (MicrotracBEL Corp.) by mixing dry N_2 gas and steam. The QCM substrate was placed in a homemade humidity control chamber equipped with a high-resolution RH sensor and was connected to the oscillation circuit and the frequency counter 5313A (Agilent Technologies) through a circuit. The weight change of the film can be calculated by using the Sauerbrey equation.

$$\Delta m = \frac{S\times\sqrt{\rho\mu}}{2\times F^2} \times (-\Delta F) \quad (2\text{-}1)$$

where S is the electrode surface area. ρ, and μ stand for the quartz density and quartz shear modulus, respectively. F is for the fundamental frequency of QCM substrate. The number of water molecules adsorbed per sulfonic acid group (water uptake / λ) was calculated by the following formula as shown below,

$$\lambda = (\frac{m}{m_0} - 1) \times \frac{EW}{M_{H_2O}} \quad (2\text{-}2)$$

where *m* represents the mass of the film under each humidity, m_0 represents the mass of the film at the dry condition, M (H_2O) is the molecular weight of water molecules, and *EW* expresses the equivalent weight of each sulfonic acid group

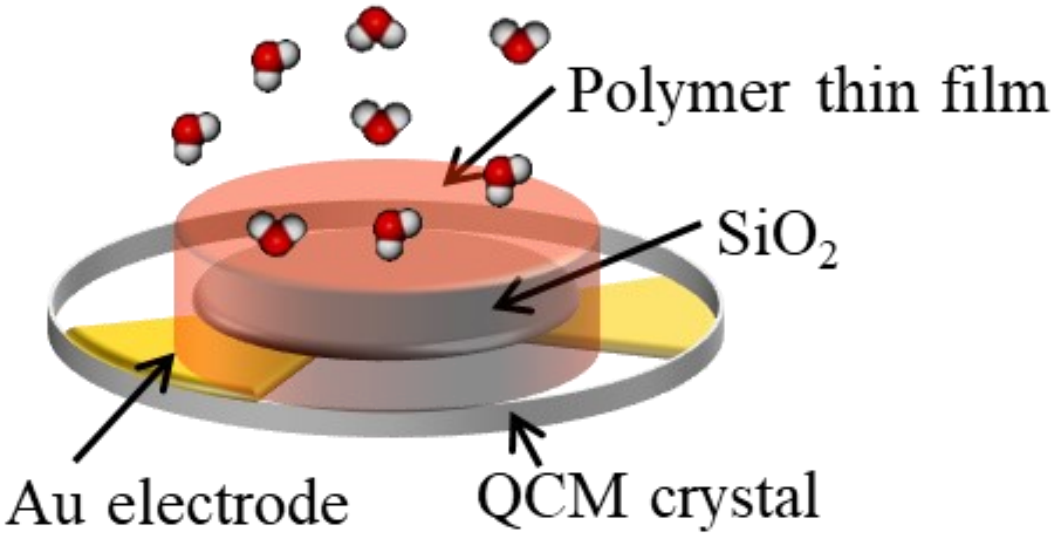

Figure 2-1. Schematic illustration of the quartz crystal microbalance devices.

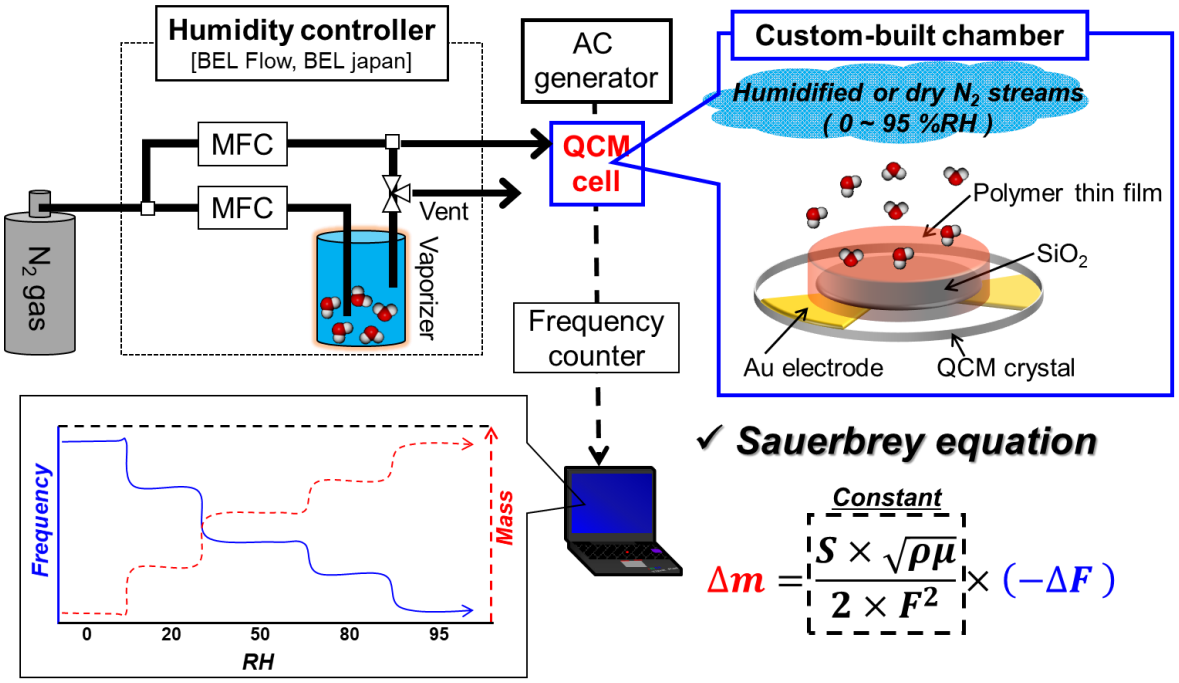

Figure 2-2. Schematic illustration of in-situ QCM measurement.

2.2.8 In situ FTIR

The dissociation state of the sulfonic acid group was investigated by RH controlled in situ FTIR measurements. The schematic diagram of the measuring system is shown in Figure 2-3. The thin film sample made on silicon wafers was placed in homemade chambers. In the humidity-controlled cell, CaF_2 windows were employed. An FTIR spectrometer (Nicolet 6700; Thermo Fisher Scientific Inc.) equipped with a deuterium triglycine sulfate (DTGS) detector was used for transmission in situ FTIR measurements. The RH change was controlled within the range of 0-95% through a humidity generator (me-40DP-2PW; Microequipment). When only nitrogen gas was flowing, the RH was defined as 0%.

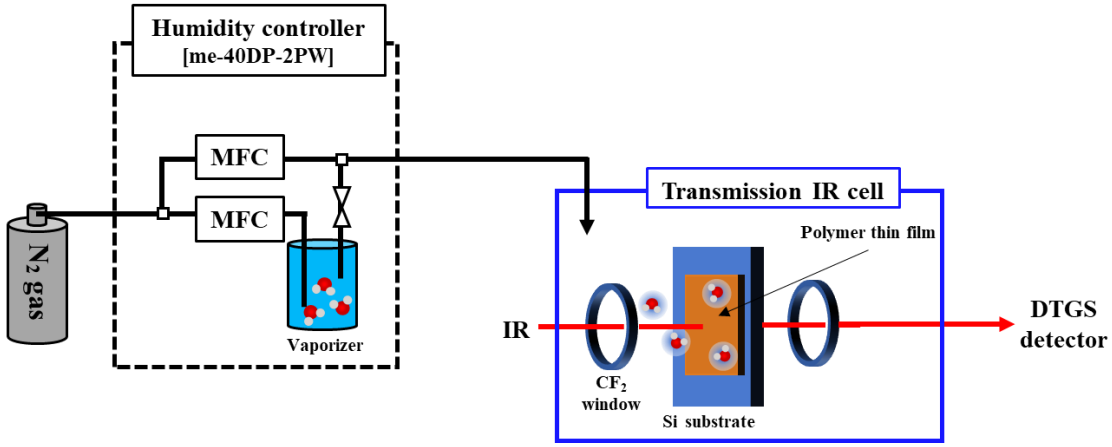

Figure 2-3. Schematic illustration of in-situ FT-IR measurement under humidity control.

2.2.9 Grazing incidence X-ray scattering (GIXRS)

RH in situ GIXRS was measured by an FR-E X-ray diffractometer equipped with R-AXIS IV two-dimensional (2D) detector (FR-E; Rigaku Corp.). The schematic diagram of the measuring system is shown in Figure 2-4. The thin film sample was placed in a humidity-controlled cell with X-ray transparent polyester film (Lumirror) windows. The humidity in the cell was controlled using the humidity generator me-40DP series. X-rays with a wavelength of 0.1542 nm were generated through Cu Kα radiation and have a beam size of approximately ϕ300 μm. The camera length was 300 mm, and the incidence angle was set in the range of 0.20°-0.22°.

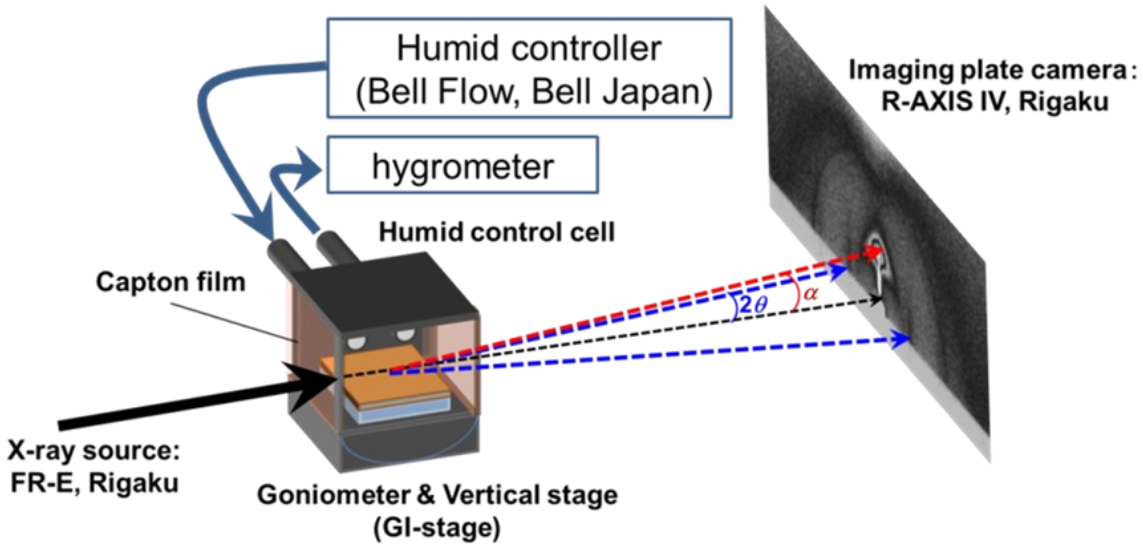

Figure 2-4. Schematic illustration of in-situ GISAXS measurement.

2.2.10 Molecular structure simulation

The optimized molecular structures were calculated by Material Studio 2020. The calculations were

done based on DFT using a DMol3 module. The generalized gradient approximation (GGA) functional with the Perdew-Burke-Ernzerhof (PBE) type was used to model the exchange and correlation interactions. Convergence threshold for the maximum force and maximum displacement for normal geometry optimization were set, respectively, to 0.002 Ha Å-1 and 0.005 Å.

2.2.11 Proton conductivity

The proton conductivity of the BSPA-BOEDA and BSPA-BOEDA-NPs thin films in the direction parallel to a substrate surface was measured by alternating current (AC) electrochemical impedance spectroscopy (EIS). The schematic diagram of the measuring system is shown in Figure 2-5. The frequency response analyzer and high-frequency dielectric interface (SI1260 and SI1296; Solartron Analytical) were used to measure the impedance. A humidity- and temperature-controlled chamber (SH-221; Espec Corp.) was used to control the humidity and temperature during the experiment. The impedance was measured when an AC voltage of 50 mV was applied, and the frequency was scanned in the range of 1 Hz to 10 MHz. The RH was controlled between 40% and 95%, and the temperature was stable at 298 K. The collected impedance values (R) were converted to the conductivity of thin film directly by the following equation,

$$\sigma = \frac{d}{Rlt} \tag{2-3}$$

where *t* and *l* stand for the film thickness and contact electrode length, respectively. *d* represents the distance between the two gold electrodes.

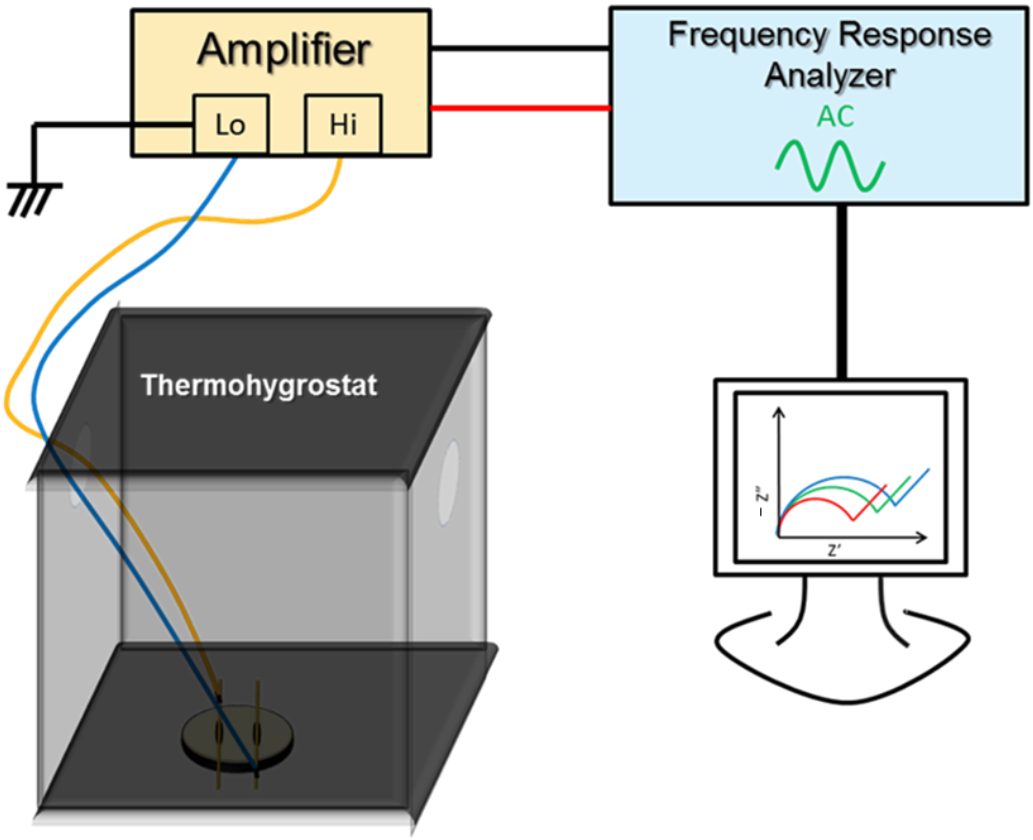

Figure 2-5. Schematic illustration of AC impedance method.

2.3 Results and discussions

2.3.1 Characterizations

2.3.1.1 ^{1}H nuclear magnetic resonance (^{1}H NMR)

The structure and ^{1}H NMR results of the BSPA-BOEDA are shown in Figure 2-6. The peaks from the possible by-product amide or carboxyl group were not observed, which proved that the imidization reaction was complete. Integration of proton peaks in ^{1}H NMR spectra was in good agreement with the number of protons in both the backbone and side chain of BSPA-BOEDA structure. Before ion exchange, the prepared polymer exhibits the TEA trace (red arrow), which is also dominant in the spectrum. After ion exchange, the TEA amount reduced considerably, which is less than 1% compared to before ion exchange.

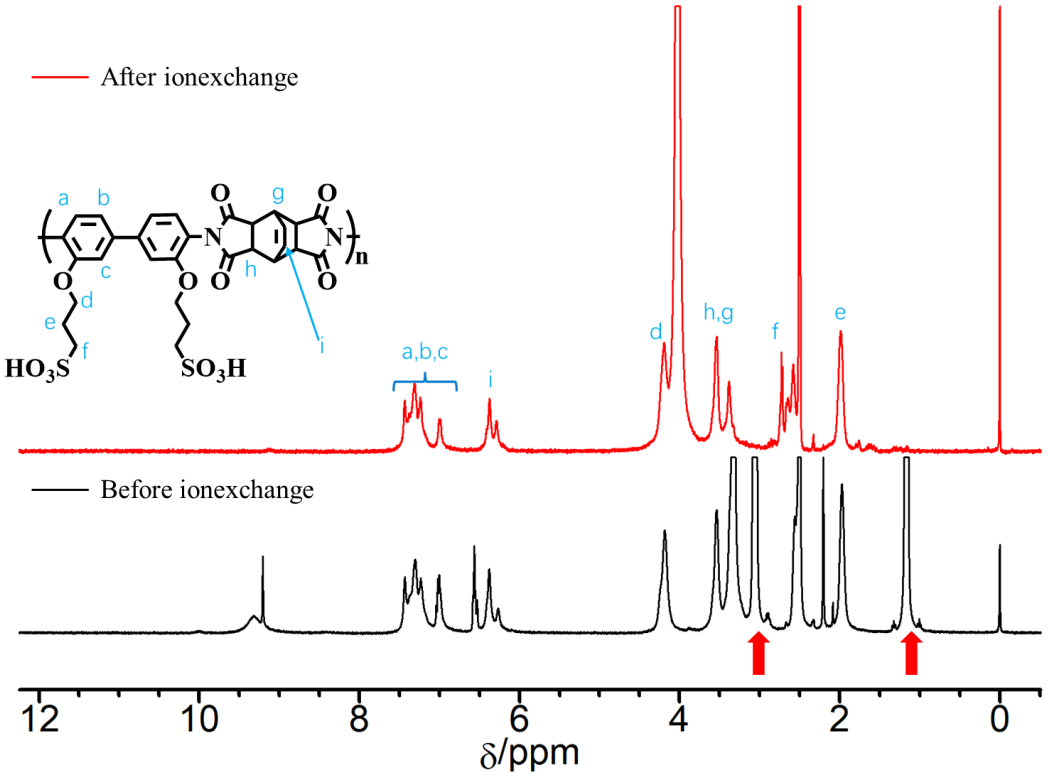

Figure 2-6. ^{1}H NMR (DMSO-d_6) spectra for each BSPA-BOEDA.

2.3.1.2 FT-IR ATR study

FTIR-ATR spectra of BSPA and BSPA-BOEDA are shown in Figure 2-8. The absorption peaks of ν_{sym} (C=O) 、ν_{asym} (C=O) and ν (C-N) which stand for imide were observed at 1776 cm^{-1},1710 cm^{-1} and 1382 cm^{-1}, respectively.[30,31,32,33] Since δ (N-H) observed at 1629 cm^{-1} of BSPA was not observed in BSPA-BOEDA, indicating that the imidization reaction was completed. In addition, since δ (C-N-H) (1530 cm^{-1}) of amic acid, which is an intermediate of imidization reaction, was not observed, it also indicated that imidization reaction was completed52. Absorption peaks at 1502 cm^{-1} and 1573 cm^{-1} caused by vibration of the phenylenediamine benzene ring skeleton ν(C-C) were observed.[34,35] Asymmetric stretching vibration peaks and symmetric stretching vibration peaks of the sulfonic acid group were observed at 1230 cm^{-1} and 1189 cm^{-1}, respectively.[36] Asymmetric stretching vibration peaks of sulfonic acid groups after proton ionization were observed at 1031 cm^{-1}.[37]

As a result of the FT-IR ATR measurement, it was found that imidization proceeded sufficiently since the typical peak of amide, amide δ (N-H) and amic acid δ (C-N-H) were not observed. Also, no by-product

or unreacted product peaks were observed.

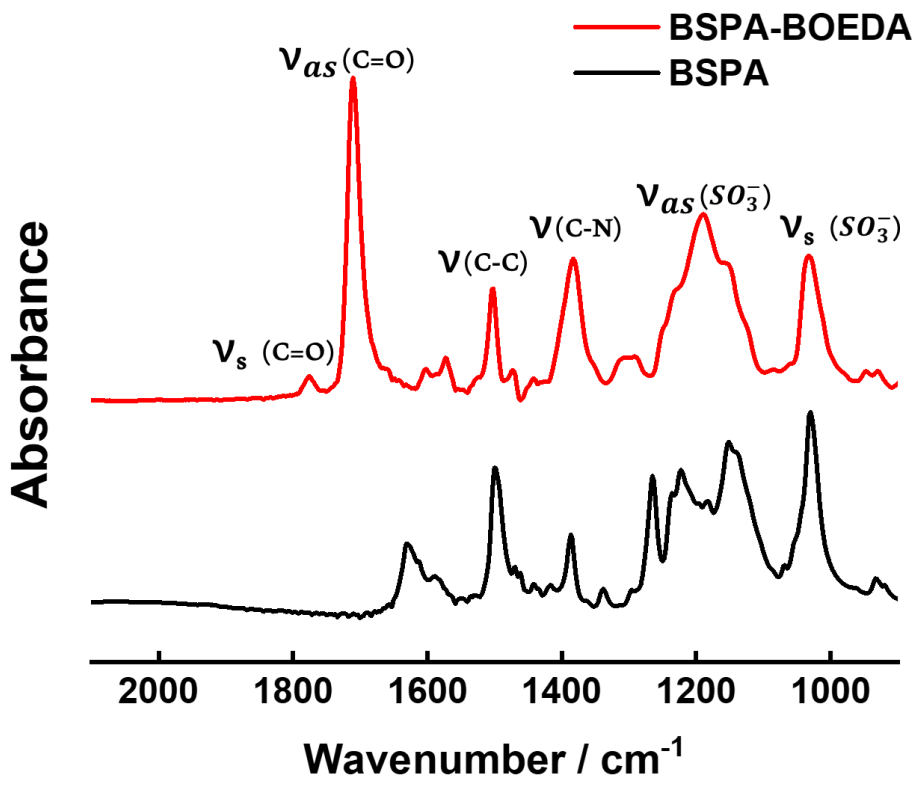

Figure 2-7. FTIR ATR spectra for 3,3'-BSPA and BSPA-BOEDA.

2.3.1.3 GPC study

The molecular weight of the polymer was confirmed by GPC and Figure 2-8 shows the GPC chromatogram. The calculation results of molecular weight were shown in Table 3-1. As a result of calculation using a calibration curve, the weight average molecular weight (Mw) of BSPA-BOEDA was 75000. Since no other prominent peaks were observed, the polymer was considered to have sufficiently polymerized.

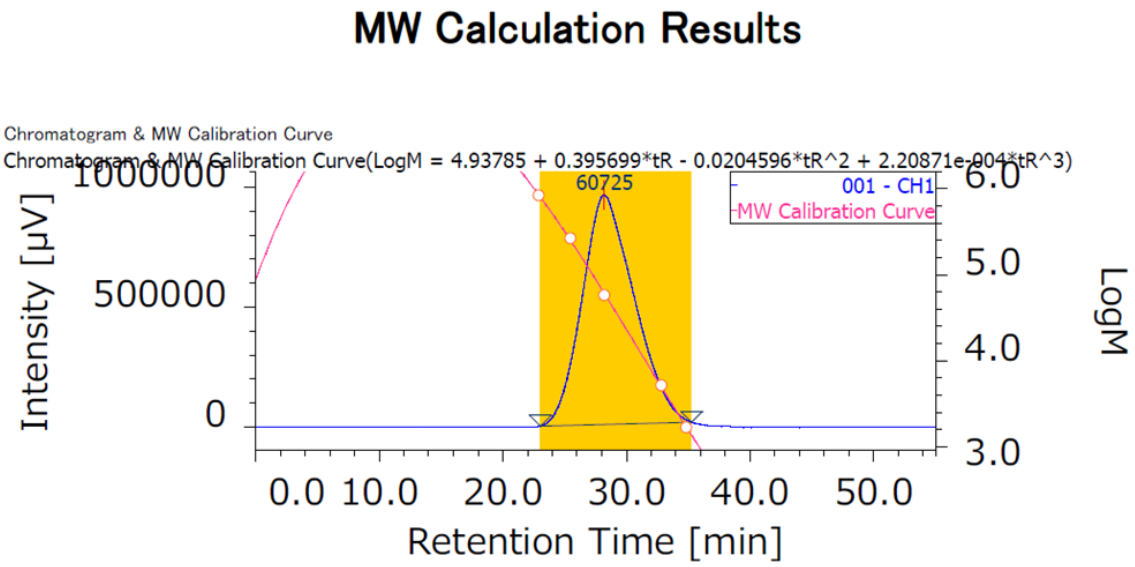

Figure 2-8.GPC spectra for BSPA-BOEDA.

Table 2-1. Molecular weight of BSPA-BOEDA.

	Baseline range	M_w	M_n	M_w/ M_n
BSPA-BOEDA	23.03 - 35.25	74747	24669	3.03

2.3.2 Fabrication of cross-linked BSPA-BOEDA-NPs membrane and thin film

2.3.2.1 Membrane fabrication

To demonstrate that the D-A reaction can take place between BSPA-BOEDA and CPTS modified NPs, an attempt was first made to fabricate membranes of BSPA-BOEDA and BSPA-BOEDA-NPs. The solubilities of the resulting membranes were compared by immersing them in deionized water and the result was shown in Figure 2-9. The BSPA-BOEDA membrane dissolved quickly in water even without stirring. However, the cross-linked BSPA-BOEDA-NPs membrane was hard to dissolve in water. The obvious change in solubility proves the success of the D-A reaction.

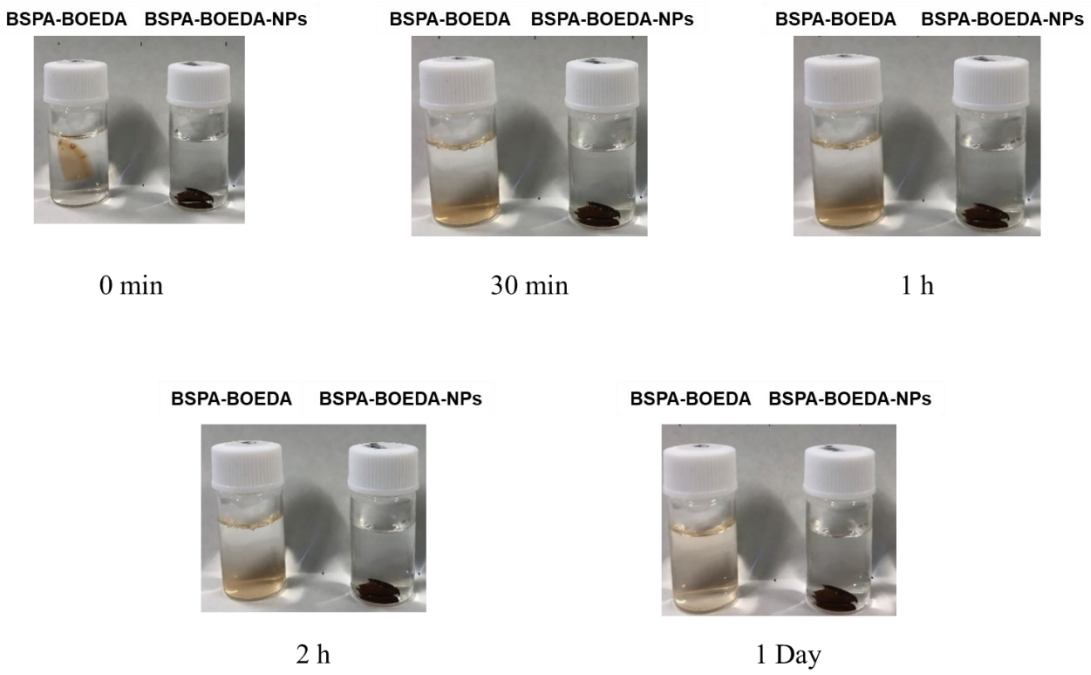

Figure 2-9. Solubility of BSPA-BOEDA membrane and BSPA-BOEDA-NPs membrane.

2.3.2.2 Thin film fabrication

The BSPA-BOEDA-NPs thin films with a thickness of ~500 nm were fabricated by spin coating method. The D-A reaction catalyzed by $FeCl_3$ can occur rapidly even at room temperature.[27,28,38] Therefore, to obtain thin films with good surface roughness, the solution was cooled in an ice-water bath for 30 min before adding $FeCl_3 \cdot 6H_2O$. Since Fe^{3+} ions can affect the measurement of proton conductivity, it must be removed completely by washing the thin film with 1 M HCl (aq). To confirm Fe^{3+} was completely removed, SEM-EDX was used, and the result is shown in Figure 2-10. Before washing by HCl the Fe^{3+} existed in thin film, while after washing Fe^{3+} was completely removed. Moreover, the BSPA-BOEDA-NPs thin films even cannot dissolve in 1 M HCl (aq) also proving that the D-A reaction occurred between BSPA-BOEDA and NPs.

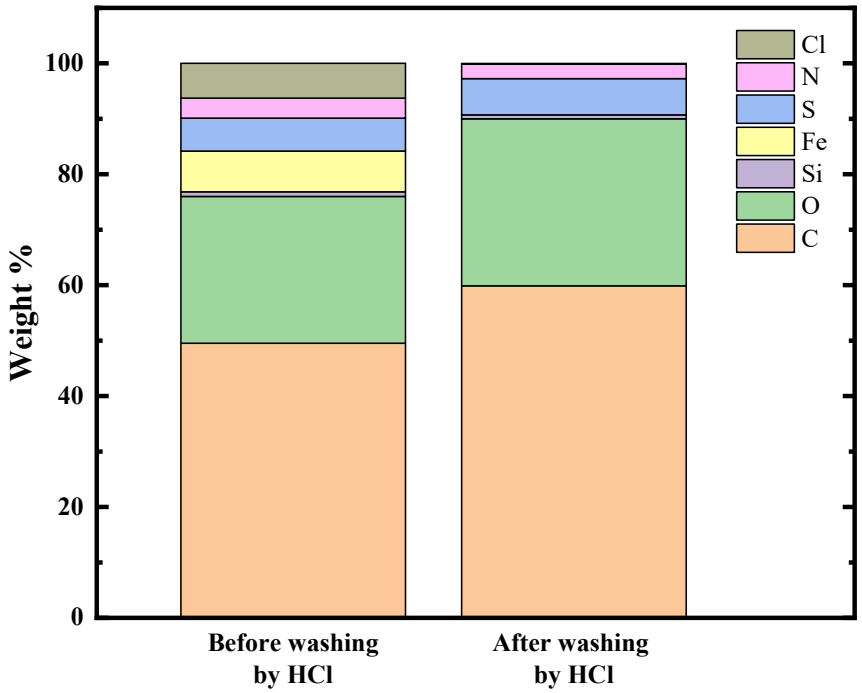

Figure 2-10. EDX results of BSPA-BOEDA-NPs thin film before and after washing by 1 M HCl.

2.3.3 Water uptake

Because water works as a carrier to facilitate the transport of protons in thin films, water uptake has a significant impact on the conductivity of proton exchange membranes. Figure 2-11 shows the RH-dependent water uptake of BSPA-BOEDA and BSPA-BOEDA-NPs thin film. The adsorption isotherm of water molecules showed a similar tendency to the adsorption isotherm of non-porous multimolecular adsorption. This was considered to be a change in the type of adsorbed water around the sulfonic acid groups.[35,36] The adsorption behaviors of BSPA-BOEDA and BSPA-BOEDA-NPs thin films with respect to RH were similar. The water uptake value gradually increased with increasing RH. It can be seen that the water uptake value of two thin films was the same under low humidity, but BSPA-BOEDA thin film showed a higher water uptake value (λ = 13.8) than BSPA-BOEDA-NPs (λ = 10.5) at 95% RH.

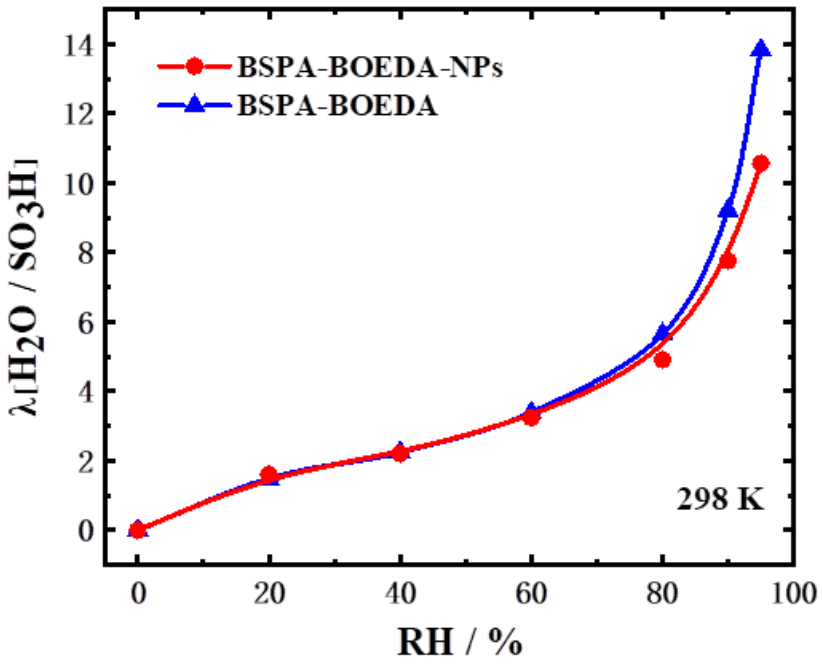

Figure 2-11. Water uptake of BSPA-BOEDA and BSPA-BOEDA-NPs thin films.

2.3.4 In situ FTIR

In order to evaluate the dissociation behavior of sulfonic acid protons, the RH-controlled in situ FTIR measurements were performed on BSAP-BOEDA and BSPA-BOEDA-NPs thin films. The spectra of BSPA-BOEDA and BSPA-BPEDA-NPs thin films under humidification are shown in Figure 2-12. The broad absorption band around 3420 cm^{-1} is attributed to the OH stretching vibration mode of water molecules under humidification.37,38 The absorbance of this band increased with increasing the RH, indicating that water molecules were adsorbed on the thin film under humidified conditions. Specifically, at 0% RH the absorption band of water molecules could not be observed, meanwhile, the band observed at 925 cm^{-1} could be attributed to the stretching vibration mode of the S-O bond in protonated sulfonic acid group. This band at was completely disappeared with increasing RH.

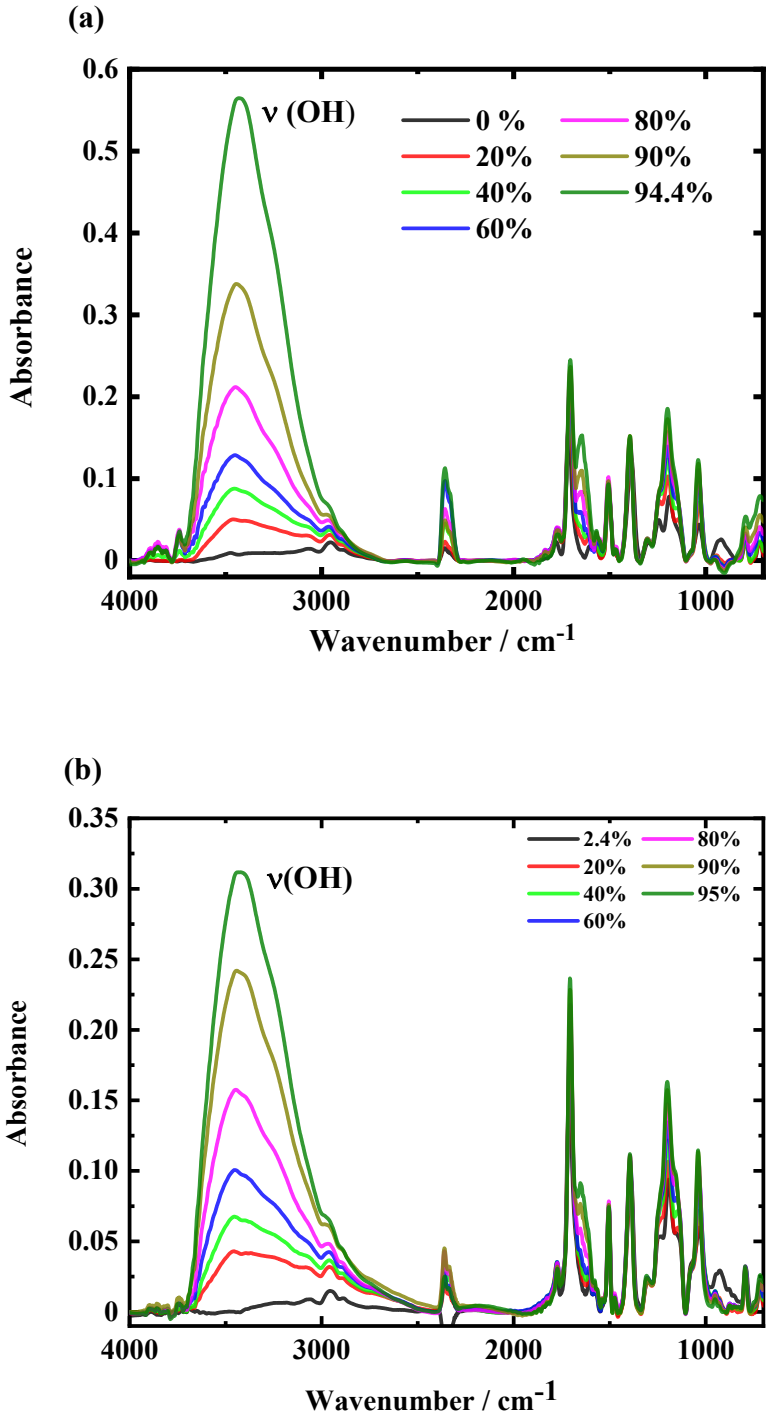

Figure 2-12. RH-dependent FTIR spectra of (a) BSPA-BOEDA thin film and (b) BSPA-BOEDA-NPs thin film in the range of 4000-700 cm^{-1}.

Subsequently, the molecular states of the sulfonic acid group of BSPA-BOEDA and BSPA-BOEDA-NPs thin films were analyzed. As shown in Figure 2-13, the absorption band attributed to the O=S=O symmetric stretching vibration (v_s (S=O)) of deprotonated sulfonic acid was observed at 1030-1040 cm^{-1}. We note that some sulfonic acid groups are deprotonated under the 0% RH. The peak area of v_s (S=O)

under different RH conditions was recorded as $S_x(SO_3^-)$, and the peak area of v_s (S=O) at 0% RH was recorded as $S_0(SO_3^-)$. The proton dissociation (PD / %) rate of the sulfonic acid group under each humidity condition is defined by the following equation:

$$PD(\%) = \frac{\left(S_{x(so_3^-)} - S_{0(so_3^-)}\right)}{\left(S_{95(so_3^-)} - S_{0(so_3^-)}\right)} \times 100\% \quad (2\text{-}4)$$

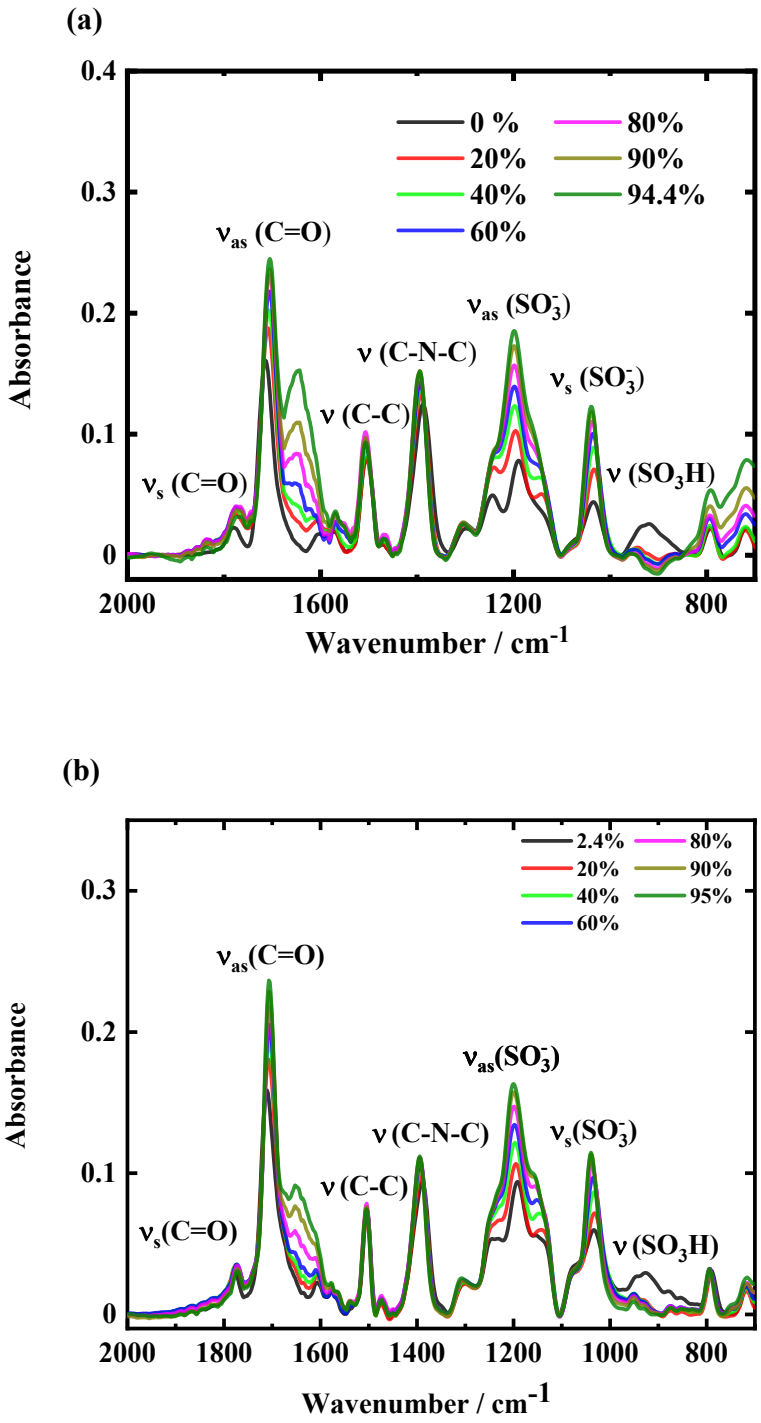

Figure 2-13. RH-dependent FTIR spectra of (a) BSPA-BOEDA and (b)BSPA-BOEDA-NPs thin films in the range of 4000-800 cm^{-1}.

The obtained PD values are plotted as a function of RH and the results are shown in Figure 2-14. The PD values of BSPA-BOEDA and BSPA-BOEDA-NPs thin films showed different increasing trends. The change in PD value of BSPA-BOEDA showed a non-linear trend similar to that of BSPA-CPDA in the

previous chapter. Below 60% RH, the PD value of BSPA-BOEDA increased to 70% rapidly, after that PD value slowly increases to 100%. On the other hand, the change in PD value of BSPA-BOEDA-NPs showed a linear change trend, indicating that even a small amount of cross-linked structure can lead to the change of sulfonic acid dissociation rate. Especially when the humidity is less than 60% RH, the PD value of BSPA-BOEDA-NPs is significantly lower than that of BSPA-BOEDA, indicating the sulfonic acid in BSPA-BOEDA-NPs becomes more difficult to dissociate due to the existence of the cross-linked structure even if the water uptake value is the same.

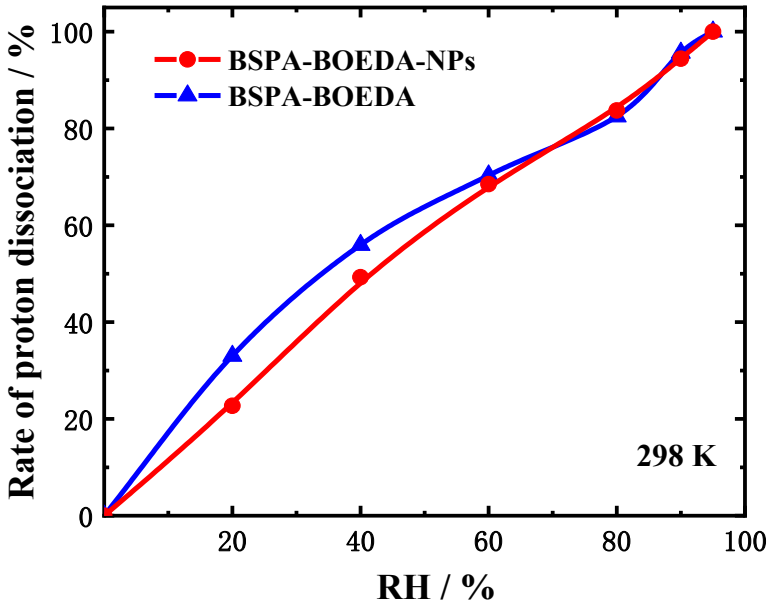

Figure 2-14. RH-dependent rate of proton dissociation of (a) BSPA-BOEDA and (b) BSPA-BOEDA-NPs thin films.

2.3.5 In situ GIXRS

GIXRS is a powerful tool for detecting molecular packings and molecular orderings in molecular organized thin films.[39,40] RH-dependent in situ GIXRS measurements on the BSPA-BOEDA and BSPA-BOEDA-NPs thin films were carried out to examine the effect of the semi-alicyclic main chain on the lyotropic ordered structure. The 2D scattering images are shown in Figures 3-15(a-d) and 1D GIXRS profiles in the in-plane and out-of-plane directions are shown in Figures 3-15(e, f). One broad scattering peak in both out-of-plane and in-plane directions was observed in both BSPA-BOEDA and BSPA-BOEDA-NPs thin films, indicating that the phase separation was formed. According to our previous reports, ASPIs

can form lamellar structures due to lyotropic LC property.[2,6,41] However, in this study, BSPA-BOEDA and BSPA-BOEDA-NPs thin films only formed a phase separation structure but not a long-range ordered lamellar structure.

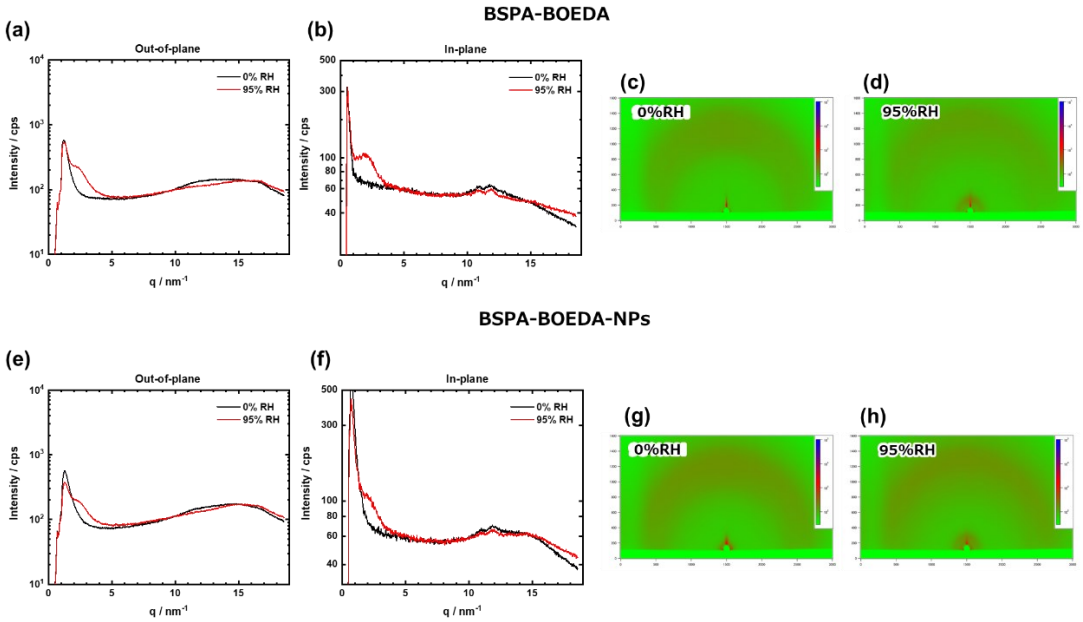

Figure 2-15. 1D GISAXS results of BSPA-BOEDA (a and b) and BSPA-BOEDA-NPs (f and g) thin films; 2D GISAXS results of BSPA-BOEDA (d and e) and BSPA-BOEDA-NPs (h and i) under 95% RH condition.

To understand the reason for only observing phase separation structure in BSPA-BOEDA and BSPA-BOEDA-NPs thin films, we tried to investigate the structural model. Figure 5 depicts the optimized oligomeric structures of 5 repeating units for BSPA-BOEDA and BSPA-CPDA by DFT calculation. The main chain of BSPA-BOEDA units showed lower rigidity. Therefore, BSPA-BOEDA and BSPA-BOEDA-NPs thin films with less rigid backbone only exhibit a phase separation structure but not long-range ordered lamellar due to weak lyotropic LC property.

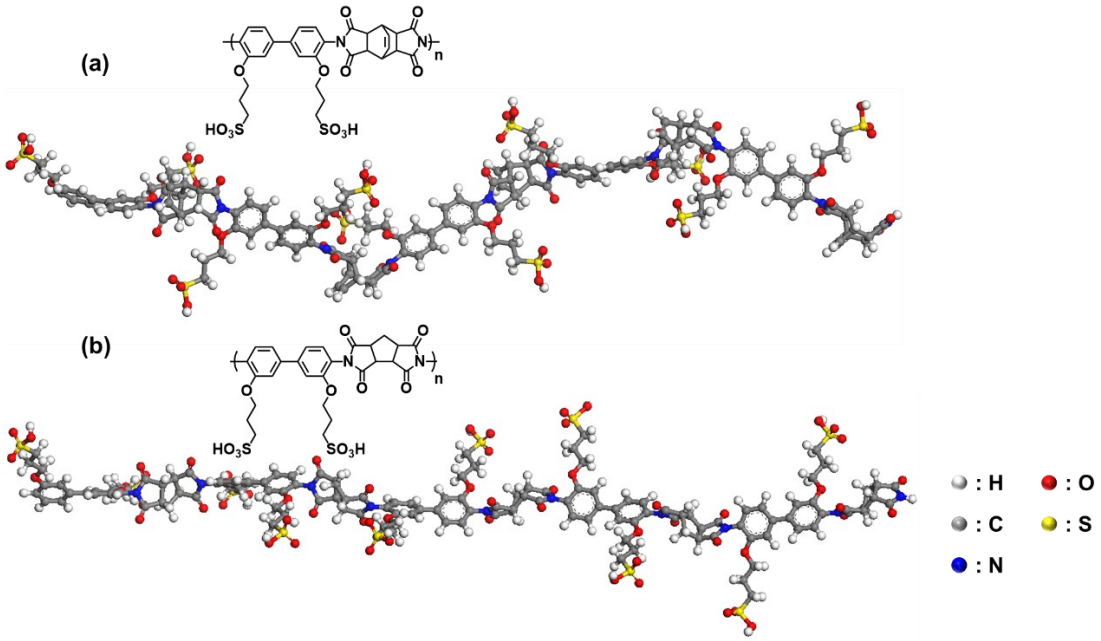

Figure 2-16. Optimized structures of 5 repeating units of BSPA-BOEDA and BSPA-CPDA.

2.3.6 Proton conductivity

The proton conductivity for the BSPA-BOEDA and BSPA-BOEDA-NPs thin film is shown in Figure 2-17a as a function of humidity at 298 K. The proton conductivity increased with increasing RH, which could be observed in typical proton-conducting polymers. The BSPA-BOEDA thin film exhibits a higher proton conductivity than BSPA-BOEDA-NPs thin film at all humidity conditions. The maximum proton conductivity reached 0.04 and 0.01 S cm^{-1} at 95% RH for BSPA-BOEDA and BSPA-BOEDA-NPs thin films, respectively. Compared with previously reported ASPIs, the proton conductivities of BSPA-BOEDA and BSPA-BOEDA-NPs are significantly lower. This is because BSPA-BOEDA and BSPA-BOEDA-NPs only form a phase separation structure but not form a lamellar structure, which cannot effectively promote proton transport. Even though the proton conductivity of BSPA-BOEDA-NPs thin film is lower than the reported ASPIs, it is still high compared to other cross-linked proton-conducting material membranes (Table 3-2). [19,20,21,22,42,43,44,45,46, 47,48,49]

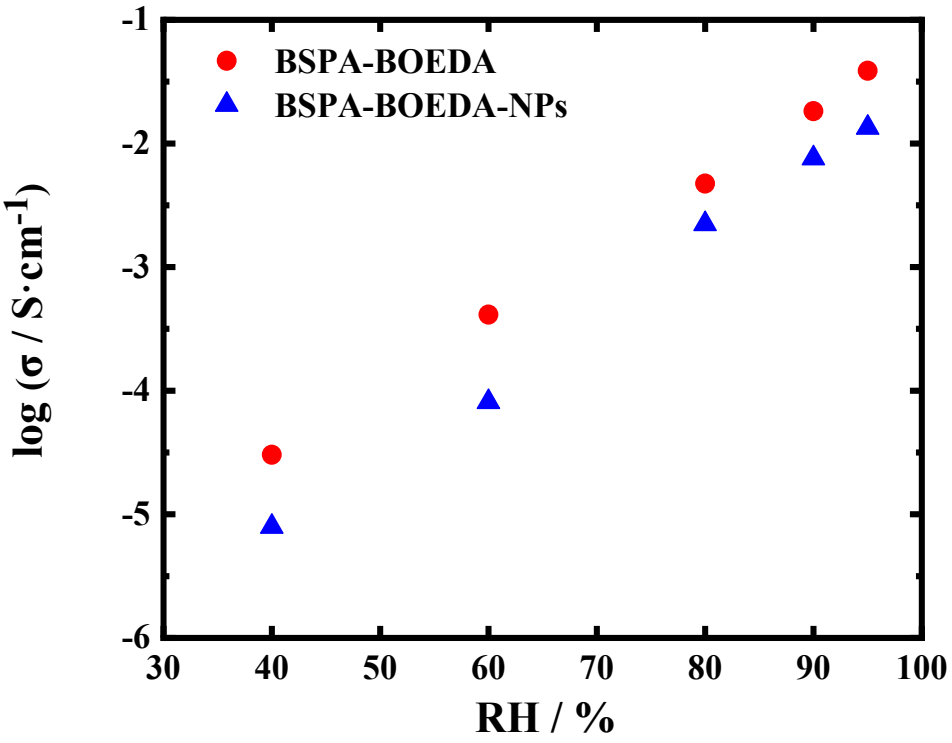

Figure 2-17. Proton conductivity of BSPA-BOEDA and BSPA-BOEDA-NPs thin films.

Table 2-2. Comparison of proton conductivity of BSPA-BOEDA-NPs thin film with reported materials.

Material	Form	T / ℃	RH / %	σ / S cm^{-1}
BSPA-BOEDA-NPs (This work)	Thin film (~ 500 nm)	25	95	0.01
Ref.19	Spin coating	90	100	0.07
Ref.20	Membrane (~ 30 μm)	30	90	0.093
Ref.21	Membrane (~ 40 μm)	80	100	0.11
Ref.22	Membrane (~ 50 μm)	80	100	0.11
Ref.42	Membrane (~ 50 μm)	90	90	0.1
Ref.43	Membrane (40-60 μm)	40	100	0.0014
Ref.44	Membrane (20-60 μm)	60	100	0.16
Ref.45	Membrane (~ 30 μm)	120	100	0.2
Ref.46	Membrane	80	90	0.15
Ref.47	Membrane (35-45 μm)	60	100	0.14
Ref.48	Membrane	30	95	0.061
Ref.49	Membrane	60	100	0.17

2.4 Conclusion

In this chapter, a semi-cycloaliphatic sulfonated polyimide (BSPA-BOEDA) containing a dienophile in its backbone was newly synthesized. A simple and readily available cross-linked thin film (BSPA-BPEDA-NPs) was obtained through the Fe^{3+}-catalyzed D-A reaction. The stability in water, water uptake, degree of sulfonic acid dissociation, morphology and proton conductivity were investigated for both BSPA-BOEDA and BSPA-BPEDA-NPs thin films. Compared with BSPA-BOEDA, the cross-linked BSPA-BPEDA-NPs membrane and thin film showed better stability in water. The water uptake of the two thin films was similar under low humidity conditions, but the water uptake of BSPA-BPEDA-NPs thin film was

less than that of BSPA-BOEDA under high humidity conditions. The sulfonic acid group dissociation of BSPA-BOEDA showed a non-linear increasing trend as a function of humidity, while BSPA-BPEDA-NPs showed a linearly increasing trend. And the sulfonic acid dissociation degree of BSPA-BPEDA-NPs is significantly smaller than that of BSPA-BOEDA at low humidity even though their water uptake is similar. The proton conductivity of BSPA-BPEDA-NPs thin film is lower than that of BSPA-BOEDA thin film due to the cross-linking, reaching maxima value of 0.01 and 0.04 S cm^{-1} at 25 °C and 95% RH, respectively. GIXRS results indicate that neither BSPA-BOEDA nor BSPA-BPEDA-NPs can form well-defined ordered structures but only form phase separation structure due to nonlinear molecular conformations confirmed by DFT calculation. This nonlinear molecular conformation reduces the lyotropic LC property, which is the intrinsic reason for its inability to form an ordered structure.

References

1. Nagao, Y. *et al.* Effect of Molecular Orientation to Proton Conductivity in Sulfonated Polyimides with bent backbones. *Mol. Cryst. Liq. Cryst.* **686**, 84–91 (2019).
2. Ono, Y. *et al.* High Proton Conduction of Organized Sulfonated Polyimide Thin Films with Planar and Bent Backbones. *Macromolecules* **51**, 3351–3359 (2018).
3. KRISHNAN, K. *et al.* Influence of Confined Polymer Structure on Proton Transport Property in Sulfonated Polyimide Thin Films. *Electrochemistry* **82**, 865–869 (2014).
4. Krishnan, K., Iwatsuki, H., Hara, M., Nagano, S. & Nagao, Y. Influence of Molecular Weight on Molecular Ordering and Proton Transport in Organized Sulfonated Polyimide Thin Films. *J. Phys. Chem. C* **119**, 21767–21774 (2015).
5. Nagao, Y. *et al.* Introducing planar hydrophobic groups into an alkyl-sulfonated rigid polyimide and how this affects morphology and proton conductivity. *Electrochim. Acta* **300**, 333–340 (2019).
6. Takakura, K. *et al.* Lyotropic ordering for high proton conductivity in sulfonated semialiphatic polyimide thin films. *Polym. J.* **51**, 31–39 (2019).
7. Kreuer, K. D. On the development of proton conducting polymer membranes for hydrogen and methanol fuel cells. *J. Memb. Sci.* **185**, 29–39 (2001).
8. Hsu, W. Y. & Gierke, T. D. Ion transport and clustering in nafion perfluorinated membranes. *J. Memb. Sci.* **13**, 307–326 (1983).
9. Woo, E. *et al.* Polyimide-PEG Segmented Block Copolymer Membranes with High Proton Conductivity by Improving Bicontinuous Nanostructure of Ionic Liquid-Doped Films. *Macromol. Chem. Phys.* **220**, 1–8 (2019).
10. Naoki Asano, Miyatake, K. & Watanabe, M. Sulfonated Block Polyimide Copolymers as a Proton-Conductive Membrane. *J. Polym. Sci. Part A Polym. Chem.* **44**, 2744–2748 (2006).
11. Narzary, B. B., Baker, B. C., Yadav, N., D'Elia, V. & Faul, C. F. J. Crosslinked porous polyimides: Structure, properties and applications. *Polym. Chem.* **12**, 6494–6514 (2021).
12. Bos, A., Pünt, I. G. M., Wessling, M. & Strathmann, H. Plasticization-resistant glassy polyimide membranes for CO2/CO4 separations. *Sep. Purif. Technol.* **14**, 27–39 (1998).
13. Xiao, Y., Low, B. T., Hosseini, S. S., Chung, T. S. & Paul, D. R. The strategies of molecular architecture and modification of polyimide-based membranes for CO2 removal from natural gas-A review. *Prog. Polym. Sci.* **34**, 561–580 (2009).
14. Kita, H., Inada, T., Tanaka, K. & Okamoto, K. ichi. Effect of photocrosslinking on permeability and permselectivity of gases through benzophenone- containing polyimide. *J. Memb. Sci.* **87**, 139–147 (1994).
15. Kratochvil, A. M. & Koros, W. J. Decarboxylation-induced cross-linking of a polyimide for enhanced CO 2 plasticization resistance. *Macromolecules* **41**, 7920–7927 (2008).
16. Rezac, M. E., Sorensen, E. T. & Beckham, H. W. Transport properties of crosslinkable polyimide blends. *J. Memb. Sci.* **136**, 249–259 (1997).
17. Zhang, G., Guo, X., Fang, J., Chen, K. & Okamoto, K. ichi. Preparation and properties of covalently cross-linked sulfonated copolyimide membranes containing benzimidazole groups. *J. Memb. Sci.* **326**, 708–713 (2009).
18. Yao, H. *et al.* Pendant-group cross-linked highly sulfonated co-polyimides for proton exchange

membranes. *J. Memb. Sci.* **480**, 83–92 (2015).
19. Sundar, S., Jang, W., Lee, C., Shul, Y. & Han, H. Crosslinked sulfonated polyimide networks as polymer electrolyte membranes in fuel cells. *J. Polym. Sci. Part B Polym. Phys.* **43**, 2370–2379 (2005).
20. Park, H. B. *et al.* Effect of crosslinked chain length in sulfonated polyimide membranes on water sorption, proton conduction, and methanol permeation properties. *J. Memb. Sci.* **285**, 432–443 (2006).
21. Yang, S. J., Jang, W., Lee, C., Shul, Y. G. & Han, H. The effect of crosslinked networks with poly(ethylene glycol) on sulfonated polyimide for polymer electrolyte membrane fuel cell. *J. Polym. Sci. Part B Polym. Phys.* **43**, 1455–1464 (2005).
22. Hu, M. *et al.* Cross-linked polymer electrolyte membrane based on a highly branched sulfonated polyimide with improved electrochemical properties for fuel cell applications. *Int. J. Energy Res.* **43**, 8753–8764 (2019).
23. Laina-Martín, V., Fernández-Salas, J. A. & Alemán, J. Organocatalytic Strategies for the Development of the Enantioselective Inverse-electron-demand Hetero-Diels-Alder Reaction. *Chem. – A Eur. J.* **27**, 12509–12520 (2021).
24. Gregoritza, M. & Brandl, F. P. The Diels–Alder reaction: A powerful tool for the design of drug delivery systems and biomaterials. *Eur. J. Pharm. Biopharm.* **97**, 438–453 (2015).
25. Yates, P. & Eaton, P. Acceleration of the diels-alder reaction by aluminum chloride. *J. Am. Chem. Soc.* **82**, 4436–4437 (1960).
26. Otto, S., Bertoncin, F. & Engberts, J. B. F. N. Lewis acid catalysis of a Diels-Alder reaction in water. *J. Am. Chem. Soc.* **118**, 7702–7707 (1996).
27. Tomifuji, R., Maeda, K., Takahashi, T., Kurahashi, T. & Matsubara, S. FeCl 3 as an Ion-Pairing Lewis Acid Catalyst. Formation of Highly Lewis Acidic FeCl 2+ and Thermodynamically Stable FeCl 4- to Catalyze the Aza-Diels-Alder Reaction with High Turnover Frequency. *Org. Lett.* **20**, 7474–7477 (2018).
28. Donatoni, M. C. *et al.* Solvent-free Diels-Alder reactions catalyzed by FeCl3 on Aerosil® silica. *Tetrahedron* **70**, 3231–3238 (2014).
29. Krishnan, K., Iwatsuki, H., Hara, M., Nagano, S. & Nagao, Y. Proton conductivity enhancement in oriented, sulfonated polyimide thin films. *J. Mater. Chem. A* **2**, 6895–6903 (2014).
30. Yin, Y. *et al.* Water stability of sulfonated polyimide membranes. *Macromolecules* **39**, 1189–1198 (2006).
31. Sung, J., Kim, D., Whang, C. N., Oh-E, M. & Yokoyama, H. Sum-frequency vibrational spectroscopic study of polyimide surfaces made by spin coating and ionized cluster beam deposition. *J. Phys. Chem. B* **108**, 10991–10996 (2004).
32. Sakamoto, K. *et al.* Determination of molecular orientation of very thin rubbed and unrubbed polyimide films. *J. Appl. Phys.* **80**, 431–439 (1996).
33. Shin, T. J., Lee, B., Youn, H. S., Lee, K. B. & Ree, M. Time-resolved synchrotron X-ray diffraction and infrared spectroscopic studies of imidization and structural evolution in a microscaled film of PMDA-3,4′-ODA poly(amic acid). *Langmuir* **17**, 7842–7850 (2001).
34. Miyatake, K., Yasuda, T., Michiko, H., Nanasawa, M. & Watanabe, M. Synthesis and properties of a polyimide containing pendant sulfophenoxypropoxy groups. *J. Polym. Sci. Part A Polym. Chem.* **46**, 157–163 (2007).
35. Hietpas, G. D., Sands, J. M. & Allara, D. L. Formation of a molecularly reconstructed surface layer during unidirectional rubbing of polyimide films. *Macromolecules* **31**, 3374–3378 (1998).

36. Fang, J. *et al.* Novel sulfonated polyimides as polyelectrolytes for fuel cell application: 1. Synthesis, proton conductivity, and water stability of polyimides from 4,4′-diaminodiphenyl ether-2,2′-disulfonic acid. *Macromolecules* **35**, 9022–9028 (2002).
37. Buzzoni, R., Bordiga, S., Ricchiardi, G., Spoto, G. & Zecchina, A. Interaction of H2O, CH3OH, (CH3)2O, CH3CN, and Pyridine with the Superacid Perfluorosulfonic Membrane Nafion: An IR and Raman Study. *J. Phys. Chem.* **99**, 11937–11951 (1995).
38. Pei, W., Wang, Y. J. & Yu, C. Q. Diels-Alder reactions of N-functionalized acryloyl α-pyrrolidone derivatives using FeCl3·6H2O as an efficient catalyst under solvent-free conditions. *Chinese J. Chem.* **25**, 814–817 (2007).
39. Nagano, S., Kodama, S. & Seki, T. Ideal spread monolayer and multilayer formation of fully hydrophobic polythiophenes via liquid crystal hybridization on water. *Langmuir* **24**, 10498–10504 (2008).
40. Nagano, S. Inducing Planar Orientation in Side-Chain Liquid-Crystalline Polymer Systems via Interfacial Control. *Chem. Rec.* **16**, 378–392 (2016).
41. Nagao, Y. Proton-Conductivity Enhancement in Polymer Thin Films. *Langmuir* **33**, 12547–12558 (2017).
42. Lee, C. H., Park, H. B., Chung, Y. S., Lee, Y. M. & Freeman, B. D. Water Sorption, Proton Conduction, and Methanol Permeation Properties of Sulfonated Polyimide Membranes Cross-Linked with N,N-Bis(2-hydroxyethyl)-2-aminoethanesulfonic Acid (BES) permeation properties. *J. Memb. Sci.* **39**, 755–764 (2005).
43. Pan, H. *et al.* Preparation and properties of the cross-linked sulfonated polyimide containing benzimidazole as electrolyte membranes in fuel cells. *J. Memb. Sci.* **476**, 87–94 (2015).
44. Fang, J., Zhai, F., Guo, X., Xu, H. & Okamoto, K. I. A facile approach for the preparation of cross-linked sulfonated polyimide membranes for fuel cell application. *J. Mater. Chem.* **17**, 1102–1108 (2007).
45. Yin, Y., Hayashi, S., Yamada, O., Kita, H. & Okamoto, K. I. Branched/crosslinked sulfonated polyimide membranes for polymer electrolyte fuel cells. *Macromol. Rapid Commun.* **26**, 696–700 (2005).
46. Ye, Y. S., Huang, Y. J., Cheng, C. C. & Chang, F. C. A new supramolecular sulfonated polyimide for use in proton exchange membranes for fuel cells. *Chem. Commun.* **46**, 7554–7556 (2010).
47. Endo, N. *et al.* Cross-Linked Sulfonated Polyimide Membranes for Polymer Electrolyte Fuel Cells. *J. Electrochem. Soc.* **156**, B628 (2009).
48. Lee, C. H. *et al.* Water-stable crosslinked sulfonated polyimide-silica nanocomposite containing interpenetrating polymer network. *J. Power Sources* **163**, 339–348 (2006).
49. Kido, M. *et al.* Novel preparation method of cross-linked sulfonated polyimide membranes for fuel cell application. *Chem. Lett.* **36**, 272–273 (2007).

Chapter 3

Lyotropic Liquid Crystalline Property and Organized Structure in High Proton-Conductive Sulfonated Semi-Alicyclic Oligoimide Thin Films

Abstract

Fully aromatic sulfonated polyimides with rigid backbone can form lamellar structure under humidified conditions, which is facilitated to the transmission of protons in ionomers. Herein, we synthesized a new sulfonated semi-alicyclic oligoimide composed of 1,2,3,4-cyclopentanetetracarboxylic dianhydride (CPDA) and 3,3'-bis¬(sulfopropoxy)-4,4'-diaminobiphenyl (BSPA) to investigate the influence of molecular organized structure and proton conductivity with lower molecular weight than before. The weight average molecular weight (Mw) determined by gel permeation chromatography (GPC) was 9300. Humidity controlled Grazing Incidence Small-Angle X-ray Scattering (GIXRS) revealed that one scattering was observed in the out-of-plane direction and scattering position shifted to lower angle as the humidity increased. A loosely packed lamellar structure was formed by a lyotropic liquid crystalline property. Although the ch-pack aggregation of the present oligomer reduced by the substitution to the semi-alicyclic CPDA from the aromatic backbone, we observed the formation of a distinct organized structure in the oligomeric form because of the relatively rigid backbone. This is the first-time observation of the lamellar structure in such low molecular weight oligoimide thin film. The thin film exhibited a high conductivity of 2.1×10^{-1} S cm^{-1} under 25 ℃ and 95% relative humidity (RH). This value was the highest conductivity compared to the other reported sulfonated polyimide thin films with comparable molecular weight.

3.1 Introduction

Since the great success of perfluorosulfonic acid polymer Nafion designed by DuPont in fuel cell applications, the design of proton-conducting polymers has mostly been based on the phase separation between hydrophilic and hydrophobic components. However, these materials usually do not possess well-defined long-range ordered structures, which makes it difficult to deeply discuss the relationship between structure and proton conductivity.[1,2,3,4,5,6 7] After decades of research, designing polymers with efficient proton transport channels based on well-defined phase segregation is a basic principle for development of high-performance proton-conducting materials.[5,6,7,8]

Ikkala et al. firstly observed a temperature-dependent change in proton conductivity during the order-disorder or order-to-order structural changes in copolymers.[9] Kato et al. reported the pioneering work on the anisotropy of proton conductivity in thermotropic liquid crystal (LC) materials and demonstrated that higher proton conductivity can be obtained in channels formed by the liquid crystal.[10,11,12] Rikukawa et al. observed anisotropic proton conductivity and swelling behavior in sulfonated poly(4-phenoxybenzoyl-1,4-phenylene)s (s-PPBPs) and proposed that this is due to the formation of liquid crystal phase by s-PPBPs in DMSO solution.[13] Matsui et al. used poly (N-dodecylacrylamide-co-acrylic acid) to obtain thin films with well-defined lamellar structures and demonstrated a huge difference in proton conductivity between in-plane and out-of-plane directions.[14]

Recently, alkyl-sulfonated polyimides (ASPIs) have attracted attention again, not only because of their good mechanical properties and proton conductivity, but also because of their ability to form an ordered structure under humidified conditions. Ando et al. first demonstrated the existence of ordered liquid crystal phases in fully aromatic and semi-aliphatic polyimides (PIs) molecules by grazing incidence wide-angle X-ray scattering.[15] Krishnan et al. obtained proton conductivity as high as 0.26 S cm^{-1} (at 25 °C and 95% RH) in the direction parallel to the substrate surface in ASPI thin film, which is an order of magnitude higher than its bulk membrane.[16] They attribute this to the formation of a lamellar ordered structure parallel to the substrate under humidified conditions and propose that the formation of this ordered structure is driven by lyotropic LC property. The molecules with both rigid backbones and highly soluble side chains such as ASPIs exhibit the lyotropic liquid crystalline (LC) properties in solutions due to excluded volume effects.[17] These findings have brought a new perspective to investigate the relationship between structure and proton transport.[18,19,20,21,22,23,24,25,26,27,28,29]

Our previous studies have shown that the enhancement of molecular order in ASPIs can improve proton conductivity effectively.[16,30,31,32,33,34] These efforts have focused on the study of fully aromatic sulfonated polyimides, but studies on the effects of introducing aliphatic ring structures into polyimide backbones to the molecular order and proton conductivity are still inadequate. Ono et al. demonstrated that the increased backbone rigidity facilitates the formation of organized lamellar structures in ASPI thin films.[35] Therefore, the introduction of an aliphatic ring to the ASPI's backbone is regarded as reducing the backbone rigidity and inhibiting the formation of ordered structures. Both Krishnan et al. and Takakura et al. have proved that ASPIs with higher molecular weights enhance a degree of molecular ordering to form well-organized structures.[31,36] In the case of lower molecular weight ASPIs, especially with alicyclic structures, only weak lamellar structures can be observed.

In this study, the relationship between ordered structure and proton conductivity was investigated by introducing a cyclopentane structure into the imide backbone. The cyclopentane structure, compared to the previous cyclohexane structure which enhances linear conformation of backbone confirmed by density functional theory (DFT) calculation, can be anticipated for the changes in the molecular structure and organization by the lyotropic LC property. Grazing-incidence X-ray scattering (GIXRS) technique has been proven to be suitable for structural studies.34 Therefore, we used relative humidity (RH)-controlled GIXRS to investigate the nanostructure of alkyl-sulfonated semi-alicyclic oligoimide thin films composed of 1,2,3,4-cyclopentanetetracarboxylic dianhydride (CPDA) and 3,3'-bis(sulfopropoxy)-4,4'-diaminobiphenyl (BSPA). The dissociation state of the proton from sulfonic acid groups and proton conductivity at different humidity were also investigated using RH in situ Fourier transform infrared (FTIR) spectroscopy and impedance spectroscopy, respectively. The results show that the newly synthesized alkyl-sulfonated semi-alicyclic oligoimide forms a lamellar structure and shows high proton conductivity of 0.2 (±0.01) S cm-1. This value is the highest conductivity compared to the other reported sulfonated polyimide thin films with comparable molecular weight.

3.2 Experimental section

3.2.1. Materials

3,3'-Bis(sulfopropoxy)-4,4'-diaminobiphenyl (BSPA) was synthesized according to previous reports.[16,30] Triethylamine (TEA) was used as received from Kanto Chemical Co. Inc., Japan. Hydrochloric acid,

m-cresol, acetic acid, acetic anhydride, methanol, and acetone were obtained from Fujifilm Wako Pure Chemical Corp., Japan. 1,2,3,4-Cyclopentanetetracarboxylic dianhydride was purchased from Tokyo Chemical Industry Co. Ltd., Japan.

3.2.2 Synthetic route of 3,3'-bis(sulfopropoxy)-4,4'-diaminobiphenyl (BSPA)

The synthetic route of 3,3'-bis(sulfopropoxy)-4,4'-diaminobiphenyl (BSPA) is shown in scheme 3-1. The detailed steps are described as follows

Step 1: Protection of amine groups

3,3'-dihydroxybenzidine (Tokyo Chemical Industry Co., Ltd.) 5 g, Acetic anhydride (Fujifilm Wako Pure Chemical Corporation) 79 ml, acetic acid (Wako) 1.5 ml, water (18 MΩ cm^{-1}) 200 ml were added into the Erlenmeyer flask and stirring at 70-80 °C for 2 h. After cooling to room temperature, the mixture was further cool down by the ice bath. The solid product was separated from the mixture by centrifuge 5804 (Eppendorf) and washed several times by acetone. The calculated yield was 97% after the product had dried overnight in a vacuum.

Step 2: Introduction of sulfonated side chains

The acetylated 3,3'-dihydroxybenzidine, 1,3-Propanesulton (Tokyo Chemical Industry Co., Ltd.) and sodium hydroxide (Fujifilm Wako Pure Chemical Corporation) were added into a three-necked flask equipped with a molar ratio of 1: 3: 3, respectively. 150 ml methanol was added into the flask to dissolve all the chemicals. Under the protection of argon atmosphere, the reaction was refluxed at 80 °C for 6 hours. The solution was black at the beginning of the reaction and turned yellowish-brown after about 1.5 h. After sufficient cooling ice bath, the solid product was separated from the mixture by centrifuged, and the product was washed several times with methanol and acetone. The dried product was weighed after being vacuum dried overnight, and the yield was 50.3%. Based on NMR results, the sulfonation rate was calculated as 95%.

Step 3: Ion exchange

The solid product obtained in the previous step was dissolved in water (18 MΩ cm^{-1}). The aqueous solution flowed through a glass column filled with ion exchange resin Amberlyst 31WET (Organo) slowly.

This process was repeated 5 times in order to exchange sodium ions into hydrogen ions as much as possible. Then the water was removed by rotary evaporator (Yamato Science).

Step 4: Removal of protective groups

The ion-exchanged product was dissolved in 100 ml of hydrochloric acid (Fujifilm Wako Pure Chemical Corporation). In a three-necked flask with a magnetic stirrer, the solution was refluxed at 120 °C for 2 hours under the protection of argon atmosphere. After that, the condenser tube was removed, and the temperature was raised to 150 °C for dry distillation. The evaporated hydrochloric acid was absorbed with a sodium hydroxide solution prepared in advance. The obtained product was washed with 2-propanol and acetone and then sufficiently dried to obtain a final product BSPA. The final yield was 47%

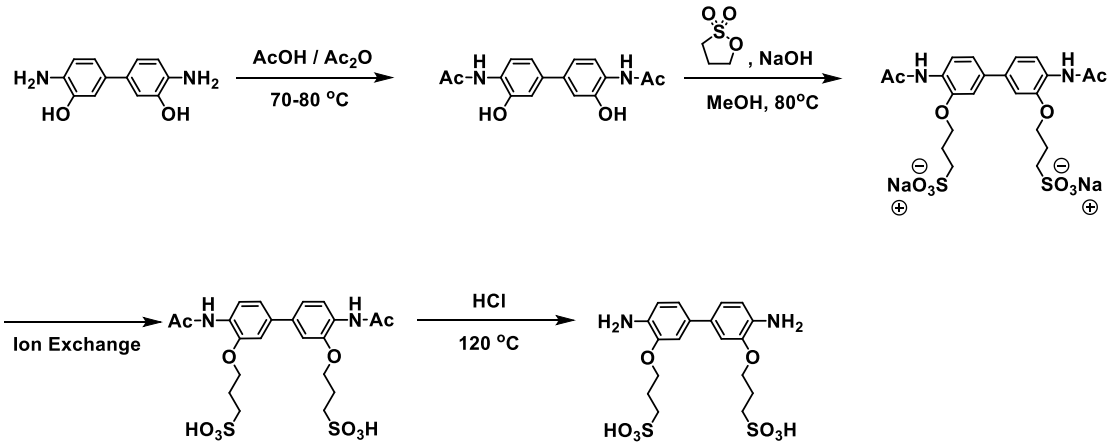

Scheme 3-1. Scheme for synthesizing BSPA.

3.2.3 Synthetic route of BSPA-CPDA

The synthetic route of BSPA-CPDA is shown in Scheme 3-2. BSPA 0.46 g (1 mmol) and CPDA 0.21 g (1 mmol) were added into a three-necked flask with magnetic stirring. 10 ml m-cresol (Fujifilm Wako Pure Chemical Corporation) was added to the three-necked flask as a solvent. Then 600 μl triethylamine (Kanto Chemical Co. Inc) was added into the flask.

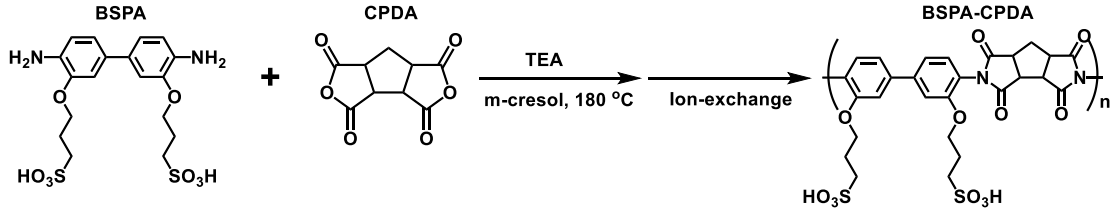

Scheme 3-2. Scheme for synthesizing BSPA-CPDA.

Under the protection of argon atmosphere, the reaction was first performed at 80 °C for 2 h. Then,

the temperature was raised to 180 ℃ and the reaction was continued for 20 h. After the reaction, the resulting solution was cooled to room temperature, and further cooled in ice bath for 30 minutes. The cooled solution was added to 100 ml of cold fresh acetone to obtain a white flocculent precipitate. The solid product was obtained by centrifugation and washed several times with acetone, then dried under vacuum overnight. The dried product was then dissolved in water, and ion exchange was carried out using a glass column packed with ion exchange resin Amberlyst 31WET (Organo). This process was repeated several times to ensure that sulfonate was exchanged to sulfonic acid as much as possible. The solvent was removed by rotary evaporation and the final product BSPA-CPDA was obtained after completely drying.

3.2.4 Characterization

3.2.4.1 Nuclear magnetic resonance (NMR)

The ^{1}H nuclear magnetic resonance (NMR, Bruker Avance III (400 MHz) spectrometer; Bruker Analytik GmbH) spectra was used to determine whether the monomer and oligomer was successfully synthesized. Approximately 3 mg of monomer or oligomer was dissolved in a 600 μl dimethyl sulfoxide (DMSO) solution containing 0.03% of trimethylsilane (TMS) for NMR determination. After the measurement, software 1D NMR was used to integrate the results.

3.2.4.2 Infrared (IR) spectroscopy

The Fourier Transform Infrared Spectroscopy of monomer and oligomer was measured by Attenuated Total Reflection (FT-IR ATR). The used device was Nicolet 6700 (Thermo Fisher Scientific Inc.) and the analysis software used was OMNIC (Thermo Fisher Scientific Inc.). The sample powder is evenly coated on the prism and compacted with equipment to make the sample fully contact the prism, following the sample was measured. The background spectrum and the sample spectrum were scanned 64 times to obtain the correct spectral image. The obtained spectrum was corrected by using Advanced ATR Correction. The measurement range was 400-4000 cm^{-1}.

3.2.4.3 Gel permeation chromatography (GPC)

The molecular weight of BSPA-CPDA was measured by gel permeation chromatography (GPC), and the equipment used was LC-2000plus (JASCO). The mobile phase solution was obtained by mixing 10.26

g of $NaNO_3$ (Kanto Chemical Co. Inc), 600 ml of water, 400 ml of N, N'-dimethylformamide (DMF) (Fujifilm Wako Pure Chemical Corporation) and 18 mL of acetic acid. The preparation method of the measurement solution containing BSPA-CPDA is described as follows:

0.03 wt% of BSPA-CPDA was added to 3ml of the mobile phase solution and stir it thoroughly to dissolve it. The solution containing BSPA-CPDA was filtered by a syringe with a filter, then transfer the filtered solution to a screw cap bottle with a silicone cap. 50 μl of the prepared solution was injected into the device by microsampler. The molecular weight of the sample was calculated by comparing it with a standard curve drawn with standard materials in advance. The method of making the standard curve is as follows. Several polystyrenes with exact molecular weight (Mw = 759000, 580000, 290000, 101000, 23600) were dissolved in mobile solution to prepare a standard solution. GPC measurement was performed on the standard solution, and the obtained results were fitted into a standard curve.

3.2.5 Thin film preparation

The spin coating (ACT-200 spin-coater; Active Co. Ltd.) method was used to prepare thin films. BSPA-CPDA was dissolved in the 1: 1 (w / w) of water and Tetrahydrofuran (THF) (Fujifilm Wako Pure Chemical Corporation). The thickness of thin films was controled about 500 nm. The the Si, SiO_2 substrates (E&M Co. Ltd.) and SiO2-coated 9 MHz quartz crystals (Seiko EG&G Co. Ltd.) were washed by 2-propanol in advance. Before thin film deposition, plasma treatment (Cute-MP; Femto Science, Korea) was carried out to improve the hydrophilic properties of the substrate surface.

3.2.6 Water uptake

The water uptake was measured with the humidity-controlled in situ quartz crystal microbalance (in-situ QCM) system. The diagram of the QCM substrate used in the measurement is shown in Figure 3-1. The schematic diagram of the measuring device is shown in Figure 3-2. Various relative humidity (RH) was generated by humidity generator Bel Flow (MicrotracBEL Corp.) through mixing dry N_2 gas and steam. The QCM substrate was placed in a self-made humidity control chamber with a high-resolution RH sensor and was connected to the oscillation circuit and the frequency counter 5313A (Agilent Technologies) through a circuit. The weight change of the film can be calculated by using the Sauerbrey equation.

$$\Delta m = \frac{S \times \sqrt{\rho \mu}}{2 \times F^2} \times (-\Delta F) \quad (3\text{-}1)$$

where S is the electrode surface area. ρ, and μ stand for the quartz density and quartz shear modulus,

respectively. F is for the fundamental frequency of QCM substrate. The number of water molecules adsorbed per sulfonic acid group (water uptake / λ) was calculated by the following formula as shown below,

$$\lambda = (\frac{m}{m_0} - 1) \times \frac{EW}{M_{H_2O}} \quad (3\text{-}2)$$

where *m* represents the mass of the film under each humidity, m_0 represents mass of the film at the dry condition, M (H_2O) is the molecular weight of water molecules, and *EW* expresses the equivalent weight of each sulfonic acid group

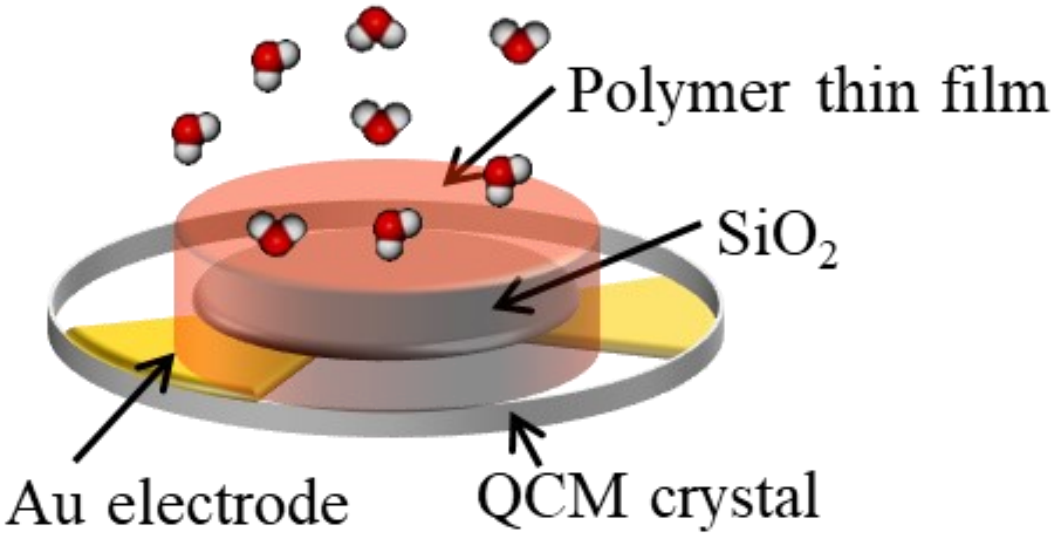

Figure 3-1. Schematic illustration of the quartz crystal microbalance devices.

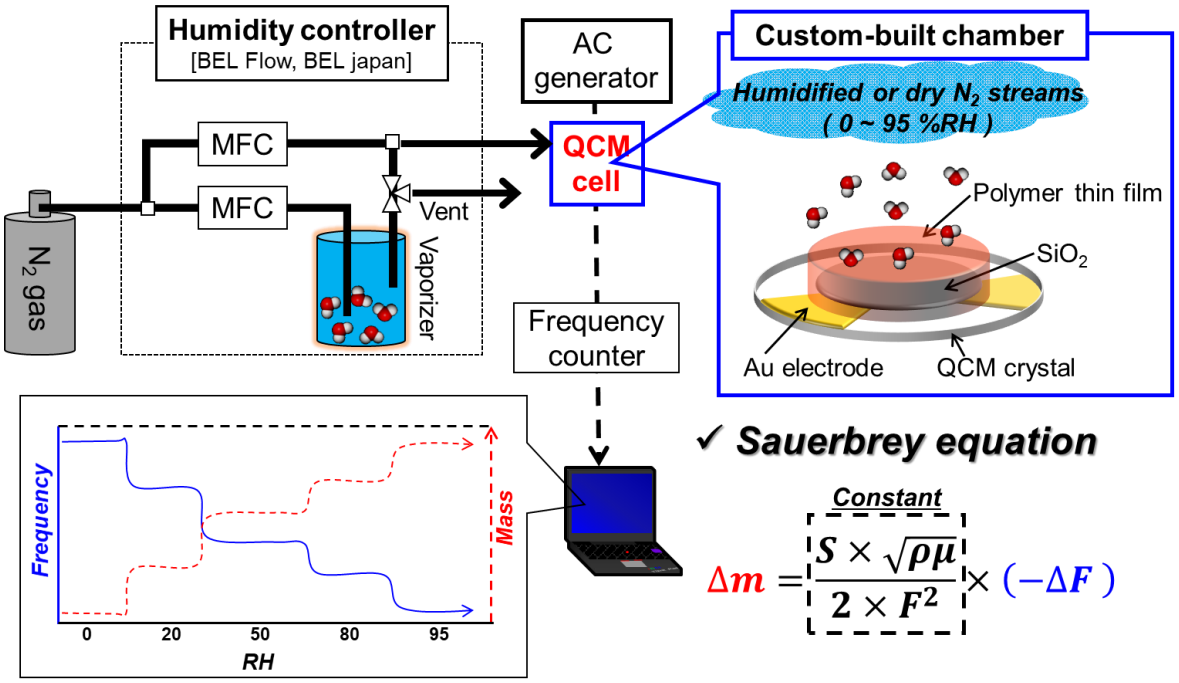

Figure 3-2. Schematic illustration of in-situ QCM measurement.

3.2.7 In situ FTIR

The dissociation state of the sulfonic acid group was investigated by RH controlled in situ FTIR measurements. The schematic diagram of the measuring system is shown in Figure 3-3. The thin film sample made on silicon wafers was placed in homemade chambers. In the humidity-controlled cell, CaF_2 windows were employed. An FTIR spectrometer (Nicolet 6700; Thermo Fisher Scientific Inc.) equipped with a deuterium triglycine sulfate (DTGS) detector was used for transmission in situ FTIR measurements. The RH change was controlled within the range of 0-95% through a humidity generator (me-40DP-2PW; Microequipment). When only nitrogen gas was flowing, the RH was defined as 0%.

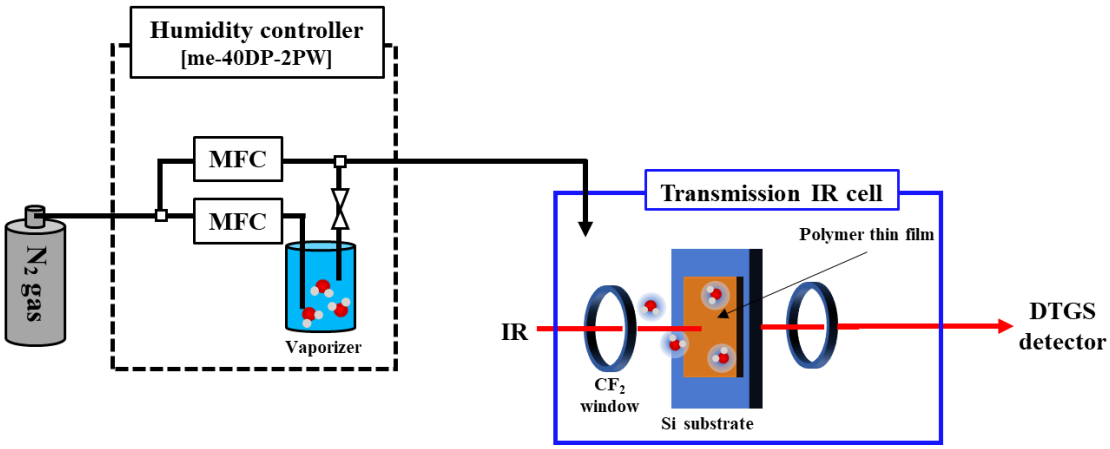

Figure 3-3. Schematic illustration of in-situ FT-IR measurement under humidity control.

3.2.8 Grazing incidence X-ray scattering (GIXRS)

RH in situ GIXRS was measured by a FR-E X-ray diffractometer equipped with R-AXIS IV two-dimensional (2D) detector (FR-E; Rigaku Corp.). The schematic diagram of the measuring system is shown in Figure 3-4. The thin film sample was placed in a humidity-controlled cell with X-ray transparent polyester film (Lumirror) windows. The humidity in the cell was controlled using the humidity generator me-40DP series. X-rays with wavelength of 0.1542 nm were generated through Cu Kα radiation and have a beam size of approximately ϕ300 μm. The camera length was 300 mm, and the incidence angle was set in the range of 0.20°-0.22°.

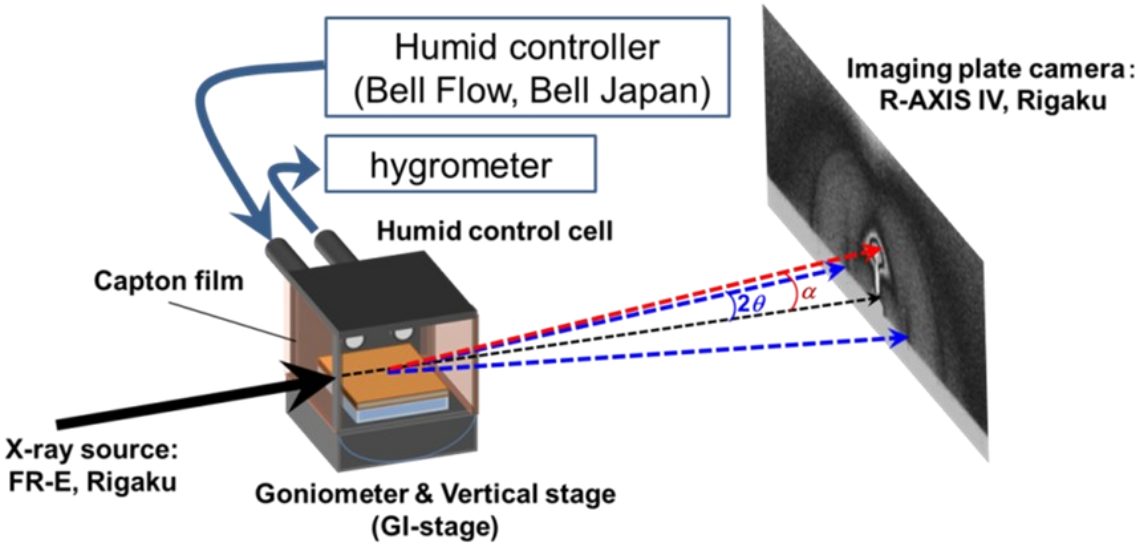

Figure 3-4. Schematic illustration of in-situ GISAXS measurement.

3.2.9 Molecular structure simulation

The optimized molecular structures were calculated by Material Studio 2020. The calculations were done based on DFT using a DMol3 module. The generalized gradient approximation (GGA) functional with the Perdew-Burke-Ernzerhof (PBE) type were used to model the exchange and correlation interactions. Convergence threshold for the maximum force and maximum displacement for normal geometry optimization were set, respectively, to 0.002 Ha Å-1 and 0.005 Å.

3.2.10 Proton conductivity

The proton conductivity of the BSPA-CPDA thin film in the direction parallel to a substrate surface was measured by alternating current (AC) electrochemical impedance spectroscopy (EIS). The schematic diagram of the measuring system is shown in Figure 3-5. The frequency response analyzer

and high-frequency dielectric interface (SI1260 and SI1296; Solartron Analytical) were used to measure the impedance. A humidity- and temperature-controlled chamber (SH-221; Espec Corp.) was used to control the humidity and temperature during the experiment. The impedance was measured when an AC voltage of 50 mV was applied, and the frequency was scanned in the range of 1 Hz to 10 MHz. The RH was controlled between 40% and 95%, and the temperature was stable at 298 K. The collected impedance values (R) were converted to the conductivity of thin film directly by the following equation,

$$\sigma = \frac{d}{Rlt} \tag{3-3}$$

where *t* and *l* stand for the film thickness and contact electrode length, respectively. *d* represents the distance between the two gold electrodes.

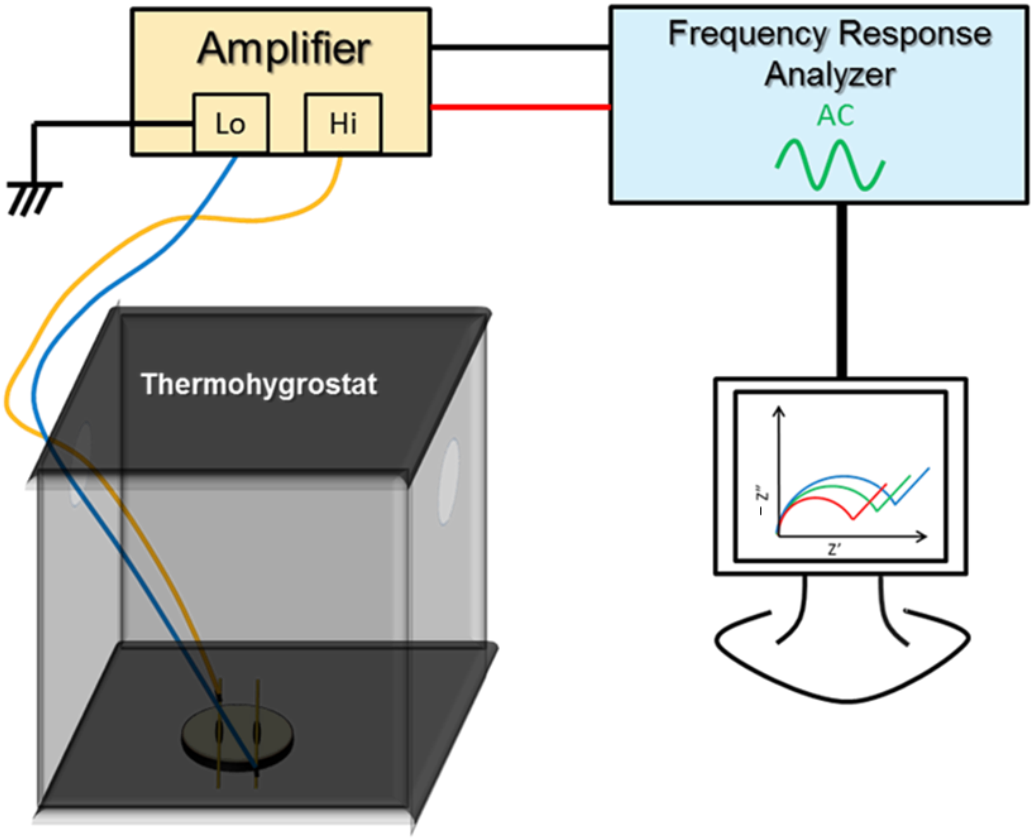

Figure 3-5. Schematic illustration of AC impedance method.

3.3 Results and discussions

3.3.1 Characterizations

3.3.1.1 ^{1}H nuclear magnetic resonance (^{1}H NMR)

The structure and ^{1}H NMR results of each step in the monomer BSPA synthesis are shown in Figure

3-1, and the structure and ^{1}H NMR results of the polymer are shown in Figure 3-6.

In all results, the peak appearing around 2.5 ppm was attributed to DMSO-d6. In the NMR results of the monomer, the water peak appeared near 3.3-3.5 ppm, while in the NMR results of the polymer, the water peak appeared at 5.0-5.8 ppm and the peak was broad. In Figure 3-1, the peak of the proton on the benzene ring appeared near 6.9-7.9 ppm, and the peak of the proton on the alkoxy chain appears near 2.1-4.2 ppm. The sulfonation rate obtained from the integrated value was around 95%. In the polymer NMR results in Figure 3-7, peaks from the possible by-product amide or carboxyl group were not observed, which proved that the imidization reaction was complete. Integration of proton peaks in ^{1}H NMR spectra was in good agreement with the number of protons in both the backbone and side chain of BSPA-CPDA structure. Before ion exchange, the prepared polymer exhibits the TEA trace (red arrow), which also dominant in the spectrum. After ion exchange, the prepared polymer exhibit that the TEA amount reduced considerably, which is less than 1% comparing to before ion exchange.

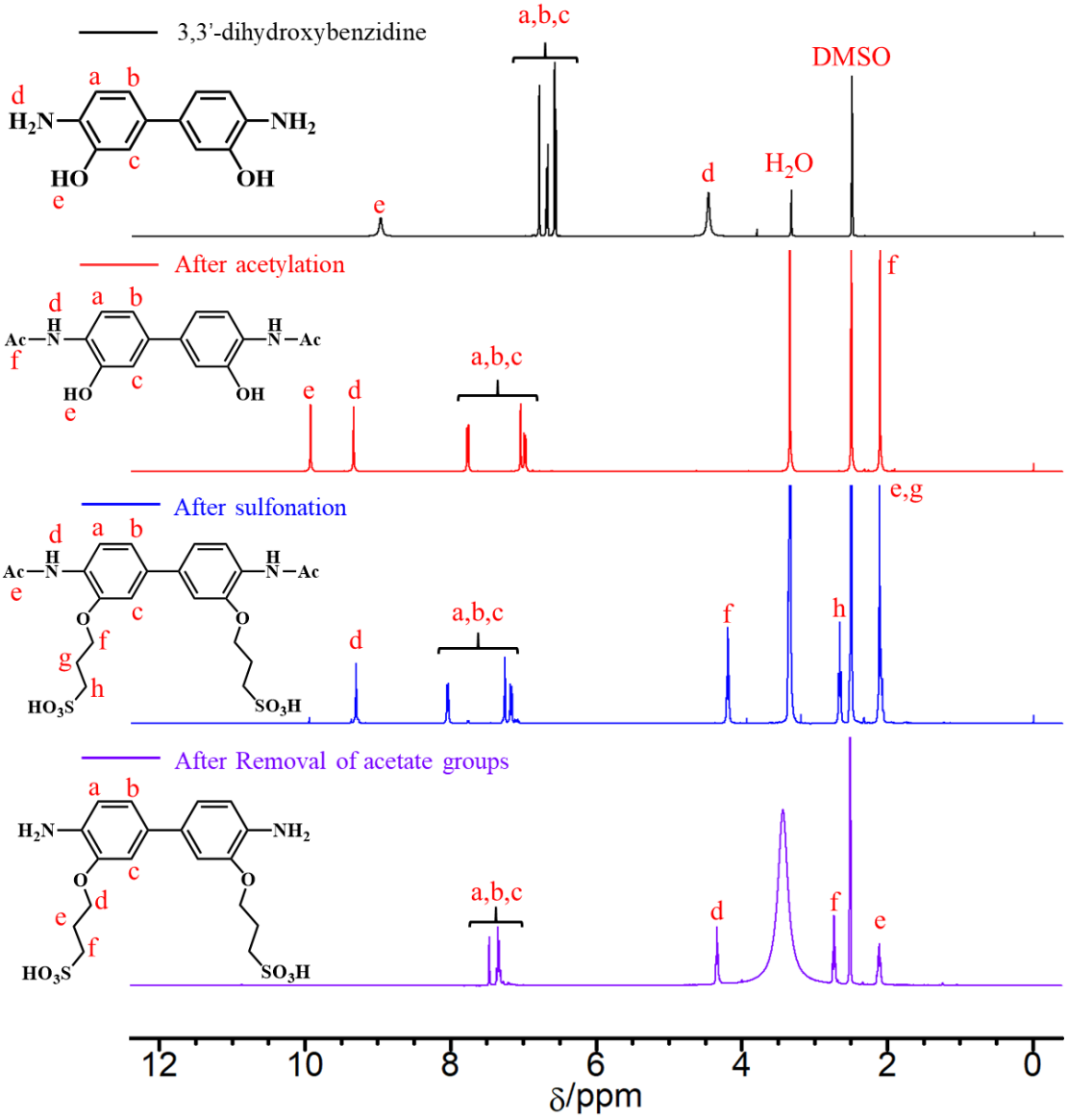

Figure 3-6. ^{1}H NMR（DMSO-d6）spectra of BSPA.

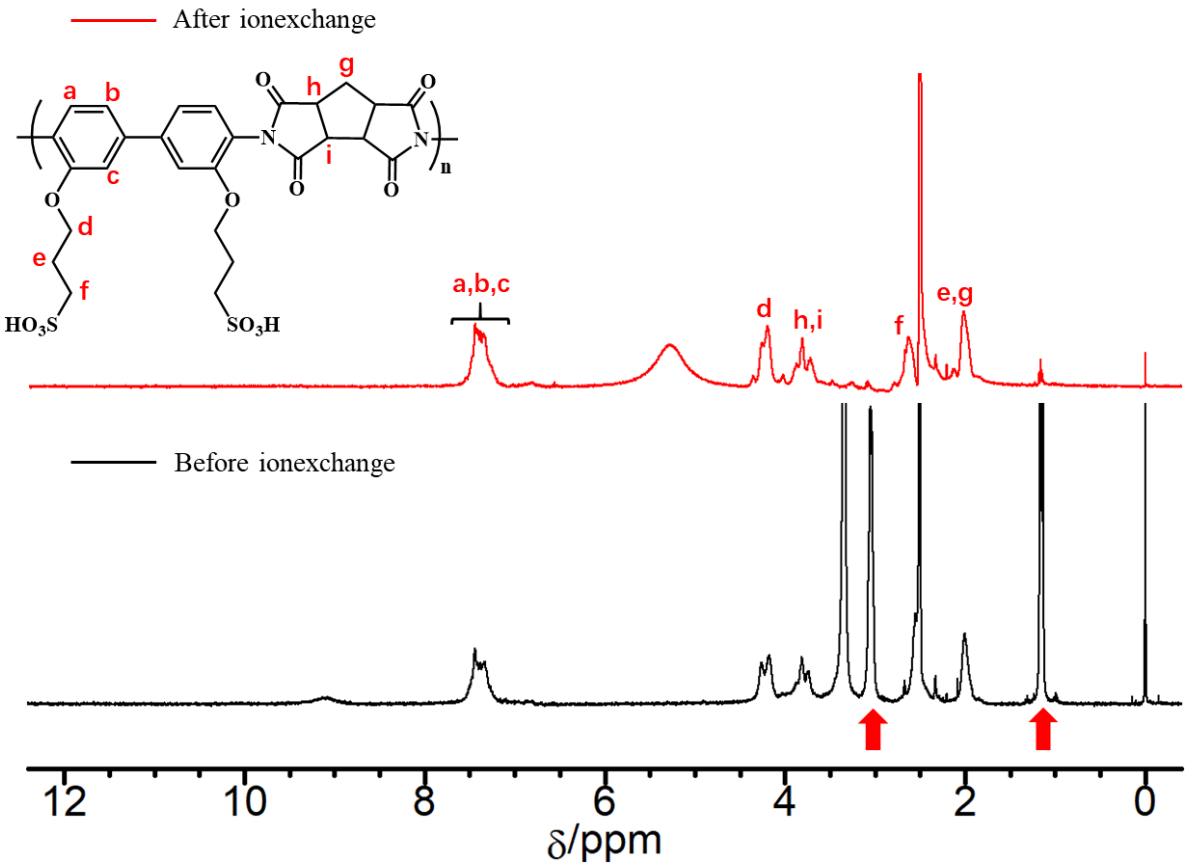

Figure 3-7. ^{1}H NMR (DMSO-d_6) spectra for each BSPA-CPDA.

3.3.1.2 FT-IR ATR study

FTIR-ATR spectra of BSPA and BSPA-CPDA are shown in Figure 3-8. The absorption peaks of v_{sym} (C=O) 、v_{asym} (C=O) and v (C-N) which are typical imide bond were observed at 1778 cm^{-1},1706 cm^{-1} and 1383 cm^{-1}, respectively.[37,38,39,40] Since δ (N-H) observed at 1629 cm^{-1} of 3,3'-BSPA was not observed in BSPA-CPDA, indicating that the imidization reaction was completed. In addition, since δ (C-N-H) (1530 cm^{-1}) of amic acid, which is an intermediate of imidization reaction, was not observed, it also indicated that imidization reaction was completed. Absorption peaks at 1502 cm^{-1} and 1573 cm^{-1} caused by vibration of the phenylenediamine benzene ring skeleton v(C-C) were observed.[41,42] Asymmetric stretching vibration peaks and symmetric stretching vibration peaks of the sulfonic acid group were observed at 1249 cm^{-1} and 1193 cm^{-1}, respectively.[43] Asymmetric stretching vibration peaks of sulfonic acid groups after proton ionization were observed at 1024 cm^{-1}.[44]

As a result of the FT-IR ATR measurement, it was found that imidization proceeded sufficiently since the typical peak of amide, amide δ (N-H) and amic acid δ (C-N-H) were not observed. Also, no by-product or unreacted product peaks were observed.

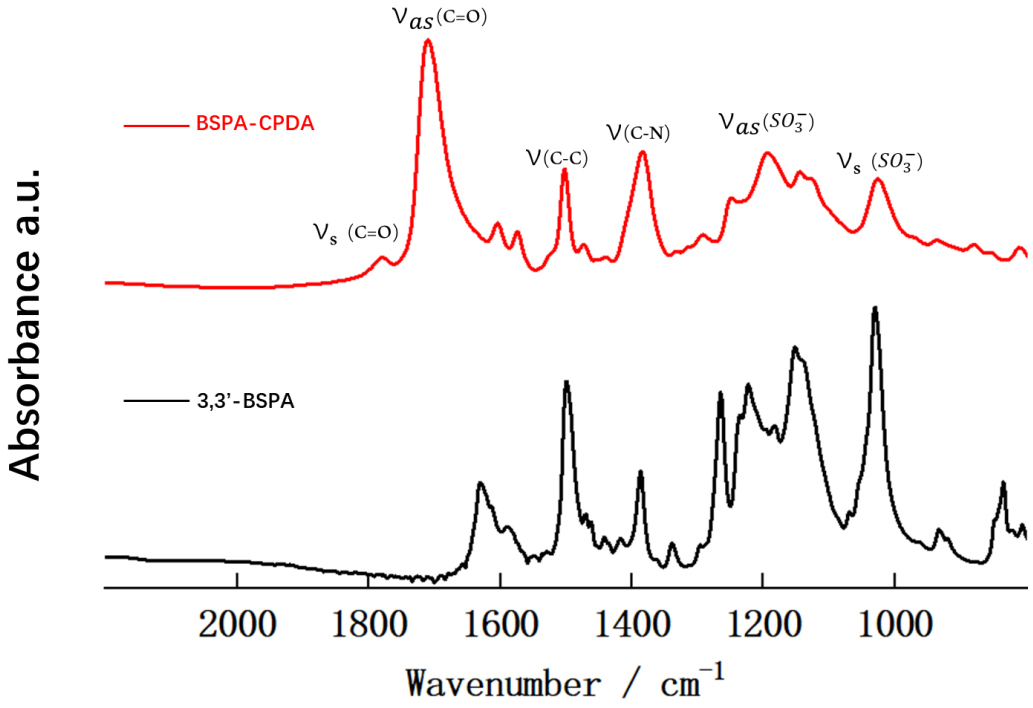

Figure 3-8. FTIR ATR spectra for 3,3'-BSPA and BSPA-CPDA.

3.3.1.3 GPC study

In order to identify the molecular weight of the polymer, measurement by GPC was performed. Figure 3-9 shows the GPC chromatogram of BSPA-CPDA. The calculation results of molecular weight were shown in Table 2-1. As a result of calculation using a calibration curve, the weight average molecular weight (Mw) of BSPA-CPDA was 9300. Since no other prominent peaks were observed, the polymer was considered to have sufficiently polymerized.

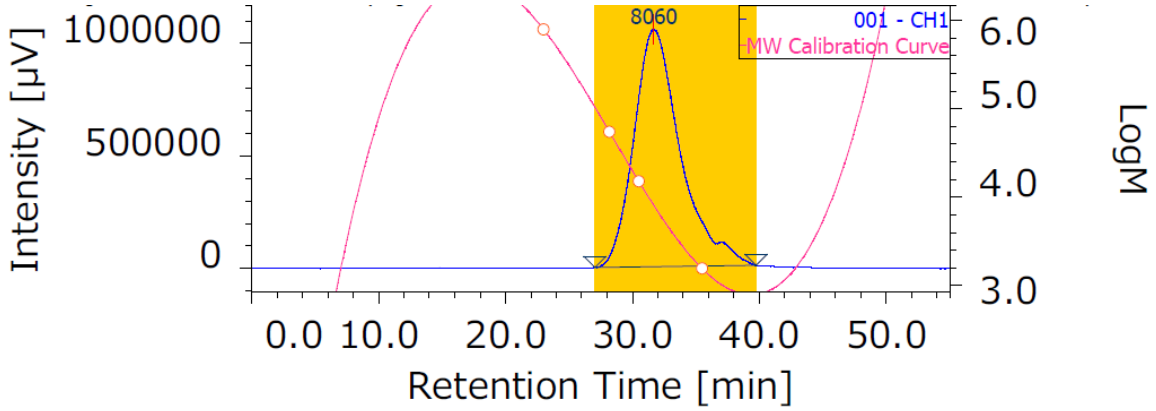

Figure 3-9.GPC spectra for BSPA-CPDA.

Table 3-1. Molecular weight of BSPA-CPDA.

	Baseline range	M_w	M_n	M_w/M_n
BSPA-CPDA	27.02 - 39.73	9365	4319	2.17

3.3.2 Water uptake

Because water works as a carrier to facilitate the transport of protons in thin films, water uptake has a significant impact on the conductivity of proton exchange membranes. Figure 3-10 shows the RH-dependent water uptake of BSPA-CPDA thin film. For comparison, water uptake data for ASPI-2 (consisting of pyromellitic dianhydride and BSPA) and ASSPI (consisting of 1,2,4,5-cyclohexanetetracarboxylic dianhydride and BSPA) thin films with comparable molecular weights are also plotted in the same figure.[31,36] The adsorption isotherm of water molecules showed a similar tendency to the adsorption isotherm of non-porous multimolecular adsorption. This was considered to be a change in the type of adsorbed water around the sulfonic acid groups.[45,46] The adsorption behaviors of BSPA-CPDA, ASPI-2 and ASSPI thin films with respect to RH were similar. The water uptake value gradually increased with increasing RH. It can be seen that the water uptake value of all thin films was the same under low humidity, but BSPA-CPDA thin film showed higher water uptake value ($\lambda = 16$) than ASSPI ($\lambda = 13$) and ASPI-2 ($\lambda = 14$) thin films at 95% RH.

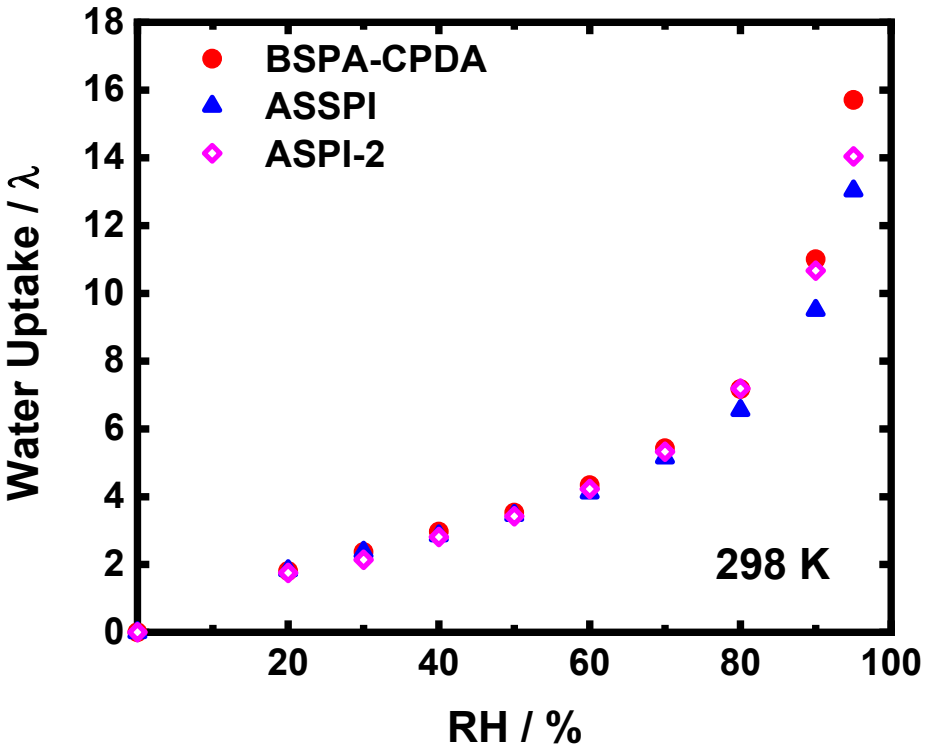

Figure 3-10. Water uptake of BSPA-CPDA, ASPI-2[28] and ASSPI[33] thin films as a function of RH at 298K.

3.3.3 In situ FTIR

In order to evaluate the dissociation behavior of sulfonic acid protons, the RH-controlled in situ FTIR measurements were performed on BSAP-CPDA thin film. The spectra of BSPA-CPDA thin film under humidification are shown in Figure 3-11(a). The broad absorption band around 3420 cm^{-1} is attributed to the OH stretching vibration mode of water molecules under humidification.[44,47] The absorbance of this band increased with increasing the RH, indicating that water molecules were adsorbed on the thin film under humidified conditions. Specifically, at 0% RH the absorption band of water molecules could not be observed, meanwhile, the band observed at 902 cm^{-1} could be attributed to the stretching vibration mode of the S-O bond in protonated sulfonic acid group.[48] This band at 902 cm^{-1} was completely disappeared with increasing RH.

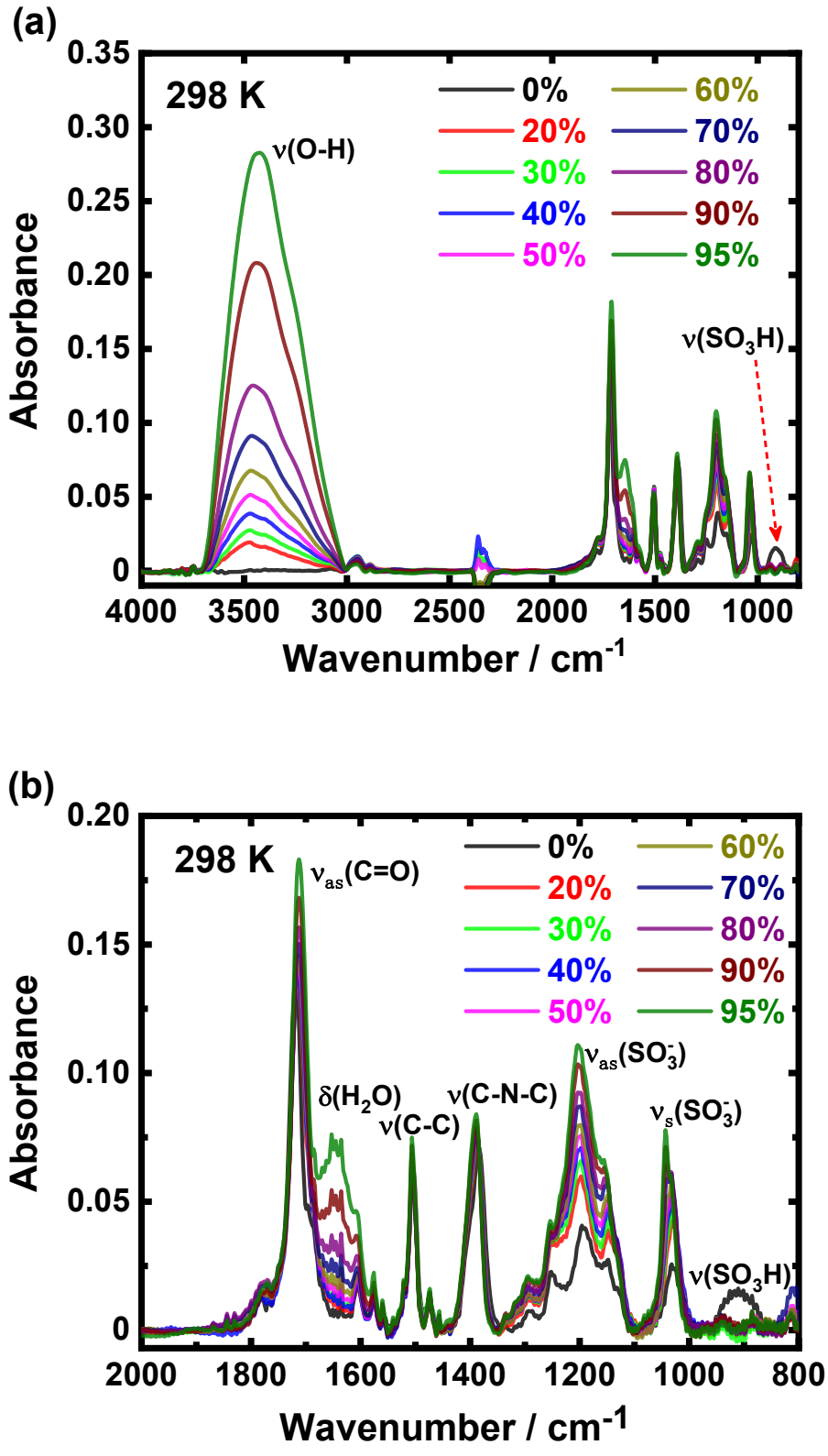

Figure 3-11. RH-dependent FTIR spectra of BSPA-CPDA thin film (a) in the range of 4000-800 cm^{-1}; (b) in the range of 2000-800 cm^{-1}.

Subsequently, the molecular states of the sulfonic acid group of BSPA-CPDA thin film were analyzed.

As shown in Figure 3-11(b), the absorption band attributed to the O=S=O symmetric stretching vibration (v_s (S=O)) of deprotonated sulfonic acid was observed at 1030-1040 cm^{-1}. We note that some sulfonic acid groups are deprotonated under the 0% RH. The peak area of v_s (S=O) under different RH conditions was recorded as $S_x(SO_3^-)$, and the peak area of v_s (S=O) at 0% RH was recorded as $S_0(SO_3^-)$. The proton dissociation (PD / %) rate of the sulfonic acid group under each humidity condition is defined by the following equation:

$$PD(\%) = \frac{\left(S_{x(so_3^-)} - S_{0(so_3^-)}\right)}{\left(S_{95(so_3^-)} - S_{0(so_3^-)}\right)} \times 100\% \quad (3\text{-}4)$$

The obtained PD value and water uptake value are plotted as a function of RH and the results are shown in Figure 3-12. Below 70% RH, the PD value increased to 90% rapidly with small amount of water uptake. This indicates that even less water adsorption can cause rapid deprotonation of sulfonic acid groups. When RH further increasing from 70% to 95%, the PD value only increased 10% and saturated. The sulfonic acid groups are considered to be completely deprotonated.

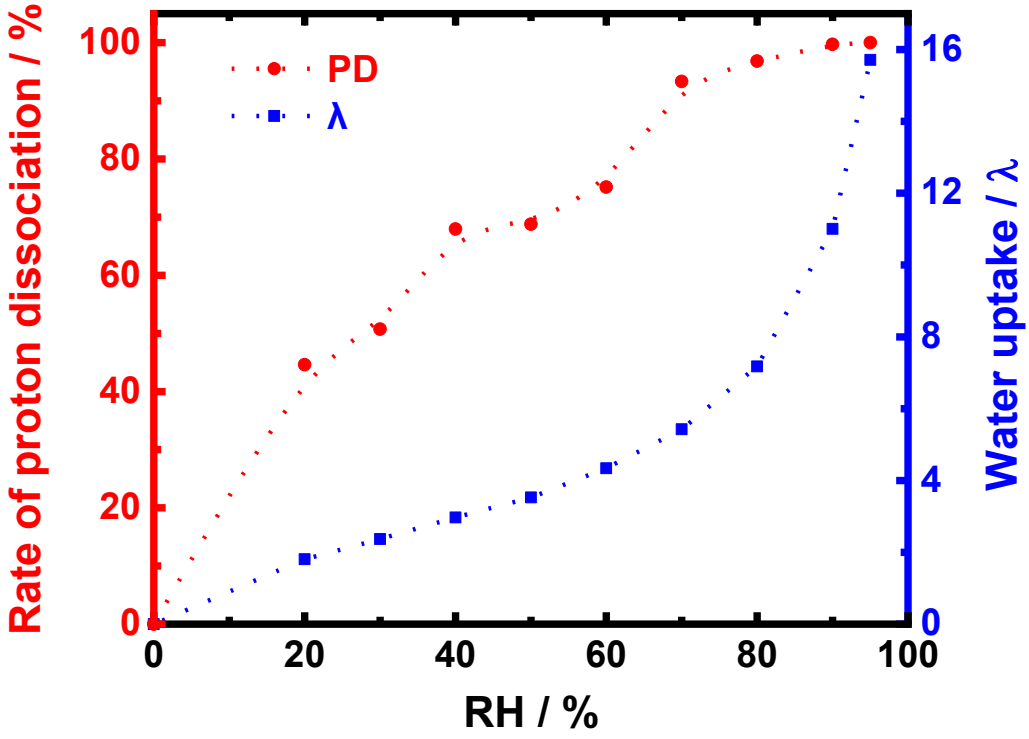

Figure 3-12. RH-dependent rate of proton dissociation from O=S=O symmetric stretching of SO_3^- (1030-1040 cm^{-1}) and water uptake for BSPA-CPDA thin film.

The change of PD behavior is related to the type of water molecules adsorbed around the sulfonic

acid groups. Zhao et al. reported that the adsorbed water molecules around sulfonic acid groups in Nafion membrane can be divided into two types: one type is caused as forming a primary hydration shell by strong binding water molecules with acid groups under the λ region less than 4; another type is caused by the hydration of more excess water molecules under the λ region more than 4.[49] In our study, the slope of the water uptake quickly changed around λ=5 as 70% RH, indicating the change of water adsorption from the strongly bound water with the sulfonic acid groups to excessive bulk water.

The O−H stretching region can be deconvolution into four peaks by Gaussian deconvolution method.[50,51,52] As shown in Figure 3-13(a), the peak representing the hydronium ion (H_3O^+) appears at 3146 cm^{-1},[50,53] the peak corresponding to the water hydrogen-bonded (H-bonded) to the sulfonic acid group appears at 3252 cm^{-1},[51,54] the peak representing water H-bonded to other water molecules appears at 3413 cm^{-1},[52,55] the peak corresponding to the non-H-bonded water appears at 3558 cm^{-1}.[50,56] The water molecules H-bonded to sulfonic acid group is assigned as “bounded water” and the water molecules H-bonded to other water molecules is assigned as the “bulk water”.

The integrated absorbance of each component *i* is expressed as A_i. The fraction fi of each band area A_i is calculated as follows

$$f_i = A_i / \sum_j^4 A_j \quad (3\text{-}5)$$

the λ_i represents each water component per sulfonic acid group is calculated as follows

$$\lambda_i = \lambda_{total} \times f_i \quad (3\text{-}6)$$

Where the λ_{total} is the water uptake value determined by QCM measurements. The Figure 3-13(b) shows the results of λ_i as a function of RH. Both water molecules H-bonded to other water molecules ($\lambda_{(H_2O)}$) and water molecules H-bonded to sulfonic acid group ($\lambda_{(SO_3^-)}$)gradually increase with increasing humidity. When the RH is higher than 70%, $\lambda_{(H_2O)}$ begins to increase rapidly but $\lambda_{(SO_3^-)}$ remains almost unchanged. This shows that most of the water molecules adsorbed after 70% RH are bulk water, which is consistent with the results discussed above about the PD and water uptake value.

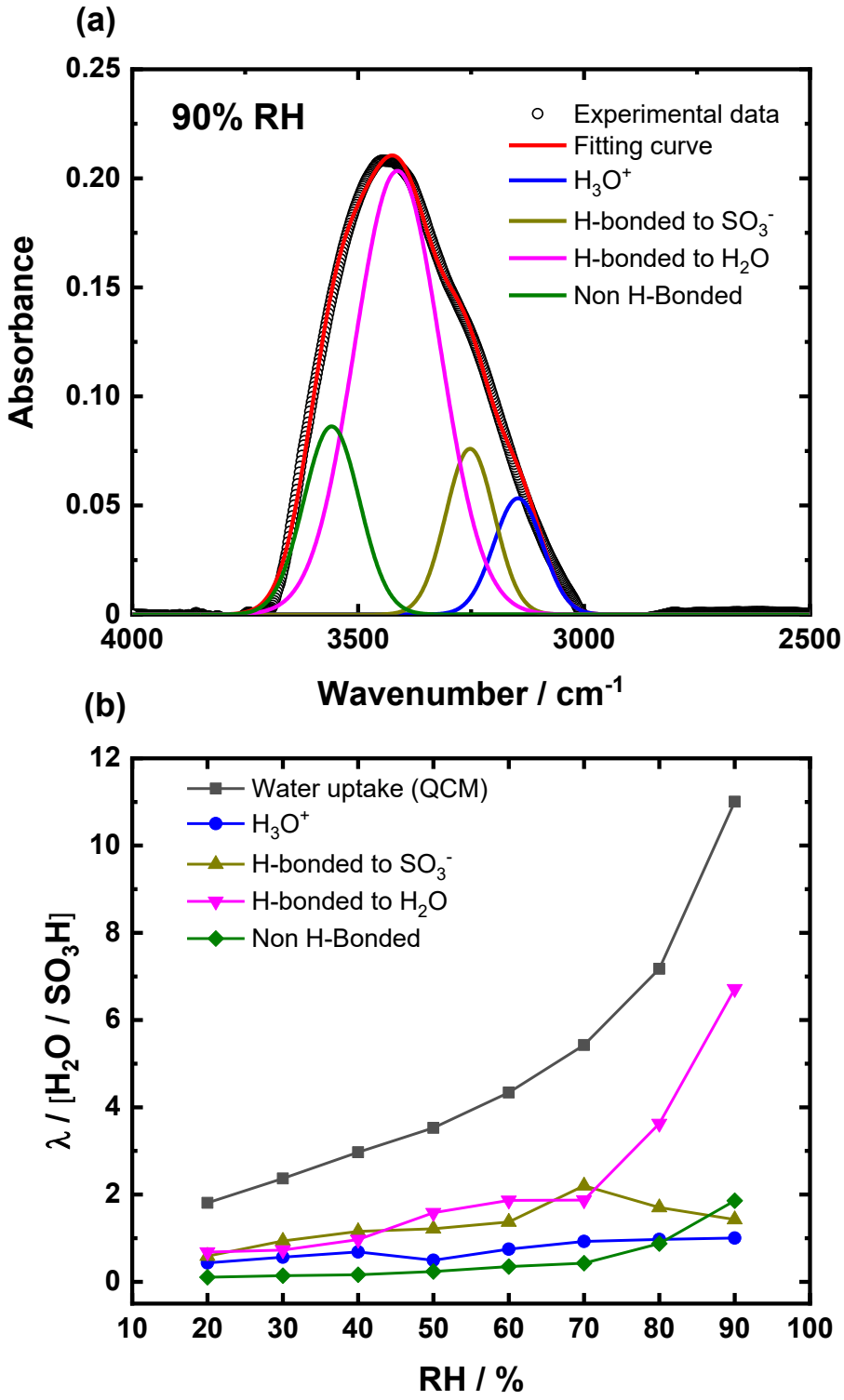

Figure 3-13. (a) Gaussian deconvolution of the O−H stretching region of in situ FTIR spectrum of BSPA-CPDA at 90% RH, 298 K; (b) water uptake values of 4 types of water in BSPA-CPDA thin film as a function of RH.

3.3.4 In situ GIXRS

GIXRS is a powerful tool for detecting molecular packings and molecular orderings in molecular organized thin films.[50,51] RH-dependent in situ GIXRS measurements on the BSPA-CPDA thin film were carried out to examine the effect of the oligomeric semi-alicyclic main chain on the lyotropic ordered structure. The 2D scattering images are shown in Figures 3-14(a-d) and 1D GIXRS profiles in the in-plane (IP) and out-of-plane (OP) directions are shown in Figures 3-14(e, f). One scattering peak in the OP direction was observed, indicating that the ordered structure was formed perpendicular to the substrate surface. According to our previous reports, the hydrophobic backbone of polyimides aligned along the IP direction parallel to the substrate, meanwhile the hydrophilic side chain with sulfonic acid groups oriented in the OP direction to form a lamellar structure by lyotropic LC property.[8,35,36] In the present study, as the RH increasing, the intensity of the scattering peak increased in the OP direction, and the peak position gradually moved toward the small angle. This trend of structural change is the same as that seen in previous reports, indicating lamellar expansion and degree of molecular ordering were enhanced by the lyotropic LC property. In the IP profiles, RH-dependent scattering peaks were observed in the small-angle region. This scattering peak can be attributed to the origin from the broad OP scattering as shown in Figures 33-14(b-d). These results indicate that as the RH increases, the loosely packed lamellar was organized and expanded to the OP direction with increasing the degree of structural order.

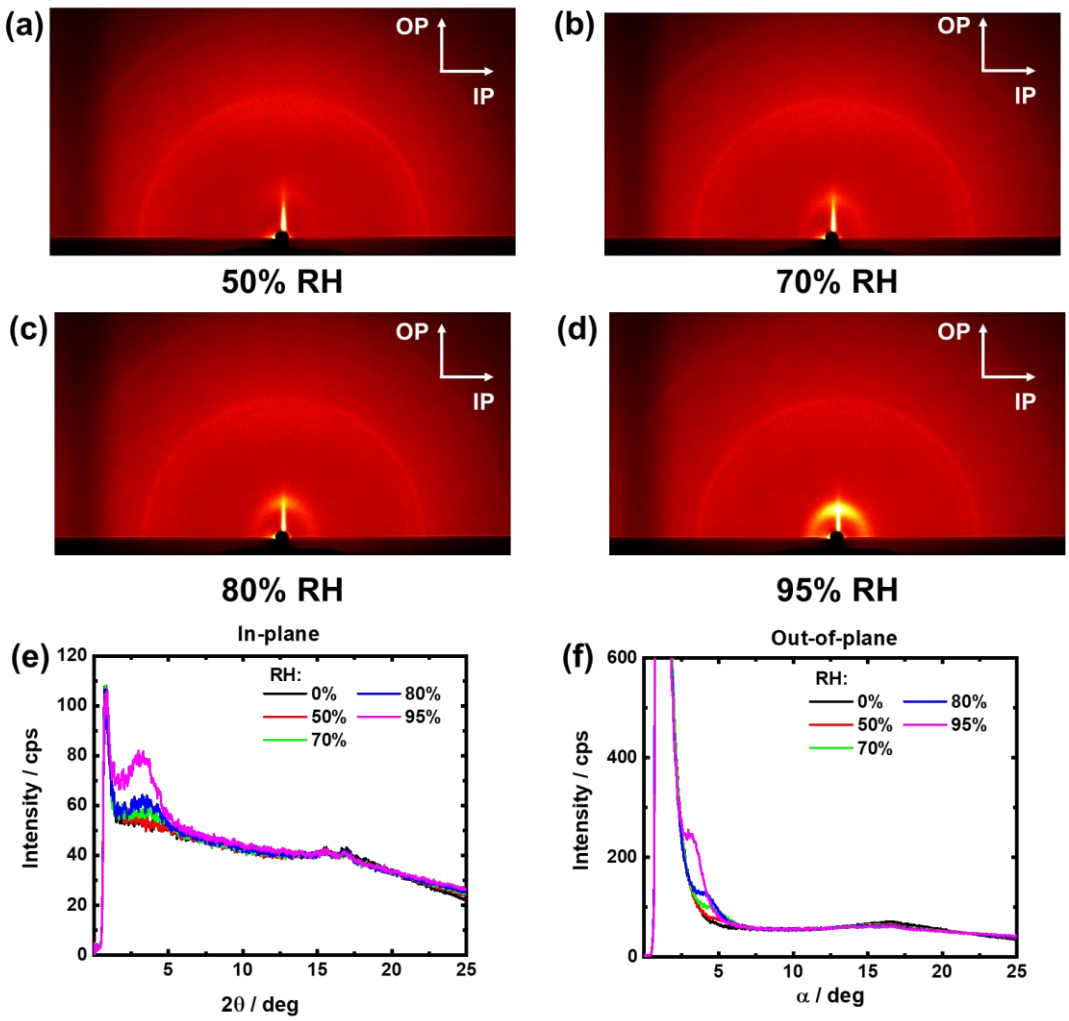

Figure 3-14. GIXRS measurement results of BSPA-CPDA thin film. A, b, c and d show 2D GIXRS patterns at 50% RH, 70% RH, 80% RH and 95% RH, respectively. RH-dependent 1D profiles in the in-plane and out-of-plane directions of the thin film are shown in e and f, respectively. Those scattering peaks at 2θ=15.5° and 16.8° were originated from the Lumirror window of the humidity-controlled cell.

Ando et al. have investigated the backbone aggregation of polyimides with both aromatic and semialiphatic structures through grazing-incidence wide-angle X-ray scattering (GIWAXS) measurement.[15] The fully aromatic polyimide with the rod-like molecular structure and high planarity forms smectic LC ordered structure like main-chain LC polymers. Our previous fully aromatic ASPI thin films with alkyl-sulfonated side chains also showed similar in-plane and out-of-plane scatterings, which could be explained by the periodic unit length and a ch-pack aggregation of the polyimide backbone, respectively. In the case of ASSPI, no scattering representing the periodic unit length was observed in the in-plane direction and the scattering represents ch-pack aggregation was observed in the out-of-plane

direction. However, only one isotropic (arc) scattering was observed in the GIXRS results of low-molecular-weight ASSPI, indicating that even under humidified conditions, low-molecular-weight ASSPI only exhibits a weak randomly oriented lamellar structure due to the semi-alicyclic main chain. In the present study, the GIXRS results are similar to the ASSPI case. A weak RH-independent scattering was observed at α = 16.5° representing the ch-pack aggregation of BSPA-CPDA backbone in the out-of-plane direction. Although the ch-pack interaction of the present oligomer reduces by the substitution of semi-alicyclic CPDA, we could observe the formation of a distinct organized lamellar structure in the out-of-plane direction under high RH conditions.

To understand the reason for observing the lamellar structure at oligomeric BSPA-CPDA, we tried to investigate the structural model. For comparison, oligomeric ASSPI units which only shows weak lamellar structure was also considered. Figure 3-15 depicts the optimized oligomeric structures of 5 repeating units for BSPA-CPDA and previous ASSPI by DFT calculation. The main chain of BSPA-CPDA units showed higher rigidity than that of ASSPI units. Therefore, even low molecular weight, BSPA-CPDA thin film with more rigid backbone can exhibit a well-ordered lamellar structure by strong lyotropic LC property.

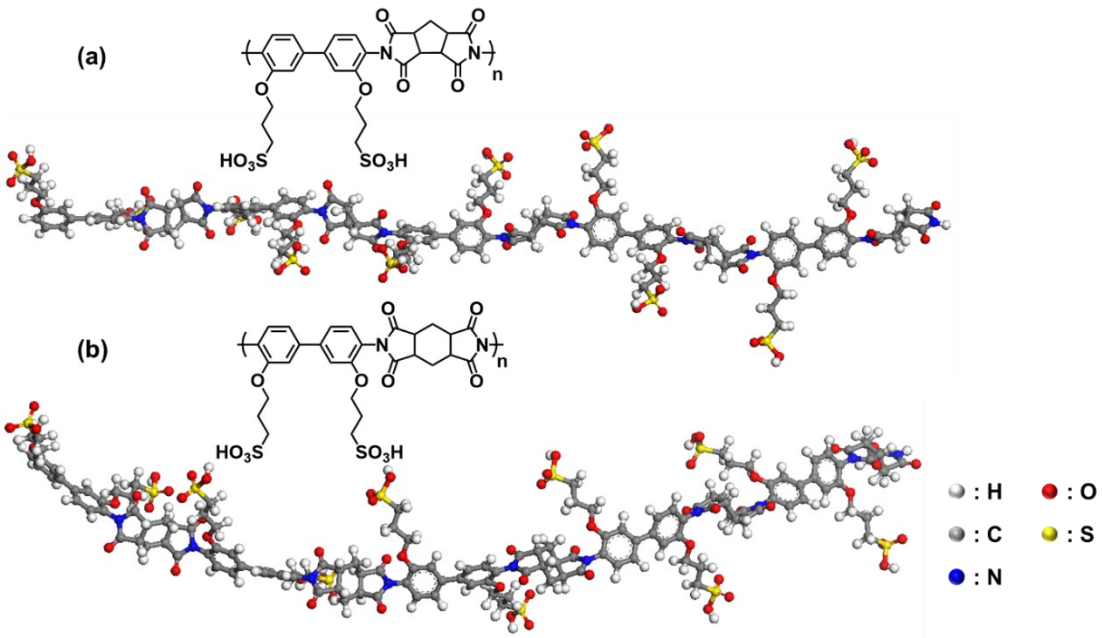

Figure 3-15. Optimized structures of (a) 5 repeating units of BSPA-CPDA with rigid backbone and (b) 5 repeating units of ASSPI with bending backbone.

The layer distance (*d*) of lamellar structure under different humidity conditions can be calculated by

employing the following equation :

$$d = \frac{0.1542}{2sin\theta} \quad (3\text{-}7)$$

Where θ is the angle of scattering peak appeared at different RH and 0.1542 (nm) is the wavelength of the X-rays generated through Cu Kα radiation. Figure 3-16 shows the calculated *d* value of BSPA-CPDA thin film as a function of water uptake. For comparison, water uptake of other two reported ASPI thin films are shown. The layer distance of fully aromatic ASPI-2 thin film changes linearly, showing a maximum d value of 3.0 nm at λ=14. The layer distance of semi-alicyclic sulfonated oligo-BSPA-CPDA and ASSPI thin films varied nonlinearly with a relatively lower maximum d value of 2.7 nm at λ = 16. Non-linear expansion of interlamellar distance with respect to the number of water molecules contained has not been observed in fully aromatic polyimide. This is considered to be a feature of thin films having a semi-alicyclic backbone though the mechanism is not yet determined. In addition, in the fully aromatic polyimide thin films, the length of the side chain determined the interlamellar distance, but it is clear that this tendency is different in the semi-alicyclic oligoimide thin film having an alkyl chain of the same length in the side chain. Since the semi-alicyclic oligoimide thin film has a small interlamellar distance, the proton concentration per unit volume is higher than that of the fully aromatic polyimide thin films, so that high proton conductivity can be expected.

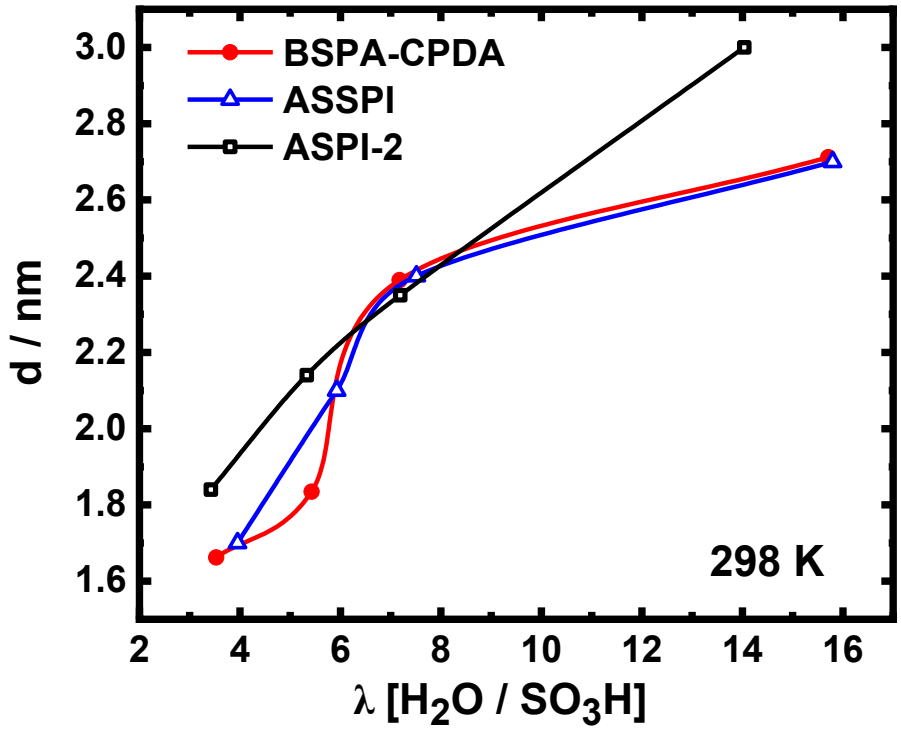

Figure 3-16. Humidity-dependent layer distance of BSPA-CPDA, ASSPI and ASPI-2 thin films.

3.3.5 Proton Conductivity

The proton conductivity for the BSPA-CPDA thin film is shown in Figure 3-17(a) as a function of humidity at 298 K. The proton conductivity increased with increasing RH, which could be observed as typical proton conducting polymers. The maximum proton conductivity reached 0.2 S cm^{-1} at 95% RH. The achieved value is the highest one among the reported sulfonated polyimide thin films with lower molecular weight. We note that these ASPI thin films show molecular weight dependence of the proton conductivity. Therefore we compared the proton conductivity of thin films with similar low molecular weight. Figure 3-17(b) shows the proton conductivity of BSPA-CPDA, ASPI-2 and ASSPI thin films as a function of the water uptake value (λ) per sulfonic acid group. The increasing in λ value in the case of low RH significantly increased proton conductivity of all thin films. In the same water uptake, the BAPA-CPDA thin film showed the highest proton conductivity. This highest proton conductivity can be achieved by the organized lamellar structure with relatively rigid backbone in semi-alicyclic oligoimide because of the strong lyotropic LC property.

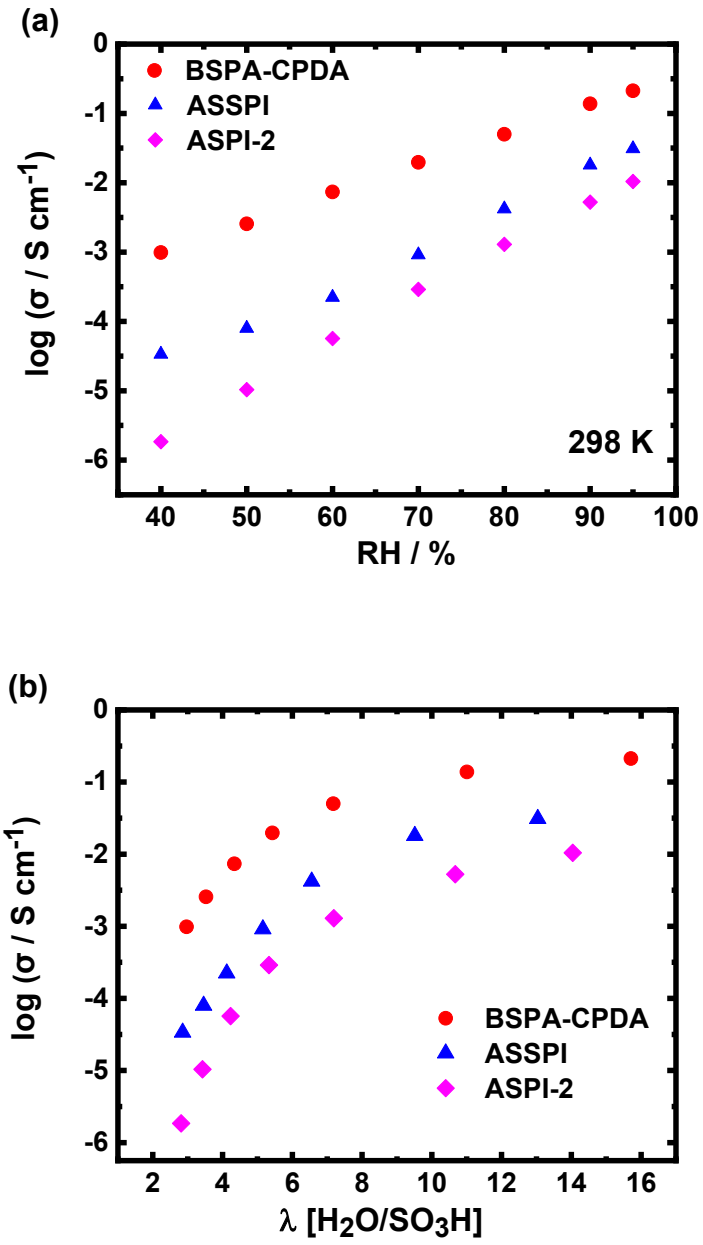

Figure 3-17. (a) Proton conductivity of BSPA-CPDA, ASSPI and ASPI-2 thin films with comparable molecular weight as a function of RH at 298 K; (b) Proton conductivity of BSPA-CPDA, ASPI-2 and ASSPI thin films with comparable molecular weight as a function of water up take (λ) at 298 K.

3.3.6 Comparison with other ASPIs

Table 1 summarizes the structural features, molecular weight, liquid crystal features, and proton conductivity of the BSPA-CPDA and reported ASPI thin films.[31,35,36] The ASPI-1[31] (consisting of 1,4,5,8-

naphthalenetetracarboxylic dianhydride and BSPA, Figure S4c) and ASPI-2 have fully aromatic backbone, and the ASSPI[36] and the present BSPA-CPDA possesses semi-alicyclic backbone. In all the alkyl sulfonated polyimide thin films, a lyotropic lamellar ordering with phase separation of the hydrophobic main chain and hydrophilic side chain layers is observed under humidification. Moreover, the fully aromatic ASPI-1 and ASPI-2 thin films exhibit smectic ordering within the lamellar layer because of the lyotropic LC properties by the rigid linear main chain.[31,35] Reportedly, the degree of molecular ordering deteriorates when the molecular weight becomes small.[31] On the other hand, the previous ASSPI thin film with a semi-alicyclic backbone does not exhibit scattering corresponding to the main chain smectic order in the intra-lamellar plane.[36] This indicates that the alicyclic structure weakens the aggregate of the main chains, and the positional order of the main chains within the lamellar layer is lost (nematic-like structure). Therefore, the scattering of the lyotropic lamellar structures is also weak and less ordered compared to the fully aromatic polyimides. The lamellar ordering decreased considerably in the low-molecular-weight ASSPI (M_w = 25,000).

In the present BSPA-CPDA with a semi-alicyclic backbone, the scattering corresponding to the lyotropic lamellar organized structure was observed, but no positional order of the main chains was observed. Even for the oligomer level of the molecular weight (M_w = 9,300), BSPA-CPDA obviously exhibits the lyotropic lamellar scattering, indicating highly molecular ordering compared to ASSPI. Comparing the two semi-alicyclic polymers, the present BSPA-CPDA adopts a more linear conformation according to the DFT results (Figure 5). Thereby, BSPA-CPDA with a more linear main chain exhibits a higher-ordered lamellar structure than that of ASSPI. Proton conductivity decreased greatly with decreasing molecular weight in previous ASPI and ASSPI. However, the BSPA-CPDA oligomer exhibits high proton conductivity comparable to ASPIs with higher molecular weight. The ordered lamellar structure driven by the linear conformation of semi-alicyclic and rigid backbone structure can enhance the proton conductivity. This is the first demonstration of the high proton conductivity by the lamellar structure with semi-alicyclic backbone in such a low molecular weight oligoimide thin film.

Table 3-2. Structural features, molecular weight, liquid crystal features, and proton conductivities of the present BSPA-CPDA and reported ASPI thin films with thickness of ~500 nm.

Materials	Main chain backbone	Main chain conformation	Molecular weight (M_w)	Lyotropic LC Structure	Main chain LC structure	σ^a (S cm^{-1})
BSPA-CPDA	Semi-alicyclic	Linear	9300	Lamellar	Nematic-like	0.20
ASPI-1[35]	Aromatic	Linear	490000	Lamellar	Smectic	0.18
ASPI-2[31]	Aromatic	Linear	13000	Weak lamellar	/	0.01
			260000	Lamellar	Smectic	0.26
ASSPI[36]	Semi-alicyclic	Nonlinear	25000	Weak lamellar	/	0.03
			40000	Lamellar	Nematic-like	0.15

3.4 Conclusion

It had not been discovered that sulfonated polyimide thin films with semi-alicyclic backbone in the main chain forms a lamellar structure due to the weak rigidity of the main chain and low molecular weight. In this study, we have investigated whether lyotropic LC property can drive a lamellar structure by an improved rigidity of the alicyclic main chain even with a low molecular weight. To investigate this hypothesis, a novel sulfonated semi-alicyclic oligoimide, BSPA-CPDA, with cyclopentane backbone was newly synthesized, employing a more rigid main chain than previously reported. The water uptake of BSPA-CPDA thin film showed similar trend with the other reported ASPIs; the results of in situ FTIR showed that when λ=5 at 70% RH, the adsorbed water around the sulfonic acid group changes from bound water to bulk water. The GIXRS results of BSPA-CPDA thin film showed that the scattering peak of the loosely packed lamellar structure driven by lyotropic LC property was observed under high humidity conditions, indicating a change from disordered to ordered aggregated structure. As the humidity increases, the layered structure was strengthened and the distance of lamellar was enlarged. The proton conductivity of the BSPA-CPDA thin film increased with increasing the humidity and achieved a value of 0.2 S cm^{-1} at 298 K and 95% RH. Compared with the other reported ASPIs with relatively lower molecular weight, BSPA-CPDA thin film has the highest proton conductivity value among them. This is attributed to

the formation of the lamellar structure to facilitate proton transport channels driven by the nature of lyotropic LC property. We concluded that sulfonated oilgoimide thin films with more rigid alicyclic backbone in the main chain can form organized lamellar structure due to the strong lyotropic LC property.

References

1. Hsu, W. Y. & Gierke, T. D. Ion transport and clustering in nafion perfluorinated membranes. J. Memb. Sci. 13, 307–326 (1983).
2. Kreuer, K. D. On the development of proton conducting polymer membranes for hydrogen and methanol fuel cells. J. Memb. Sci. 185, 29–39 (2001).
3. Hickner, M. A., Ghassemi, H., Kim, Y. S., Einsla, B. R. & McGrath, J. E. Alternative polymer systems for proton exchange membranes (PEMs). Chem. Rev. 104, 4587–4611 (2004).
4. Rikukawa, M. & Sanui, K. Proton-conducting polymer electrolyte membranes based on hydrocarbon polymers. Prog. Polym. Sci. 25, 1463–1502 (2000).
5. Yang, Y. & Holdcroft, S. Synthetic strategies for controlling the morphology of proton conducting polymer membranes. Fuel Cells 5, 171–186 (2005).
6. Chang, Y. et al. Aromatic Ionomers with Highly Acidic Sulfonate Groups: Acidity, Hydration, and Proton Conductivity. Macromolecules 44, 8458–8469 (2011).
7. Allen, F. I. et al. Morphology of hydrated as-cast Nafion revealed through cryo electron tomography. ACS Macro Lett. 4, 1–5 (2015).
8. Nagao, Y. Proton-Conductivity Enhancement in Polymer Thin Films. Langmuir 33, 12547–12558 (2017).
9. Ruokolainen, J. et al. Switching supramolecular polymeric materials with multiple length scales. Science (80-.). 280, 557–560 (1998).
10. Soberats, B. et al. Ionic Switch Induced by a Rectangular-Hexagonal Phase Transition in Benzenammonium Columnar Liquid Crystals. J. Am. Chem. Soc. 137, 13212–13215 (2015).
11. Yoshio, M., Mukai, T., Ohno, H. & Kato, T. One-Dimensional Ion Transport in Self-Organized Columnar Ionic Liquids. J. Am. Chem. Soc. 126, 994–995 (2004).
12. Kato, T. et al. Transport of ions and electrons in nanostructured liquid crystals. Nat. Rev. Mater. 2, (2017).
13. Tonozuka, I., Yoshida, M., Kaneko, K., Takeoka, Y. & Rikukawa, M. Considerations of polymerization method and molecular weight for proton-conducting poly(p-phenylene) derivatives. Polymer (Guildf). 52, 6020–6028 (2011).
14. Sato, T. et al. High proton conductivity in the molecular interlayer of a polymer nanosheet multilayer film. Langmuir 31, 5174–5180 (2015).
15. Wakita, J., Jin, S., Shin, T. J., Ree, M. & Ando, S. Analysis of molecular aggregation structures of fully aromatic and semialiphatic polyimide films with synchrotron grazing incidence wide-angle x-ray scattering. Macromolecules 43, 1930–1941 (2010).
16. Krishnan, K., Iwatsuki, H., Hara, M., Nagano, S. & Nagao, Y. Proton conductivity enhancement in oriented, sulfonated polyimide thin films. J. Mater. Chem. A 2, 6895–6903 (2014).
17. Goto, R. et al. Preparation and structural characterization of shear-aligned films in a high proton conductive alkyl-sulfonated polyimide with lyotropic liquid crystallinity. Mol. Cryst. Liq. Cryst. 0, 1–10 (2021).
18. Meyer, G. et al. Degradation of sulfonated polyimide membranes in fuel cell conditions. J. Power Sources 157, 293–301 (2006).
19. Chen, K., Hu, Z., Endo, N., Higa, M. & Okamoto, K. Sulfonated multiblock copolynaphthalimides for

polymer electrolyte fuel cell application. Polymer (Guildf). 52, 2255–2262 (2011).
20. Li, N., Cui, Z., Zhang, S., Li, S. & Zhang, F. Preparation and evaluation of a proton exchange membrane based on oxidation and water stable sulfonated polyimides. J. Power Sources 172, 511–519 (2007).
21. Park, M. J. & Balsara, N. P. Anisotropie proton conduction in aligned block copolymer electrolyte membranes at equilibrium with humid air. Macromolecules 43, 292–298 (2010).
22. Chen, Y. et al. Enhancement of anhydrous proton transport by supramolecular nanochannels in comb polymers. Nat. Chem. 2, 503–508 (2010).
23. Trigg, E. B. et al. Self-assembled highly ordered acid layers in precisely sulfonated polyethylene produce efficient proton transport. Nat. Mater. 17, 725–731 (2018).
24. Tamura, T. & Kawakami, H. Aligned electrospun nanofiber composite membranes for fuel cell electrolytes. Nano Lett. 10, 1324–1328 (2010).
25. Mauritz, K. A. & Moore, R. B. State of understanding of Nafion. Chem. Rev. 104, 4535–4585 (2004).
26. Kusoglu, A. & Weber, A. Z. New Insights into Perfluorinated Sulfonic-Acid Ionomers. Chem. Rev. 117, 987–1104 (2017).
27. Karan, K. Interesting Facets of Surface, Interfacial, and Bulk Characteristics of Perfluorinated Ionomer Films. Langmuir 35, 13489–13520 (2019).
28. Liu, X. et al. Magnetic field alignment of stable proton-conducting channels in an electrolyte membrane. Nat. Commun. 10, (2019).
29. Nagao, Y. Progress on highly proton-conductive polymer thin films with organized structure and molecularly oriented structure. Sci. Technol. Adv. Mater. 21, 79–91 (2020).
30. KRISHNAN, K. et al. Influence of Confined Polymer Structure on Proton Transport Property in Sulfonated Polyimide Thin Films. Electrochemistry 82, 865–869 (2014).
31. Krishnan, K., Iwatsuki, H., Hara, M., Nagano, S. & Nagao, Y. Influence of Molecular Weight on Molecular Ordering and Proton Transport in Organized Sulfonated Polyimide Thin Films. J. Phys. Chem. C 119, 21767–21774 (2015).
32. NAGAO, Y., KRISHNAN, K., GOTO, R., HARA, M. & NAGANO, S. Effect of Casting Solvent on Interfacial Molecular Structure and Proton Transport Characteristics of Sulfonated Polyimide Thin Films. Anal. Sci. 33, 35–39 (2017).
33. Nagao, Y. et al. Effect of Molecular Orientation to Proton Conductivity in Sulfonated Polyimides with bent backbones. Mol. Cryst. Liq. Cryst. 686, 84–91 (2019).
34. Nagao, Y. et al. Introducing planar hydrophobic groups into an alkyl-sulfonated rigid polyimide and how this affects morphology and proton conductivity. Electrochim. Acta 300, 333–340 (2019).
35. Ono, Y. et al. High Proton Conduction of Organized Sulfonated Polyimide Thin Films with Planar and Bent Backbones. Macromolecules 51, 3351–3359 (2018).
36. Takakura, K. et al. Lyotropic ordering for high proton conductivity in sulfonated semialiphatic polyimide thin films. Polym. J. 51, 31–39 (2019).
37. Yin, Y. et al. Water stability of sulfonated polyimide membranes. Macromolecules 39, 1189–1198 (2006).
38. Sung, J., Kim, D., Whang, C. N., Oh-E, M. & Yokoyama, H. Sum-frequency vibrational spectroscopic study of polyimide surfaces made by spin coating and ionized cluster beam deposition. J. Phys. Chem. B 108, 10991–10996 (2004).
39. Sakamoto, K. et al. Determination of molecular orientation of very thin rubbed and unrubbed polyimide films. J. Appl. Phys. 80, 431–439 (1996).
40. Shin, T. J., Lee, B., Youn, H. S., Lee, K. B. & Ree, M. Time-resolved synchrotron X-ray diffraction and

infrared spectroscopic studies of imidization and structural evolution in a microscaled film of PMDA-3,4′-ODA poly(amic acid). Langmuir 17, 7842–7850 (2001).
41. Miyatake, K., Yasuda, T., Michiko, H., Nanasawa, M. & Watanabe, M. Synthesis and properties of a polyimide containing pendant sulfophenoxypropoxy groups. J. Polym. Sci. Part A Polym. Chem. 46, 157–163 (2007).
42. Hietpas, G. D., Sands, J. M. & Allara, D. L. Formation of a molecularly reconstructed surface layer during unidirectional rubbing of polyimide films. Macromolecules 31, 3374–3378 (1998).
43. Fang, J. et al. Novel sulfonated polyimides as polyelectrolytes for fuel cell application: 1. Synthesis, proton conductivity, and water stability of polyimides from 4,4′-diaminodiphenyl ether-2,2′-disulfonic acid. Macromolecules 35, 9022–9028 (2002).
44. Buzzoni, R., Bordiga, S., Ricchiardi, G., Spoto, G. & Zecchina, A. Interaction of H2O, CH3OH, (CH3)2O, CH3CN, and Pyridine with the Superacid Perfluorosulfonic Membrane Nafion: An IR and Raman Study. J. Phys. Chem. 99, 11937–11951 (1995).
45. Watari, T. et al. Water vapor sorption and diffusion properties of sulfonated polyimide membranes. J. Memb. Sci. 219, 137–147 (2003).
46. Detallante, V. et al. Kinetics of water vapor sorption in sulfonated polyimide membranes. Desalination 148, 333–339 (2002).
47. Hunger, B., Matysik, S., Heuchel, M. & Einicke, W.-D. Adsorption of Methanol on ZSM-5 Zeolites. Langmuir 13, 6249–6254 (1997).
48. Ostrowska, J. & Narebska, A. Infrared study of hydration and association of functional groups in a perfluorinated Nafion membrane, Part 1. Colloid Polym. Sci. 261, 93–98 (1983).
49. Zhao, Q., Majsztrik, P. & Benziger, J. Diffusion and interfacial transport of water in Nafion. J. Phys. Chem. B 115, 2717–2727 (2011).
50. Ferrari, M. C., Catalano, J., Baschetti, M. G., De Angelis, M. G. & Sarti, G. C. FTIR-ATR study of water distribution in a short-side-chain PFSI membrane. Macromolecules 45, 1901–1912 (2012).
51. Hofmann, D. W. M. et al. Investigation of water structure in Nafion membranes by infrared spectroscopy and molecular dynamics simulation. J. Phys. Chem. B 113, 632–639 (2009).
52. Barique, M. A., Tsuchida, E., Ohira, A. & Tashiro, K. Effect of Elevated Temperatures on the States of Water and Their Correlation with the Proton Conductivity of Nafion. ACS Omega 3, 349–360 (2017).
53. Laporta, M., Pegoraro, M. & Zanderighi, L. Perfluorosulfonated membrane (Nafion): FT-IR study of the state of water with increasing humidity. Phys. Chem. Chem. Phys. 1, 4619–4628 (1999).
54. Ping, Z. H., Nguyen, Q. T., Chen, S. M., Zhou, J. Q. & Ding, Y. D. States of water in different hydrophilic polymers — DSC and FTIR studies. Polymer (Guildf). 42, 8461–8467 (2001).
55. Iwamoto, R. Infrared and near-infrared study of the interaction of amide C=O with water in ideally inert medium. J. Phys. Chem. A 114, 7398–7407 (2010).
56. Falk, M. An infrared study of water in perfluorosulfonate (Nafion) membranes. https://doi.org/10.1139/v80-237 58, 1495–1501 (2011).
57. Nagano, S., Kodama, S. & Seki, T. Ideal spread monolayer and multilayer formation of fully hydrophobic polythiophenes via liquid crystal hybridization on water. Langmuir 24, 10498–10504 (2008).
58. Nagano, S. Inducing Planar Orientation in Side-Chain Liquid-Crystalline Polymer Systems via Interfacial Control. Chem. Rec. 16, 378–392 (2016).

Chapter 4

Pressure-sensitive sulfonated polyimides

Abstract

Pressure sensors have received extensive attention as an electronic component that is widely used in personal electronic equipment and industrial monitoring. In particular, new materials that can simultaneously respond to multiple stimuli in addition to pressure have received much attention. Herein, we preliminarily explore the basic properties of ion-conducting materials ASPI-1, ASPI-2 and APOS-PMDA as potential pressure-sensitive materials. Among them, ASPI-2 and APOS-PMDA show reproducible pressure sensitivity under humidified conditions. SpeciallyEspecially, the resistance of ASPI-2 can be increased to 2 times higher than the initial resistance as a maximum under the pressure, and its resistance increased linearly as a function of pressure, indicating that ASPI-2 is a potential piezoelectricity type pressure-sensitive material.

4.1 Introduction

As an important part of wearable electronic devices, pressure sensors have received extensive attention due to their wide application in health monitoring, artificial intelligence, internet of things and other fields.[1,2,3,4,5,6] Generally, pressure sensors convert pressure information into electrical signals which are easy to read and analyze by some method. The rapid development of materials science, systems engineering, signal processing and other technologies, making pressure sensors have unique advantages, such as low cost, excellent flexibility, and compatibility with large-area processing technologies.[7,8,9,10,11] Usually pressure sensors can be divided into piezoresistive, piezocapacitive, transistor, piezoelectric sensors according to the working principle.[12,13]

In practical applications, the ideal pressure sensor should have the characteristics of high sensitivity, wide working range, fast response speed and low hysteresis. Therefore, researchers have attempted to introduce well-defined morphological microstructures in pressure sensors to achieve large conductive contact changes, effective stress concentration, and signal conduction.[14,15,16,17,18] Common microstructures usually appear at the nano or micro scale, including tunable layer spacing, crack, porous hierarchical structure multiscale hierarchical structure, etc. [19,20,21,22,23,24,25,26]

In recent years, lamellar materials with variable interlayer distances have provided new ideas for the design and construction of pressure sensors due to their novel principles.[19,20,27,28] Gao et al fabricated a piezoresistive flexible pressure sensor with high sensitivity based on multilayer $Ti_3C_2T_x$ MXene.[19] Using transmission electron microscopy (TEM), they observed huge interlayer distances changes under pressure, providing a fundamental working mechanism for piezoresistive sensors. Huang et al. designed and fabricated a series of piezoresistive sensors based on active material obtained by the reaction between graphene oxide and three kinds of amino-functionalized molecules (triethylene glycol amine (R1), 1-octylamine (R2), and 4-aminobiphenyl (R3)).[20] This chemically modified graphene oxide can be spray-coated on the substrate to obtain a multi-layer structure, and the interlayer distance is determined by the employed molecules (ie, R1-R3 molecules). The results show that the sensitivity of the pressure sensor increases with the flexibility of the employed molecules. Yang et al. fabricated a piezoresistive sensor with high sensitivity and multifunctional microforce sensing by exploiting the designed channel confinement effect and compressible laminated MXene ($Ti_3C_2T_x$).[27]

The microstructure in the pressure sensor can be obtained by techniques such as self-assembly, patterning, auxiliary manufacturing, etc.[8,29,30,31,32,33] Self-assembly is driven by intermolecular interactions, electrostatic interactions, hydrophilic-hydrophobic interactions, etc. [13,34,35,36,37] Huang et al. reported a pressure sensor based on reduced graphene oxide (rGO) sponge microstructures and polyaniline (PANI) nanoarrays.[34] The microstructures are formed by self-assembly processes through strong π-π interactions, hydrogen bonding, and electrostatic interactions. There have been reports of pressure-sensitive materials fabricated based on hydrophilic-hydrophobic interactions. Jung et al. prepared porous pressure-sensitive rubber (PPSR) by the reverse micelle method.[8] The reverse micelles in the form of water droplets are surrounded by an emulsifier consisting of a mixture of PDMS/organic solvent/multi-walled carbon nanotubes. Reverse micelles migrate, merge and evaporate during the process, resulting in a porous structure.

Human skin is extremely sensitive to pressure, benefit from multi-layered structure. This multi-layer structure composed of epidermis, dermis, etc. can effectively transmit stress to enhance tactile perception.[38] Inspired by skin structure and function, researchers have developed a variety of pressure sensors with micro- or nano-scale multilayer structures. Ko and coworkers proposed a skin-like hierarchical nanoporous and interlocked micro-ridge structured polymer architecture with gradient elastic modulus for the fabrication of highly sensitive triboelectric sensors.[38] Pan and coworkers have presented the first skin-interfaced iontronic pressure-sensing architecture for wearable sensing, based on the emerging iontronic detection principle in an easy-to-apply imperceptible and ultrathin (1.9 μm) packaging.[39] R. Wood and coworkers present a versatile transduction mechanism for highly sensitive strain detection based on strain-mediated contact in anisotropically resistive structures (SCARS).[40]

The ability to mimic the complex function of human skin is of tremendous interest in the development of electronic sensors.[38] Functions in addition to pressure or tactile sensing are desirable to better adapt to the surrounding environment, including the abilities of strain, humidity and temperature measurement at the same time.[39,40] However, most previously reported materials are limited to single stimulus responses and have limited ability to perceive changes in multiple stimuli.[41] Normally, two strategies can be used to produce the multiple stimuli stimuli-responsive sensors. The first one is integrating multiple different kinds of single stimulus-responsive sensors on the same substrate.[42] The second one is development of new materials that can simultaneously sense and convert multiple stimuli changes into easily analyzed electrical signals

Generally, Alkyl sulfonated polyimides (ASPIs) is are considered to be one of the potential electrolyte materials due to its their high chemical stability, controllable molecular structure and high proton conductivity.[43,44,45,46] Driven by the lyotropic liquid crystal properties, ASPIs can self-assemble into ordered lamellar structures in solution. In particular, its ability to automatically form ordered structures under humidified conditions, which is called lyotropic LC property. When the polymer having this property is mixed with water or other polar solvents, it becomes a liquid crystal within a specific concentration range. Since the hydrophilic part and the hydrophobic part are gathered close and far away from water, respectively, phase separation will occur. And this phase separation will work as a proton transport channel to improve the proton conductivity. ASPIs are naturally sensitive to ambient temperature and humidity as an ionic (proton) conductor material. Moreover, ASPIs can form lamellar ordered structure driven lyotropic liquid crystalline property, when applied a pressure perpendicular to the ASPI thin film plane, the lamellar distance will decrease accordingly, resulting a change in proton conductivity. This makes them to be a kind of potential stimulus-responsive material.

4.2 Experimental section

4.2.1. Materials

3,3'-Bis(sulfopropoxy)-4,4'-diaminobiphenyl (BSPA), ASPI-1 and ASPI-2 was synthesized according to previous reports.[43,47,45] Triethylamine (TEA) was used as received from Kanto Chemical Co. Inc., Japan. Hydrochloric acid, m-cresol, acetic acid, acetic anhydride, methanol, and acetone were obtained from Fujifilm Wako Pure Chemical Corp., Japan. 1,2,3,4-Cyclopentanetetracarboxylic dianhydride was purchased from Tokyo Chemical Industry Co. Ltd., Japan.

4.2.2 Synthetic route of APOS

The synthesis of sulfonated diamine monomer APOS is shown in Scheme 4-1, and each step is described in detail as follows:

Step 1: Protection of amine groups

3,3'-dihydroxybenzidine (Tokyo Chemical Industry Co., Ltd.) 5 g, Acetic anhydride (Fujifilm Wako Pure Chemical Corporation) 79 ml, acetic acid (Wako) 1.5 ml, water (18 MΩ cm^{-1}) 200 ml were added into the Erlenmeyer flask and stirring at 70-80 ℃ for 2 h. After cooling to room temperature, the mixture was further cooled down by the ice bath. The solid product was separated from the mixture by centrifuge

5804（Eppendorf）and washed several times by with acetone. The calculated yield was 97% after the product had dried overnight in a vacuum.

Step 2: Introduction of side chain

Anhydrous potassium carbonate of 3.2 g and 60 ml acetonitrile (Wako, Japan) were added into a 100 ml three-necked flask and heated at 80 ℃. After the temperature reached 80 ℃, 8 ml 1,2-bis(2-chloroethoxy)ethane (TCI, Japan) was added into the three-necked flask, and 1.2 g (as total) of acetylated 3,3'-dihydroxybenzidine was added into the three-necked flask in six times within one hour to avoid the formation of crown ether structure. The reaction was carried out under an argon atmosphere for 72 h with a moderate argon flow to prevent excessive evaporation of acetonitrile.

After the reaction, the solid impurities were removed by suction filtration and acetonitrile was removed by rotary evaporator (Yamato Science). Followed by column chromatography was used to obtain pure product.

The mobile phase, ethyl acetate (Wako, Japan), was used by thin layer chromatography (TLC), and the wakogel C-200 (Wako, Japan) was used as stationary phase. After chromatography, the ethyl acetate was removed by rotary evaporator, and the yield was 39%.

Step 3: Sulfonation reaction

The product obtained in the previous step was reacted with sodium sulfite in a molar ratio of 1:4 to obtain a sulfonated product. The 0.92 g of the product obtained in the previous step, 1.53 g sodium sulfite, 31 ml ethanol and 31 ml distilled water, were added into a 100 ml three-necked flask with a magnetic stirring, and reacted under 100 ℃ for 24 hours under the protection of argon.

After the reaction, a rotary evaporator was used to remove the solvent. The sulfonated product can dissolve in methanol, but sodium sulfite or sodium chloride cannot. The solid product was dissolved in methanol and the insoluble impurities were removed by suction filtration. Followed by the solvent was removed by rotary evaporator, and the product was vacuum vacuum-dried overnight. The yield was 88%.

Step 4: Ion exchange

The solid product obtained in the previous step was dissolved in water (18 MΩ cm^{-1}). The aqueous

solution flowed through a glass column filled with ion exchange resin Amberlyst 33 (Organo) slowly. This process was repeated 5 times in order to exchange sodium ions into hydrogen ions as much as possible. Then the water was removed by rotary evaporator (Yamato Science).

Step 5: Removing protecting groups

The product obtained in the previous step was dissolved in 22 ml HCl (Wako, Japan), then reacted in a 25 ml three-necked flask under 120 ℃ for 2 hours under the protection of argon. After that, removed the condenser tube and raised the temperature up to 160 ℃ to evaporate HCl. The evaporated hydrochloric acid was absorbed with a sodium hydroxide solution prepared in advance. Then the solid product was washed by with 2-propanol with centrifugation by the Centrifuge5804 (Eppendorf) for several times. And the product was dried for one night by with vacuum dryer. The yield was 85%.

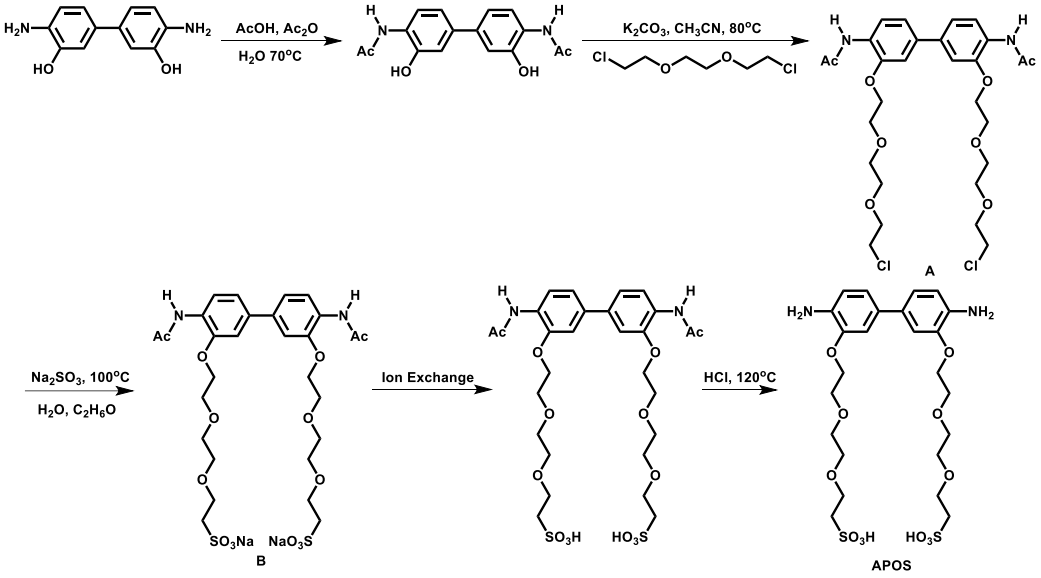

Scheme 4-1. Scheme for synthesizing APOS.

4.2.3 Synthetic route of APOS-PMDA

The process of polymer synthesis is shown in Scheme 4-2. 0.30 g sulfonated diamine monomer APOS (0.5 mmol), 0.11 g pyromellitic dianhydride (0.5 mmol) (TCI, Japan),5 ml m-cresol (Wako, Japan), and 150 μl triethylamine (Kanto Chemical, Japan) were added into a 25 ml three-necked flask, then reacted at 160 ℃ for 10 hours under the protection of argon gas flow. The product was cooled to the room temperature after the reaction. Then the cooled product was added to 50 ml cold acetone, and the solid product precipitated was obtained. The pure solid product was obtained by centrifugation and

washed several times with acetone, then dried under vacuum overnight.

The dried product was then dissolved in water, and ion exchange was carried out using a glass column packed with ion exchange resin Amberlyst 33 (Organo). This process was repeated several times to ensure that sulfonate was exchanged to sulfonic acid as much as possible. The solvent was removed by rotary evaporation and the final product APOS-PMDA was obtained after completely drying. The yield was 76%. The weight average molecular weight (M_w) of synthesized APOS-PMDA was 116,200 which was confirmed by Gel permeation chromatography (GPC).

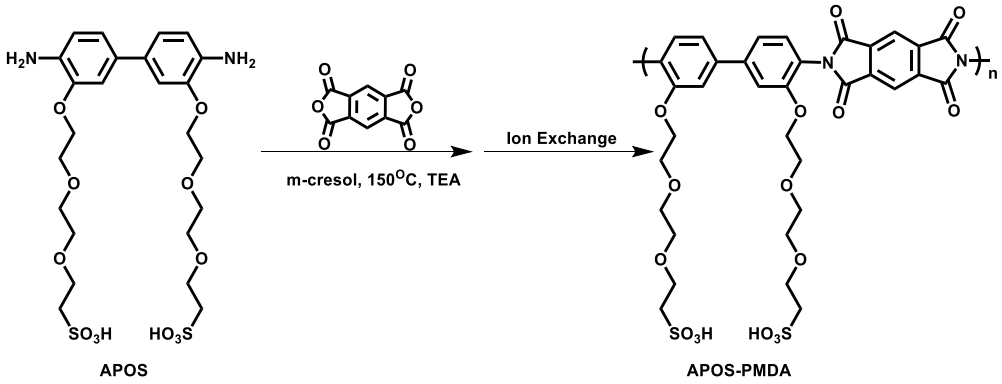

Scheme 4-2. Scheme for synthesizing APOS-PMDA.

4.2.4 Synthetic route of ASPI-1 and ASPI-2

The synthesis of ASPI-1 and ASPI-2 is shown in Scheme 4-3. Typically, 0.46 g sulfonated diamine monomer BSPA (1 mmol), 1 mmol dianhydride monomer (TCI, Japan),6 ml m-cresol (Wako, Japan), and 300 μl triethylamine (Kanto Chemical, Japan) were added into a 25 ml three-necked flask, then reacted at 150 ℃ for 6 hours under the protection of argon gas flow. The product was cooled to the room temperature after the reaction. Then the cooled product was added to 50 ml cold acetone, and the solid product precipitated was obtained. The pure solid product was obtained by centrifugation and washed several times with acetone, then dried under vacuum overnight.

The dried product was then dissolved in water, and ion exchange was carried out using a glass column packed with ion exchange resin Amberlyst 33 (Organo). This process was repeated several times to ensure that sulfonate was exchanged to sulfonic acid as much as possible. The solvent was removed by rotary evaporation and the final product was obtained after completely drying. After the ion exchange process, the products were further washed by with methanol. The Mw confirmed by GPC of synthesized ASPI-1 and ASPI-2 was 470,000 and 430,000, respectively.

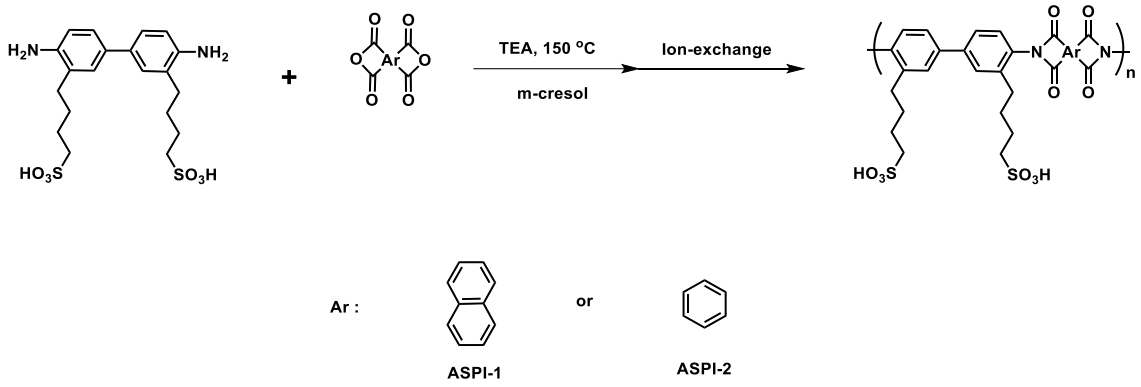

Scheme 4-3. Scheme for synthesizing ASPI-1 and ASPI-2.[45]

4.2.5 Thin film preparation

The spin coating (ACT-200 spin-coater; Active Co. Ltd.) method was used to prepare thin films. BSPA-CPDA was dissolved in the 1: 1 (w / w) of water and Tetrahydrofuran (THF) (Fujifilm Wako Pure Chemical Corporation). The thickness of thin films was controlled at about 500 nm. The the Si, SiO_2 substrates (E&M Co. Ltd.) and SiO_2-coated 9 MHz quartz crystals (Seiko EG&G Co. Ltd.) were washed by with 2-propanol in advance. Before thin film deposition, plasma treatment (Cute-MP; Femto Science, Korea) was carried out to improve the hydrophilic properties of the substrate surface.

4.2.6 Electrochemical impedance spectroscopy (EIS)

In order to measure the pressure sensitivity of the ASPI thin films, an original cell (Figure 4-1) that can measure the resistance changes of thin films under continuous pressure was fabricated. The resistance changes of ASPI thin films in the direction parallel to a substrate surface was measured by alternating current (AC) electrochemical impedance spectroscopy (EIS). The frequency response analyzer and high-frequency dielectric interface (SI1260 and SI1296; Solartron Analytical) were used to measure the impedance. A humidity- and temperature-controlled chamber (SH-221; Espec Corp.) was used to control the humidity and temperature during the experiment. The impedance was measured when an AC voltage of 50 mV was applied, and the frequency was scanned in the range of 1 Hz to 10 MHz. The RH was controlled between 40% and 95%, and the temperature was stable at 298 K.

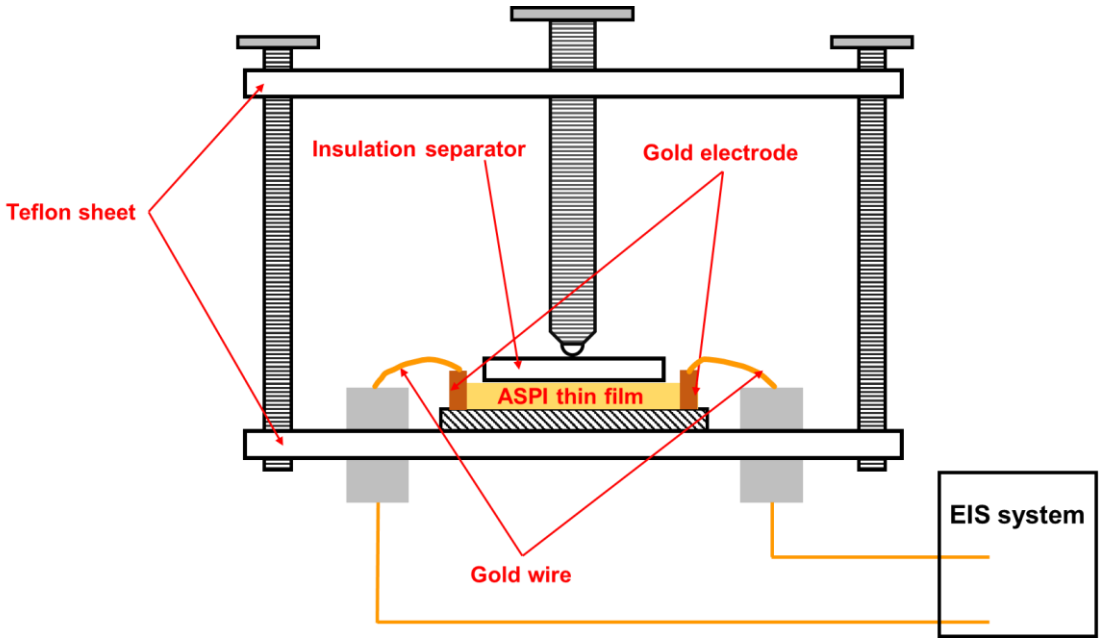

Figure 4-1. Schematic illustration of AC impedance method.

4.3 Results and discussions.

4.3.1 ^{1}H nuclear magnetic resonance (^{1}H NMR)

The structure and ^{1}H NMR results of ASPI-1, ASPI-2 and APOS-PMDA are shown in Figure 4-2. In all results, the peak appearing around 2.5 ppm was attributed to DMSO-d6, and the water peak appeared appearing near 3.5-3.8 ppm was attributed to water. In the result of APOS-PMDA, the signal of proton e, f, g, h was overlapped by water peck. Peaks from the possible by-product amide or carboxyl group were not observed, which proved that the imidization reaction was complete. Integration of proton peaks in ^{1}H NMR spectra was in good agreement with the number of protons in both the backbone and side chain.

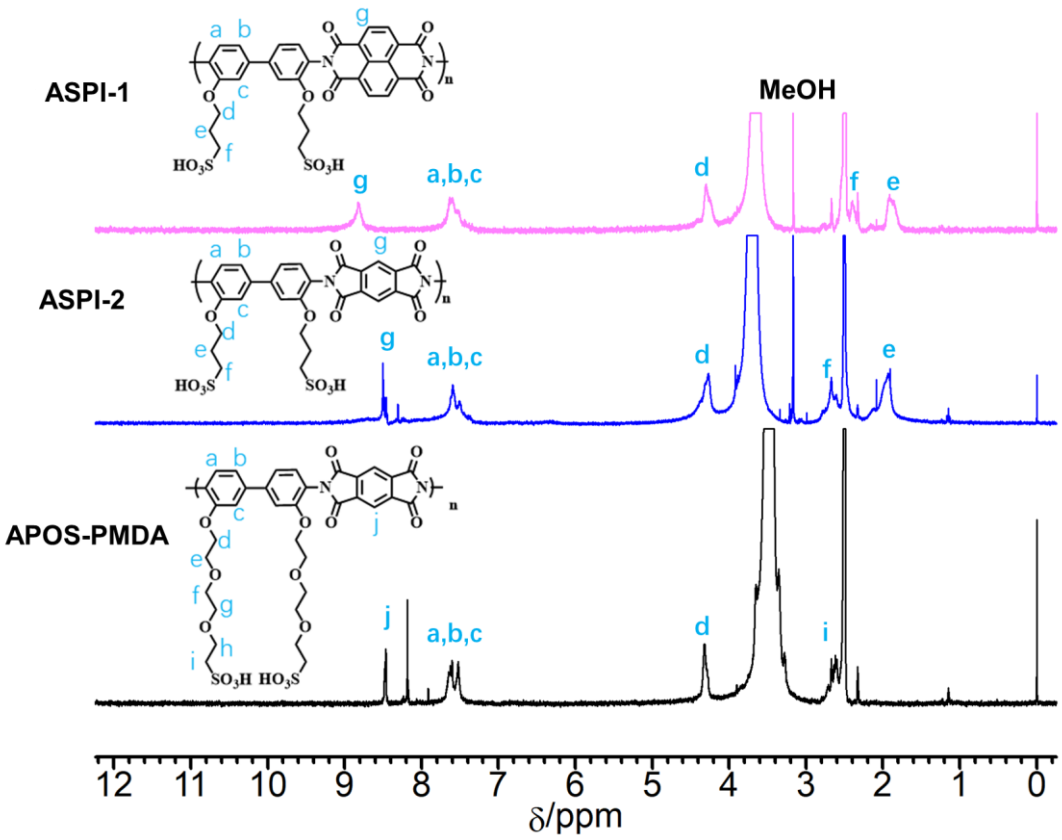

Figure 4-2. ^{1}H NMR results of ASPI-1, ASPI-2 and APOS-PMDA

4.3.2 Qualitative analysis

To explore whether ASPI-1, ASPI-2 and PMDA-APOS thin films are pressure sensitive, their impedances were measured under constant pressure and different humidity conditions. Figure 4-3 shows the Nyquist plots of ASPI-1 thin film with and without 0.18 MPa pressure applied. The electrical resistance as a function of humidity and pressure obtained from the Nyquist plot is shown in Figure 4-4. The resistance of ASPI-1 thin film did not exhibit a repeatable change as pressure is applied or removed, indicating that ASPI-1 thin film is not pressure sensitive.

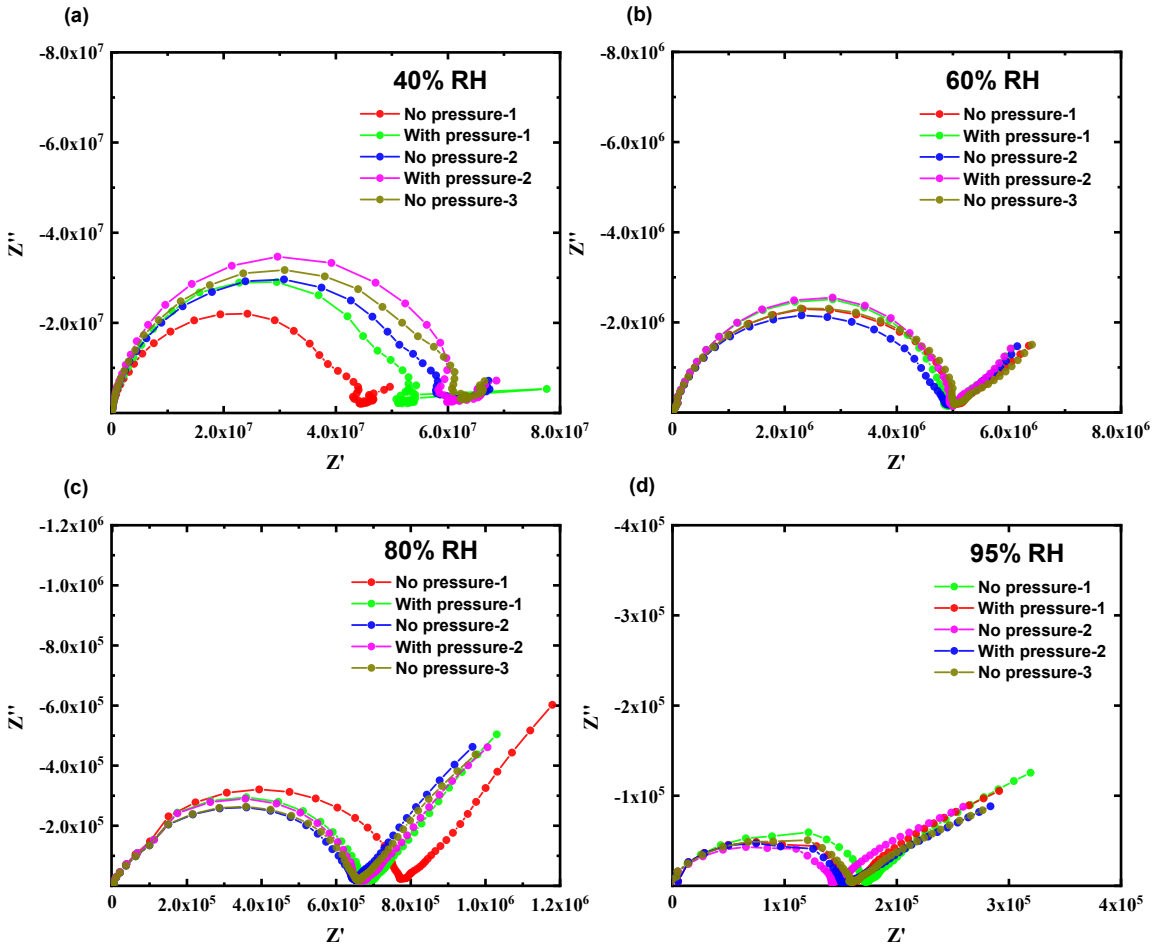

Figure 4-3. Nyquist plots of ASPI-1 thin film under different RH conditions with and without 0.18 MPa pressure applied.

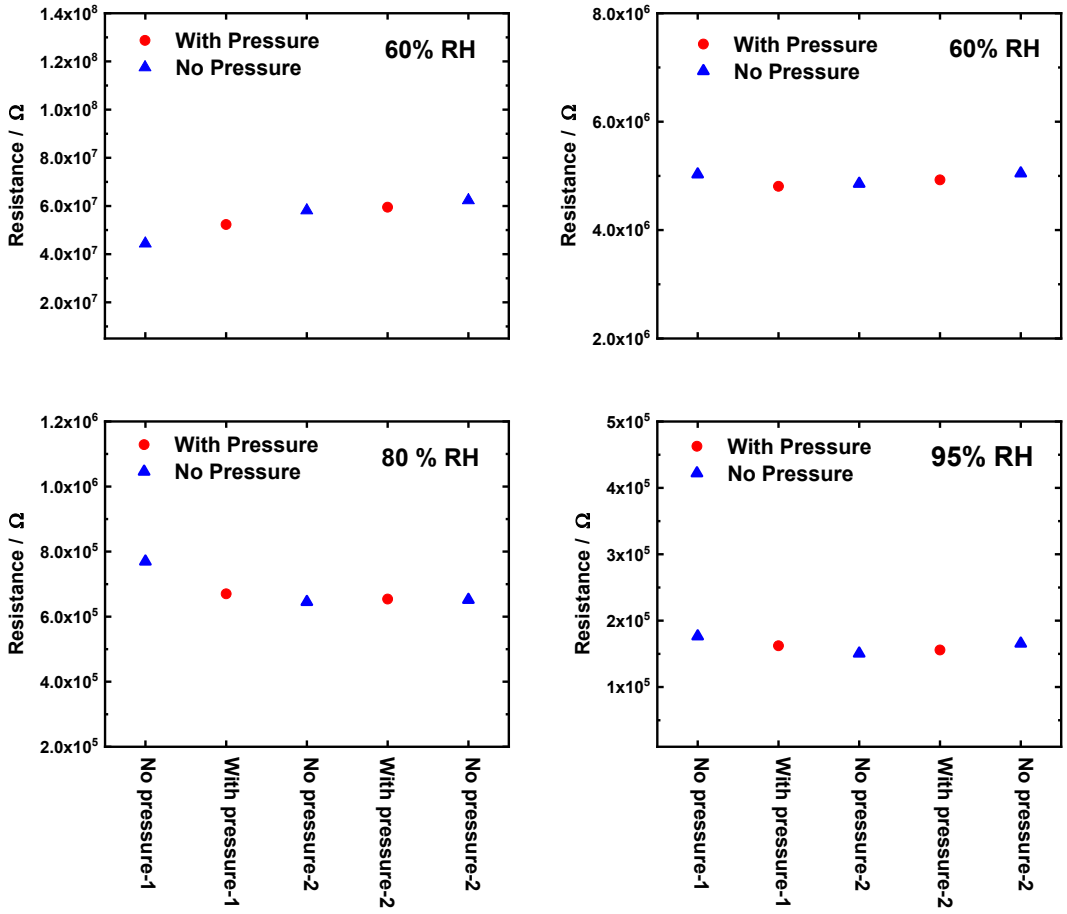

Figure 4-4. Resistance changes of ASPI-1 thin film under different RH conditions with and without pressure.

Figure 4-5 shows the Nyquist plots of ASPI-2 thin film with and without 0.19 MPa pressure applied. The electrical resistance as a function of humidity and pressure obtained from the Nyquist plot is shown in Figure 4-6. Under 40% RH, the resistance of ASPI-2 thin film did not exhibit a repeatable change as pressure was applied or removed. However, at 60% RH, the resistance of ASPI-2 thin film increases significantly when pressure is applied and decreases when pressure is removed. When the humidity was increased to 80% and 90% RH, the resistance of ASPI-2 thin film still exhibited repeatable changes with the application or removal of pressure. When the pressure is applied, its resistance can be up to 2 times higher than the initial resistance. And when the pressure is removed its resistance can be restored to the same magnitude as the initial resistance. These indicate that under high humidity conditions, ASPI-2 thin film exhibits good pressure sensitivity and repeatability.

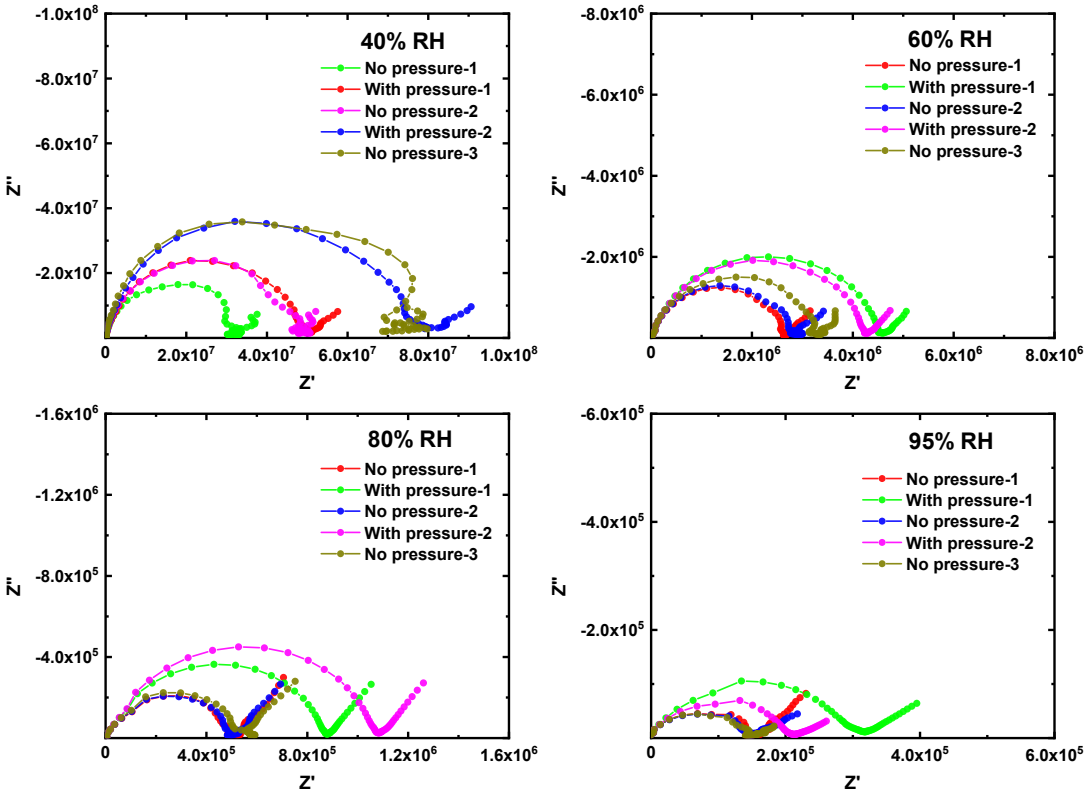

Figure 4-5. Nyquist plots of ASPI-2 thin film under different RH conditions with and without 0.19 MPa pressure applied.

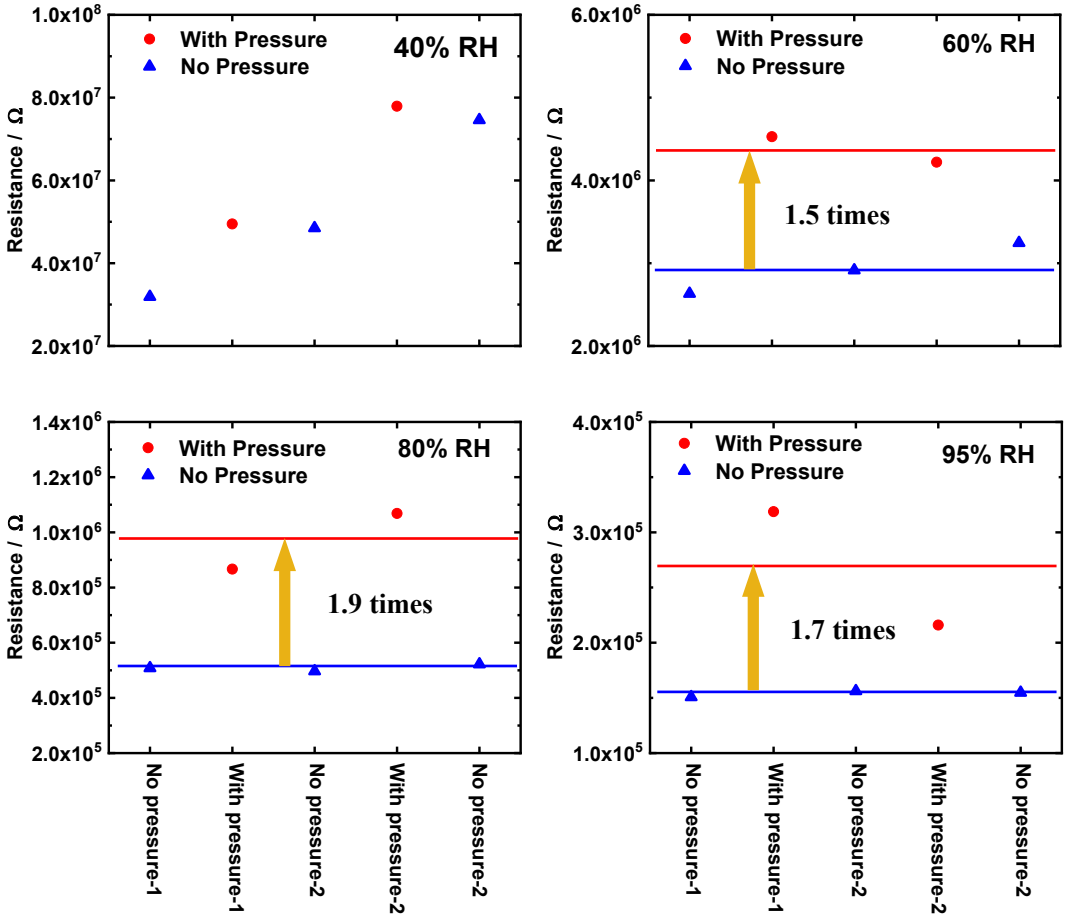

Figure 4-6. Resistance changes of ASPI-2 thin film under different RH conditions with and without pressure.

Figure 4-7 shows the Nyquist plots of APOS-PMDA thin film with and without 0.16 MPa pressure applied. The electrical resistance as a function of humidity and pressure obtained from the Nyquist plot is shown in Figure 4-8. Under 40% RH, the resistance of APOS-PMDA thin film was too large to be determined. Under 60% RH, the resistance of APOS-PMDA thin film did not exhibit a repeatable change as pressure was applied or removed. Under 80% and 90% RH, the resistance of APOS-PMDA thin film only increases by a maximum of 50% when pressure is applied. This indicates that APOS-PMDA is less pressure sensitive than ASPI-2.

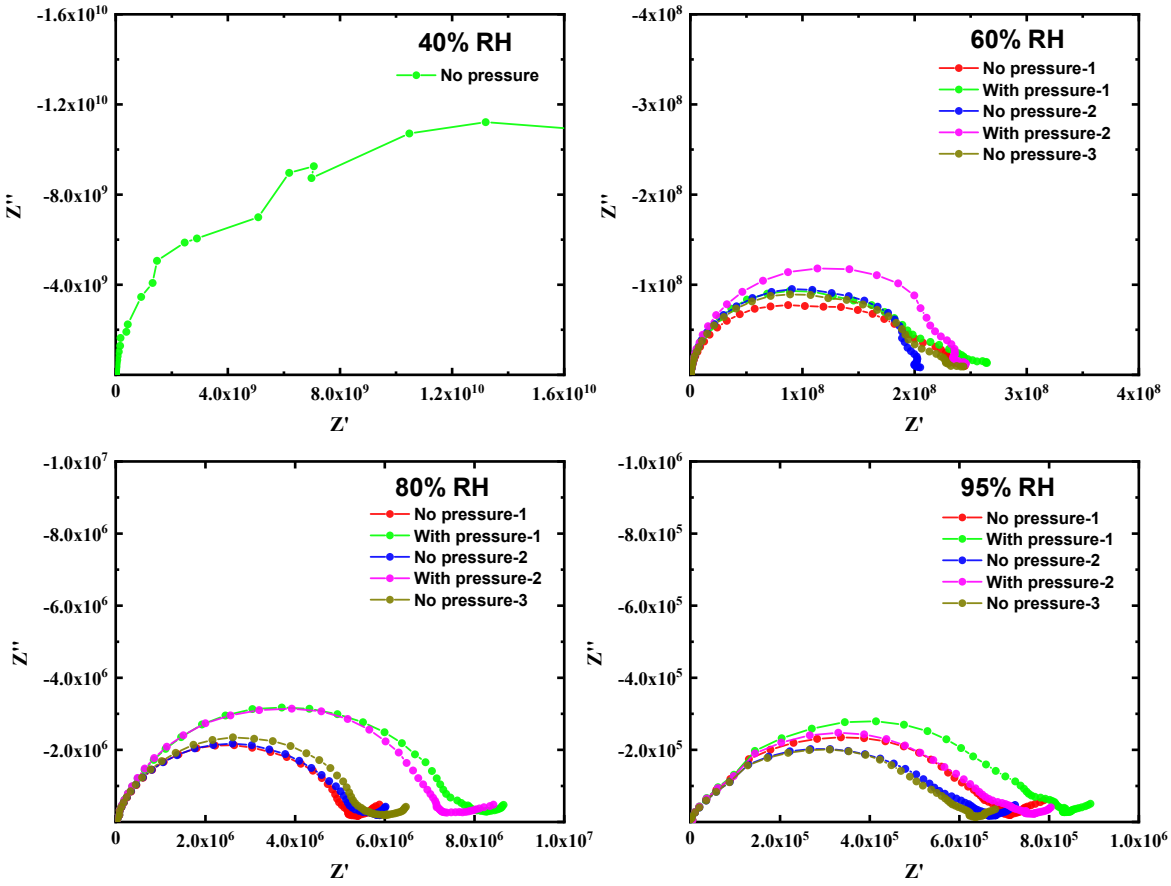

Figure 4-7. Nyquist plots of APOS-PMDA thin film under different RH conditions with and without 0.16 MPa pressure applied.

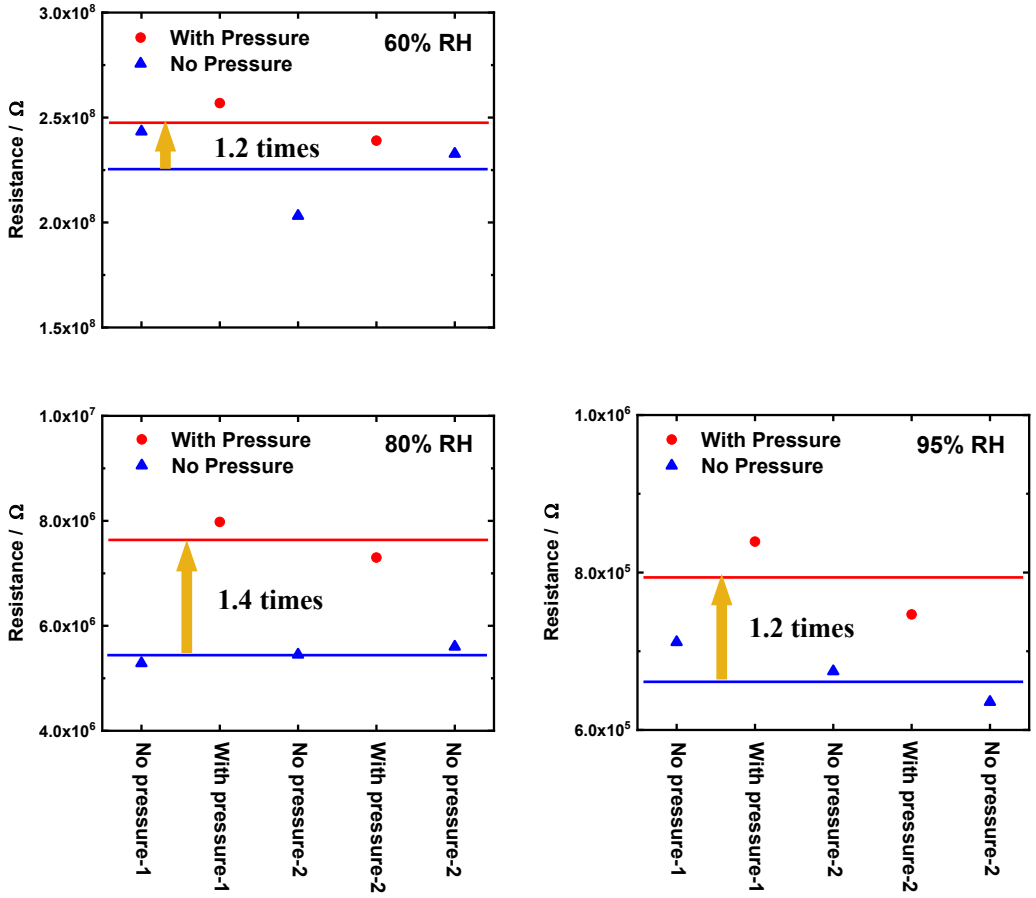

Figure 4-8. Resistance changes of APOS-PMDA thin film under different RH conditions with and without pressure.

Qualitative analysis of three ASPI materials shows that ASPI-1 has no pressure sensitivity, while ASPI-2 and APOS-PMDA show reproducible pressure sensitivity under high humidity conditions. Particularly, the resistance of ASPI-2 can be increased to 2 times higher than the initial resistance under the pressure, proving that ASPI-2 is a potential pressure-sensitive material.

4.3.3 Quantitative analysis

Since ASPI-2 has good pressure sensitivity, in order to explore the relationship between its resistance change and applied pressure, the resistance change as a function of pressure was measured under 60% and 80% RH.

Figure 4-9 (a) and (b) shows the results of the Nyquist plots and obtained resistance of ASPI-2 thin film as a function of pressure under 60% RH, respectively. The results show that the resistance of ASPI-2 thin film increases linearly with increasing the pressure between 0.1 and 0.2 MPa. The sensitivity (S) of ASPI-2 thin film is calculated to be 24 MPa^{-1} by using the equation $S=\delta(\Delta R/R_0)/\delta P$, where P is the

applied pressure, R and R_0 represent the resistance with or without pressure, respectively.[20] Compared with previously reported materials, ASPI-2 exhibited the highest sensitivity in a similar pressure range (Table 4-1).[48,49,50,51] However, when removed pressure its resistance cannot restore to the initial value completely.

Table 4-1. Comparison of sensitivity of ASPI-2 thin film with reported materials.

Material	Pressure region (MPa)	**Sensitivity** (MPa^{-1})
ASPI-2	0.1-0.2	24
Ag NW[48]	<0.5	1.62
Si NM[49]	0-0.25	0.48
Gold thin film[50]	0-0.16	0.4
PDMS[51]	0-0.25	4.8

Figure 4-9 (c) and (d) shows the results of Nyquist plots and obtained resistance of ASPI-2 thin film as a function of pressure under 80% RH, respectively. Unlike the results at 60% RH, the resistance of ASPI-2 did not increase linearly with increasing pressure at 80% RH between 0.1 and 0.2 MPa. However, it is worth noting that the resistance of ASPI-2 at 80% RH can recover to its initial value when the pressure is removed. This was also demonstrated in qualitative analysis above. Considering that increased humidity corresponds to a change in water uptake, more water molecule adsorption is therefore considered to be beneficial for maintaining the pressure sensitivity of ASPI-2.

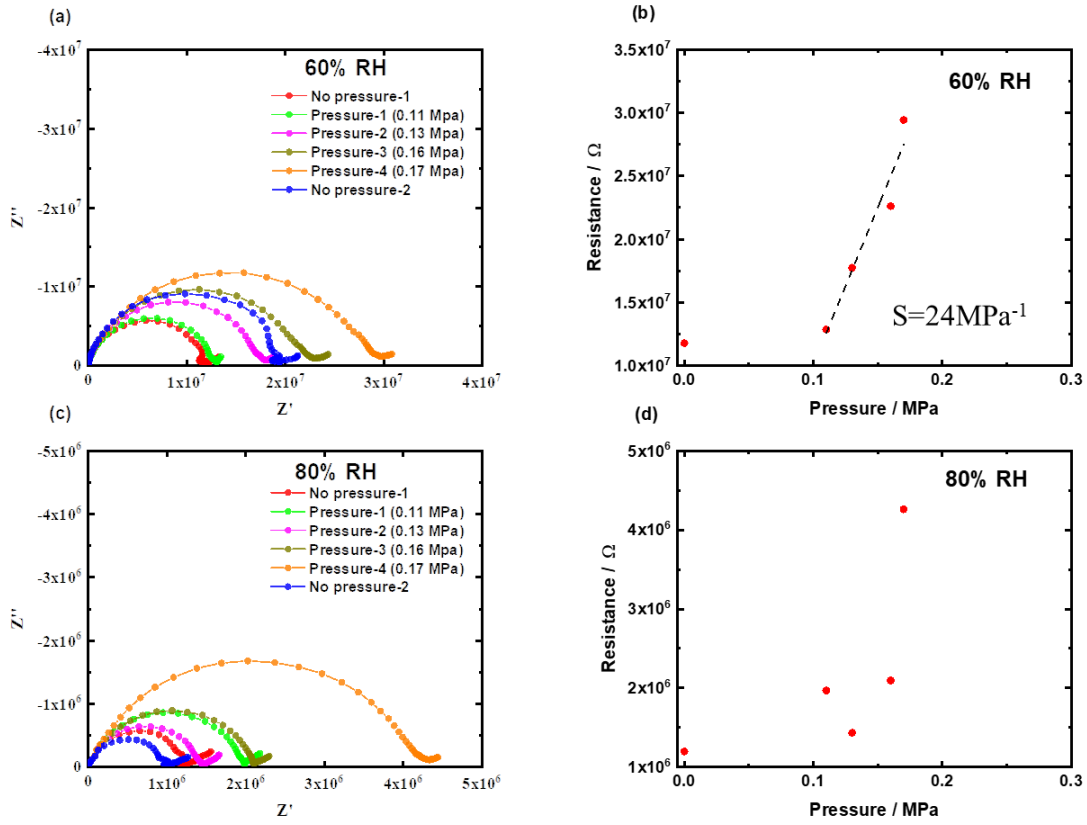

Figure 4-9. Nyquist plots (a) and resistance (b) of ASPI-2 thin film as a function of pressure under 60% RH; Nyquist plots (c) and resistance (d) of ASPI-2 thin film as a function of pressure under 80% RH

To confirm that more water uptake is beneficial for maintaining the pressure sensitivity of ASPI-2, after measured measuring the change in resistance with pressure at 60% RH, the humidity was increased to 80% RH and kept for 1 h, then the humidity was decreased to 60% RH, and the resistance was measured again. The result is shown in the Figure 4-10. The resistance of ASPI-2 cannot return to its initial value when keep at 60% RH. But after being kept at 80% RH for 1 h, its resistance even became lower than the initial value.

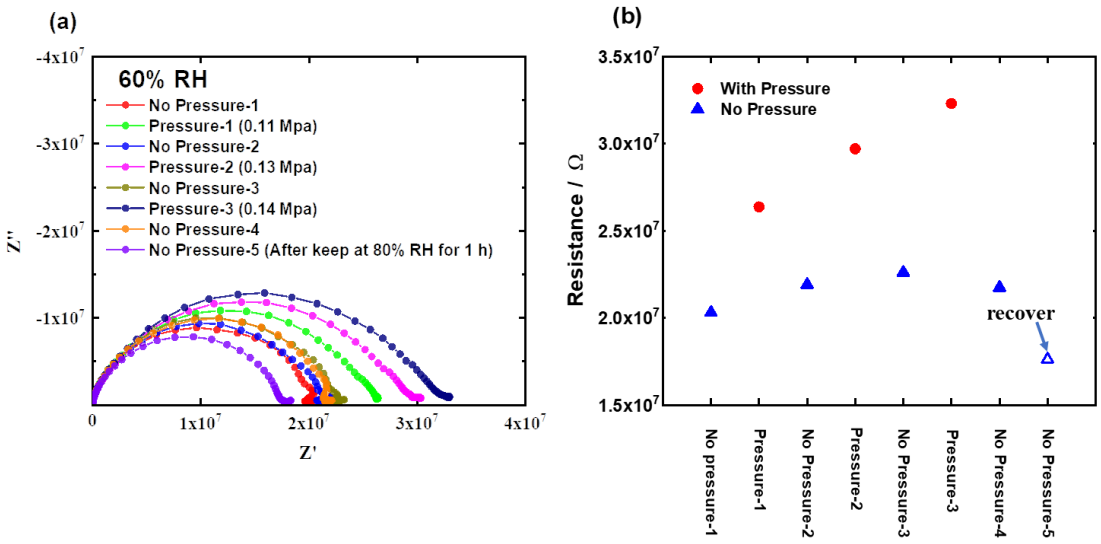

Figure 4-10. (a) Nyquist plots and (b) resistance changes of ASPI-2 thin film under 60% RH conditions with and without pressure**.**

To further confirm whether the recoverable resistance was caused by residual water or structural recovery, the adsorption-desorption curves of ASPI-2 were measured. As shown in Figure 4-11, when the humidity is less than 90% RH, the uptake of ASPI-2 under the same RH during the adsorption and desorption processes is the same, indicating that no excess water molecules were remaining during the desorption process. Combined with the results mentioned above, it is reasonable to consider that the recoverable resistance in ASPI-2 is caused by the recovery of the lamellar structure due to the lyotropic LC property.

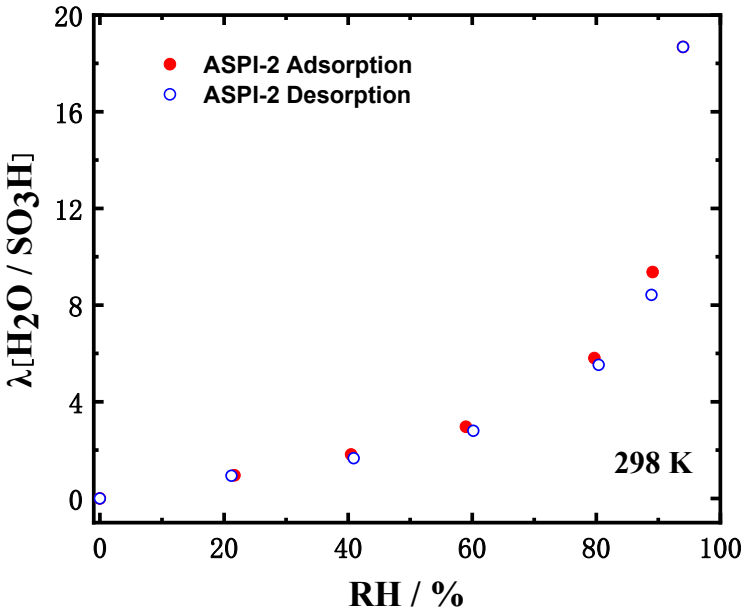

Figure 4-11. Water uptake of ASPI-2 thin film as a function of RH during adsorption and desorption process.

4.3 Conclusion

In this chapter, the basic pressure sensitivity of three ASPIs (ASPI-1, ASPI-2 and APOS-PMDA) was investigated. The qualitative analysis of three ASPI materials shows that ASPI-1 has no pressure sensitivity, while ASPI-2 and APOS-PMDA show reproducible pressure sensitivity under high humidity conditions. Particularly, the resistance of ASPI-2 can be increased to 1.9 times higher than the initial resistance under the pressure, proving that ASPI-2 is a potential pressure-sensitive material. The quantitative analysis shows that the resistance of ASPI-2 thin film increases linearly with increasing the pressure between 0.1 and 0.2 MPa. Water molecules were shown to contribute to the recovery of the resistance of ASPI-2 and did not remain in the thin film during desorption, indicating the recoverable electrical resistance can be attributed to the recovery of the lamellar structure.

4.4 Future plan

In this chapter, only the primary properties of ASPIs as pressure-sensitive materials were investigated. However, the mechanism behind this phenomenon has not been investigated in detail. For example, whether the increase in ion conduction resistance under pressure comes from the displacement of the polymer molecular chain or from the destruction of the orderly structure. Understanding the mechanisms involved has important implications for designing pressure pressure-sensitive ASPIs with higher sensitivity and a wider operating range.

In addition, quantitative analysis of ASPI-2 is also crude due to equipment limitations. Based on the results at this stage, ASPI-2 exhibited a linear trend characteristic of piezoresistivity in the medium-pressure range. However, it remains to be explored whether ASPI-2 can maintain this trend in the lower pressure range. Because the range in which the resistance can continuously and stably maintain a linear change directly affects the application scenario of the material, in the context of the rapid development of wearable health care applications today, people pay more attention to the performance of the material in low-pressure (1–10 kPa) or even subtle-pressure (1 Pa–1 kPa) range. This needs to establish a more accurate system to measure.

Response speed and durability are another two important parameters for pressure pressure-sensitive materials. These properties are not characterized in this study, which requires continued efforts by successors.

References

1. Boutry, C. M. et al. Biodegradable and flexible arterial-pulse sensor for the wireless monitoring of blood flow. Nat. Biomed. Eng. 2019 31 3, 47–57 (2019).
2. Chu, Y. et al. Human Pulse Diagnosis for Medical Assessments Using a Wearable Piezoelectret Sensing System. Adv. Funct. Mater. 28, 1803413 (2018).
3. Chortos, A. & Bao, Z. Skin-inspired electronic devices. Mater. Today 17, 321–331 (2014).
4. Dahiya, R. S., Metta, G., Valle, M. & Sandini, G. Tactile sensing-from humans to humanoids. IEEE Trans. Robot. 26, 1–20 (2010).
5. Guo, X. et al. Artificial Intelligence-Enabled Caregiving Walking Stick Powered by Ultra-Low-Frequency Human Motion. ACS Nano 15, 19054–19069 (2021).
6. Huang, Y. C. et al. Sensitive pressure sensors based on conductive microstructured air-gap gates and two-dimensional semiconductor transistors. Nat. Electron. 2020 31 3, 59–69 (2020).
7. Ha, M. et al. Bioinspired Interlocked and Hierarchical Design of ZnO Nanowire Arrays for Static and Dynamic Pressure-Sensitive Electronic Skins. Adv. Funct. Mater. 25, 2841–2849 (2015).
8. Jung, S. et al. Reverse-Micelle-Induced Porous Pressure-Sensitive Rubber for Wearable Human–Machine Interfaces. Adv. Mater. 26, 4825–4830 (2014).
9. Lv, L., Zhang, P., Xu, T. & Qu, L. Ultrasensitive Pressure Sensor Based on an Ultralight Sparkling Graphene Block. ACS Appl. Mater. Interfaces 9, 22885–22892 (2017).
10. Tao, L. Q. et al. Graphene-Paper Pressure Sensor for Detecting Human Motions. ACS Nano 11, 8790–8795 (2017).
11. Cheng, H., Wang, B., Yang, K. & Wang, C. A low-cost piezoresistive pressure sensor with a wide strain range – featuring polyurethane sponge@poly(vinyl alcohol)/sulfuric gel electrolyte. J. Mater. Chem. C 9, 1014–1024 (2021).
12. Shi, Z. et al. Morphological Engineering of Sensing Materials for Flexible Pressure Sensors and Artificial Intelligence Applications. Nano-Micro Lett. 2022 141 14, 1–48 (2022).
13. Zang, Y., Zhang, F., Di, C. A. & Zhu, D. Advances of flexible pressure sensors toward artificial intelligence and health care applications. Mater. Horizons 2, 140–156 (2015).
14. Huang, Y. et al. Wood Derived Composites for High Sensitivity and Wide Linear-Range Pressure Sensing. Small 14, 1801520 (2018).
15. Xiao, J., Tan, Y., Song, Y. & Zheng, Q. A flyweight and superelastic graphene aerogel as a high-capacity adsorbent and highly sensitive pressure sensor. J. Mater. Chem. A 6, 9074–9080 (2018).
16. Yao, H.-B. et al. A Flexible and Highly Pressure-Sensitive Graphene–Polyurethane Sponge Based on Fractured Microstructure Design. Adv. Mater. 25, 6692–6698 (2013).
17. Yin, B., Liu, X., Gao, H., Fu, T. & Yao, J. Bioinspired and bristled microparticles for ultrasensitive pressure and strain sensors. Nat. Commun. 2018 91 9, 1–8 (2018).
18. Shi, L. et al. Quantum effect-based flexible and transparent pressure sensors with ultrahigh sensitivity and sensing density. Nat. Commun. 2020 111 11, 1–9 (2020).
19. Ma, Y. et al. A highly flexible and sensitive piezoresistive sensor based on MXene with greatly changed interlayer distances. Nat. Commun. 2017 81 8, 1–8 (2017).
20. Huang, C.-B. et al. Molecule–Graphene Hybrid Materials with Tunable Mechanoresponse: Highly Sensitive Pressure Sensors for Health Monitoring. Adv. Mater. 31, 1804600 (2019).

21. Kang, D. et al. Ultrasensitive mechanical crack-based sensor inspired by the spider sensory system. Nat. 2014 5167530 516, 222–226 (2014).
22. Choi, Y. W. et al. Ultra-sensitive Pressure sensor based on guided straight mechanical cracks. Sci. Reports 2017 71 7, 1–8 (2017).
23. Shi, X. et al. Pushing detectability and sensitivity for subtle force to new limits with shrinkable nanochannel structured aerogel. Nat. Commun. 2022 131 13, 1–10 (2022).
24. Wang, C. et al. Multifunctional, Highly Flexible, Free-Standing 3D Polypyrrole Foam. Small 12, 4070–4076 (2016).
25. Wang, M. et al. Wavelength-Gradient Graphene Films for Pressure-Sensitive Sensors. Adv. Mater. Technol. 4, 1800363 (2019).
26. Chen, S., Song, Y. & Xu, F. Flexible and Highly Sensitive Resistive Pressure Sensor Based on Carbonized Crepe Paper with Corrugated Structure. ACS Appl. Mater. Interfaces 10, 34646–34654 (2018).
27. Gao, Y. et al. Microchannel-Confined MXene Based Flexible Piezoresistive Multifunctional Micro-Force Sensor. Adv. Funct. Mater. 30, 1909603 (2020).
28. Chen, M. et al. Self-assembly of dendritic-lamellar MXene/Carbon nanotube conductive films for wearable tactile sensors and artificial skin. Carbon N. Y. 164, 111–120 (2020).
29. Si, Y. et al. Ultralight Biomass-Derived Carbonaceous Nanofibrous Aerogels with Superelasticity and High Pressure-Sensitivity. Adv. Mater. 28, 9512–9518 (2016).
30. Guo, S.-Z. et al. 3D Printed Stretchable Tactile Sensors. Adv. Mater. 29, 1701218 (2017).
31. Yin, M.-J. et al. Micropatterned Elastic Gold-Nanowire/Polyacrylamide Composite Hydrogels for Wearable Pressure Sensors. Adv. Mater. Technol. 3, 1800051 (2018).
32. Asghar, W. et al. Piezocapacitive Flexible E-Skin Pressure Sensors Having Magnetically Grown Microstructures. Adv. Mater. Technol. 5, 1900934 (2020).
33. Yang, J. C. et al. Microstructured Porous Pyramid-Based Ultrahigh Sensitive Pressure Sensor Insensitive to Strain and Temperature. ACS Appl. Mater. Interfaces 11, 19472–19480 (2019).
34. Huang, J. et al. Improvement of piezoresistive sensing behavior of graphene sponge by polyaniline nanoarrays. J. Mater. Chem. C 7, 7386–7394 (2019).
35. Guo, Q. et al. Protein-Inspired Self-Healable Ti3C2 MXenes/Rubber-Based Supramolecular Elastomer for Intelligent Sensing. ACS Nano 14, 2788–2797 (2020).
36. Zhu, M. et al. Hollow MXene Sphere/Reduced Graphene Aerogel Composites for Piezoresistive Sensor with Ultra-High Sensitivity. Adv. Electron. Mater. 6, 1901064 (2020).
37. Shi, S. et al. Self-Assembly of MXene-Surfactants at Liquid–Liquid Interfaces: From Structured Liquids to 3D Aerogels. Angew. Chemie Int. Ed. 58, 18171–18176 (2019).
38. Liu, Y., Pharr, M. & Salvatore, G. A. Lab-on-Skin: A Review of Flexible and Stretchable Electronics for Wearable Health Monitoring. ACS Nano 11, 9614–9635 (2017).
39. Wang, C., Xia, K., Zhang, M., Jian, M. & Zhang, Y. An All-Silk-Derived Dual-Mode E-skin for Simultaneous Temperature-Pressure Detection. ACS Appl. Mater. Interfaces 9, 39484–39492 (2017).
40. Trung, T. Q., Ramasundaram, S., Hwang, B. U. & Lee, N. E. An All-Elastomeric Transparent and Stretchable Temperature Sensor for Body-Attachable Wearable Electronics. Adv. Mater. 28, 502–509 (2016).
41. Guo, Q., Qiu, X. & Zhang, X. Recent Advances in Electronic Skins with Multiple-Stimuli-Responsive and Self-Healing Abilities. Materials (Basel). 15, (2022).
42. Hua, Q. et al. Skin-inspired highly stretchable and conformable matrix networks for multifunctional sensing. Nat. Commun. 9, 1–11 (2018).

43. KRISHNAN, K. et al. Influence of Confined Polymer Structure on Proton Transport Property in Sulfonated Polyimide Thin Films. Electrochemistry 82, 865–869 (2014).
44. Nagao, Y. Proton-Conductivity Enhancement in Polymer Thin Films. Langmuir 33, 12547–12558 (2017).
45. Ono, Y. et al. High Proton Conduction of Organized Sulfonated Polyimide Thin Films with Planar and Bent Backbones. Macromolecules 51, 3351–3359 (2018).
46. Takakura, K. et al. Lyotropic ordering for high proton conductivity in sulfonated semialiphatic polyimide thin films. Polym. J. 51, 31–39 (2019).
47. Krishnan, K., Iwatsuki, H., Hara, M., Nagano, S. & Nagao, Y. Proton conductivity enhancement in oriented, sulfonated polyimide thin films. J. Mater. Chem. A 2, 6895–6903 (2014).
48. Yao, S. & Zhu, Y. Wearable multifunctional sensors using printed stretchable conductors made of silver nanowires. Nanoscale 6, 2345–2352 (2014).
49. Ying, M. et al. Silicon nanomembranes for fingertip electronics. Nanotechnology 23, 344004 (2012).
50. Cotton, D. P. J., Graz, I. M. & Lacour, S. P. A multifunctional capacitive sensor for stretchable electronic skins. IEEE Sens. J. 9, 2008–2009 (2009).
51. Lee, H. K., Chang, S. Il & Yoon, E. A flexible polymer tactile sensor: Fabrication and modular expandability for large area deployment. J. Microelectromechanical Syst. 15, 1681–1686 (2006).

Chapter 5
General Conclusions

5.1 Conclusions

Ionomer thin film is a critical part of the triple-phase interface of polymer electrolyte membrane fuel cells (PEMFCs). It not only needs to act as a binder to link the Pt-loaded catalyst particles with the gas diffusion layer but also to undertake the transport of protons within the catalyst layer. Although Nafion has achieved great success as a standard material for proton transport with high physicochemical properties. However, the huge performance degradation when it is processed into ultrathin films forces people to search for more suitable ionomer materials.

In chapter 2 and 3, the properties of sulfonated semi-alicyclic oligo- / polyimide as a highly proton-conducting ionomer are explored by introducing alicyclic structures into the backbone. The effect of alicyclic structure on the ordered structure caused by the lyotropic liquid crystal properties was mainly studied.

In chapter 2, a sulfonated semi-alicyclic polyimide (BSPA-BOEDA) with a dienophile structure in backbone was newly synthesized. A facile cross-linking reaction was carried out via Fe^{3+}-catalyzed Diels–Alder (D-A) reaction between BSPA-BOEDA and silica nanoparticles modified by (3-cyclopentadienylpropyl) triethoxyslane (CPTS). Compared with BSPA-BOEDA, the cross-linked BSPA-BOEDA-NPs membrane and thin film showed better stability in water. Because of the nonlinear molecular conformation of BSPA-BOEDA neither BSPA-BOEDA nor BSPA-BPEDA-NPs can form well-defined ordered structures but only form phase separation. The proton conductivity of BSPA-BPEDA-NPs thin film is lower than that of BSPA-BOEDA thin film due to the cross-linking, reaching maxima value of 0.01 and 0.04 S cm^{-1} at 25 °C and 95% RH, respectively.

In chapter 3, a sulfonated semi-alicyclic oligoimide (BSPA-CPDA) with a linear molecular conformation was newly synthesized. Benefiting from this conformation, the BSPA-CPDA thin film forms a lamellar structure similar to that of fully aromatic alkyl sulfonated polyimides driven by lyotropic liquid crystal properties, even the molecular weight is significantly lower. The BSPA-CPDA thin film exhibits a high proton conductivity of 0.2 S cm^{-1} at 95% RH, 25℃, which is the highest value among reported alkyl sulfonated polyimides with comparable molecular weight.

Benefiting from the need to develop wearable healthcare applications, the development of novel materials that can respond to multiple stimuli simultaneously is a topic of note. Alkyl sulfonated polyimides (ASPIs), which are a kind of ion-conducting material, can be a candidate for multiple stimuli-responsive

materials due to their natural sensitivity to humidity and temperature.

In chapter 4, The measurement process of the resistance change of ASPI thin films under continuous pressure was newly established. The basic pressure sensitivity of three ASPIs (ASPI-1, ASPI-2 and APOS-PMDA) was investigated. The results show that ASPI-1 has no pressure sensitivity, while ASPI-2 and APOS-PMDA show reproducible pressure sensitivity under humidified conditions. Particularly, the resistance of ASPI-2 thin film increases linearly with increasing the pressure between 0.1 and 0.2 MPa and the calculated sensitivity is 24 MPa^{-1}.

5.2 Future scope

1. This thesis has revealed the effect of the alicyclic structures on the lyotropic liquid crystal properties and proton conductivity. However, there is still a lack of molecular dynamics explanation for the formation process of the lamellar structure driven by the lyotropic liquid crystal properties. Therefore, in future work, an appropriate model should be established to perform accurate simulation calculations on this phenomenon to provide data support for explaining the mechanism of lyotropic liquid crystal properties. In addition, only the proton conductivity of ASPIs has been systematically investigated so far, however, whether it can effectively improve the performance of fuel cells when applied in fuel cells is still unknown.
2. As mentioned at the end of chapter 4, the exploration of the pressure sensitivity of ASPIs is still in its infancy. A more detailed investigation of the mechanism, response speed, durability, etc. is still required in future work.

Acknowledgments

I would like to offer my sincere thanks to my supervisor, Professor Yuki Nagao, for providing academic guidance and kind support during my doctoral study period.

I would like to express my appreciation to Professor Matsumi for his support with my minor research project and for his academic advice. I also appreciate Ms. Anusha's guidance with the minor research project. I was able to understand the Lithium-ion battery experiment specifics with Ms. Anusha's guidance.

I would like to acknowledge my gratitude to Professor Kaneko, who is my second supervisor and provides helpful advice. I would like to express my appreciation to Professor Nagano for his academic advice on my research project. I also want to thank Dr. Hara for supporting GIXRS measurement.

I want to express my thanks to everyone of the Nagao laboratory for their kind help throughout my doctoral study period.

Finally, I am deeply grateful to my family and friends for their support and encouragement.

Yuze Yao

School of Materials Science

Japan Advanced Institute of Science and Technology

Achievements

Research Publications:

1. **Yuze Yao,** Hayato Watanabe, Mitsuo Hara, Shusaku Nagano, Yuki Nagao*, Lyotropic Liquid Crystalline Property and Organized Structure in High Proton-Conductive Sulfonated Semi-Alicyclic Oligoimide Thin Films (Resubmitted)
2. Z. Li*, **Y. Yao**, D. Wang, M.M.Hasan, A. Suwansoontorn, H. Li*, G. Du, Z. Liu, Y. Nagao*, Intrinsic proton conduction in 2D sulfonated covalent organic frameworks through a post-synthetic strategy, Mater. Chem. Front. 2020, 4, 2339-2345.
3. L. Zhai, **Y. Yao**, B. Ma, M.M.Hasan, Y. Han, L. Mi*, Y. Nagao*, Z. Li*, Macromol. Accumulation of Sulfonic Acid Groups Anchored in Covalent Organic Frameworks as an Intrinsic Proton-Conducting Electrolyte, Rapid Commun. 2021, 43, 2100590.
4. A. Kobayashi*, S. Imada, **Y. Yao**, Y. Nagao, Y. Kubota, M. Yoshida, M. Kato*, Halide Replacement Effect on Proton Conductivity and Vapochromic Luminescence of Pt(II) Complexes, Bull. Chem. Soc. Jpn. 2021, 94, 2466–2473.

Conferences:

1. **Yuze Yao**, Hayato Watanabe, Mitsuo Hara, Shusaku Nagano, Yuki Nagao “Lyotropic liquid crystal property and organized structure in high proton-conductive semi-alicyclic sulfonated polyimide thin films” 68th Symposium on Macromolecules, 2019/9. (Poster Presentation)
2. **Yuze Yao**, Hayato Watanabe, Mitsuo Hara, Shusaku Nagano, Yuki Nagao “· Lyotropic liquid crystal property and organized structure in high proton-conductive semi-alicyclic sulfonated polyimide thin films” Japanese Liquid Crystal Conference 2019, 2019/9. (Poster Presentation)

3. **Yuze Yao**, Hayato Watanabe, Mitsuo Hara, Shusaku Nagano, Yuki Nagao “Lyotropic liquid crystal property and organized structure in high proton-conductive semi-alicyclic sulfonated polyimide thin films” 3rd SYMPOSIUM ON INDUSTRIAL SCIENCE AND TECHNOLOGY, 2021/8. (Oral Presentation)
4. **Yuze Yao,** Miaomiao Liu, Naoki Hida, Mitsuo Hara,Shusaku Nagano, Yuki Nagao “Effect of oligooxyethylene side chains on lyotropic liquid crystallinity and proton conduction of sulfonated polyimide thin films” Japanese Liquid Crystal Conference 2021, 2021/9. (Oral Presentation)

Award:

The Society of Polymer Science, Japan Symposium on Macromolecules Poster Award 2019

Abstract of Minor Research

In this study, sulfonated semi-alicyclic polyimide (BSPA-BOEDA) in the weight ratio of 5% as a binder was investigated for graphite anode in lithium-ion batteries (LIBs). The electrochemical properties of BSPA-BOEDA -based anodic half-cell were investigated. Compared to sodium carboxymethyl cellulose (CMC)-based anodic half-cells, the BSPA-BOEDA -based anodic half-cell exhibited a higher lithium-ion diffusion coefficient of 7.15×10^{-9} cm^2s^{-1} (5.47×10^{-9} cm^2s^{-1} for CMC). According to electrochemical impedance spectroscopy (EIS) results, BSPA-BOEDA -based anodic half-cell had lower interfacial resistance after cyclic voltammetry (CV) than CMC-based anodic half-cell. BSPA-BOEDA -based anodic half-cell showed higher discharge capacity at all current rates than CMC-based anodic half-cell. The highest discharge capacity of BSPA-BOEDA -based anodic half-cell was 161 mAh/g at 1C rate which is 2 times higher than that obtained from CMC-based anodic half-cell (56 mAh/g).

Keywords: water-soluble binder, discharge capacity, capacity retention, interfacial resistance, solid electrolyte interface (SEI)